

The Collision between g-C₃N₄ and QDs in the Fields of Energy and Environment: Synergistic Effects for Efficient Photocatalysis

Yongxi Chen, Min Cheng,* Cui Lai,* Zhen Wei,* Gaoxia Zhang, Ling Li, Chensi Tang, Li Du, Guangfu Wang, and Hongda Liu

Recently, graphitic carbon nitride (g-C₃N₄) has attracted increasing interest due to its visible light absorption, suitable energy band structure, and excellent stability. However, low specific surface area, finite visible light response range (<460 nm), and rapid photogenerated electron–hole (e[−]–h⁺) pairs recombination of the pristine g-C₃N₄ limit its practical applications. The small size of quantum dots (QDs) endows the properties of abundant active sites, wide absorption spectrum, and adjustable bandgap, but inevitable aggregation. Studies have confirmed that the integration of g-C₃N₄ and QDs not only overcomes these limitations of individual component, but also successfully inherits each advantage. Encouraged by these advantages, the synthetic strategies and the fundamental of QDs/g-C₃N₄ composites are briefly elaborated in this review. Particularly, the synergistic effects of QDs/g-C₃N₄ composites are analyzed comprehensively, including the enhancement of the photocatalytic performance and the avoidance of aggregation. Then, the photocatalytic applications of QDs/g-C₃N₄ composites in the fields of environment and energy are described and further combined with DFT calculation to further reveal the reaction mechanisms. Moreover, the stability and reusability of QDs/g-C₃N₄ composites are analyzed. Finally, the future development of these composites and the solution of existing problems are prospected.

Among all possible options, semiconductor photocatalytic technology is considered as an environmentally friendly and ideal strategy among all possible options and has been rapidly developed around the world.^[5–9] Since the first report of artificial photocatalysis in 1972 by Fujishima et al., traditional TiO₂ has been widely used because of its intrinsic photocatalytic performance, low toxicity, and thermodynamic stability.^[10–12] However, TiO₂ can be only photogenerated under ultraviolet light (UV-light), limiting its utilization efficiency of solar energy.^[13,14] Accordingly, researchers are actively searching for photocatalysts with excellent visible light response and satisfactory photocatalytic performance.^[15–17]

Graphitic carbon nitride (g-C₃N₄) is a metal-free nanomaterial composing of C and N with a defect-N bridges of s-triazine or tri-s-triazine (Figure 1A,B).^[19,20] The history of C₃N₄ could be traced back to 1834, but g-C₃N₄ was not formally proposed until 1996 by Teter and Hemley,


probably due to its high stability and mysterious structure.^[21] Subsequently, g-C₃N₄ has emerged as an encouraging candidate for photocatalysts based on its moderate bandgap, suitable energy band structure (Figure 1C), visible light absorption and high stability, as well as been widely concerned by countries all over the world.^[18,22–24] Since the photocatalytic H₂ evolution of g-C₃N₄ was first reported in 2009, the research on improving the photocatalytic performance of g-C₃N₄-based photocatalysts has gradually become a popular research direction (Figure 2).^[18,25,26] Pristine g-C₃N₄ can be prepared by using the heat treatment of some low-cost nitrogen-rich organic precursors, such as urea, melamine, dicyandiamide, and so on.^[27] However, their practical applications have been limited by several shortcomings of pristine g-C₃N₄, including low specific surface area, insufficient utilization of visible light (< 460 nm), and rapid recombination of photogenerated electron–hole (e[−]–h⁺) pairs.^[28,29] For the sake of overcoming these challenges, many methods have been employed to modify g-C₃N₄ to improve the photocatalytic activity, such as element/heteroatomic doping,^[30] structural design,^[31,32] and heterojunction construction.^[33–35] Among the recent progresses of modifying g-C₃N₄, heterojunctions formed

1. Introduction

Population growth and accelerated industrialization have led to a critical energy scarcity and environmental pollution. Therefore, great efforts have been committed to the efficient development of advanced technologies to address these issues.^[1–4]

Y. Chen, M. Cheng, C. Lai, Z. Wei, L. Li, C. Tang, L. Du, G. Wang, H. Liu
College of Environmental Science and Engineering
Key Laboratory of Environmental Biology and Pollution Control
of Ministry of Education
Hunan University
Changsha 410082, China
E-mail: chengmin@hnu.edu.cn; laicui@hnu.edu.cn;
z.wei925@hnu.edu.cn

G. Zhang
Carbon Neutrality Research Institute of Power China Jiangxi Electric
Power Construction Co., Ltd.
Nanchang 330001, China

 The ORCID identification number(s) for the author(s) of this article can be found under <https://doi.org/10.1002/smll.202205902>.

DOI: 10.1002/smll.202205902

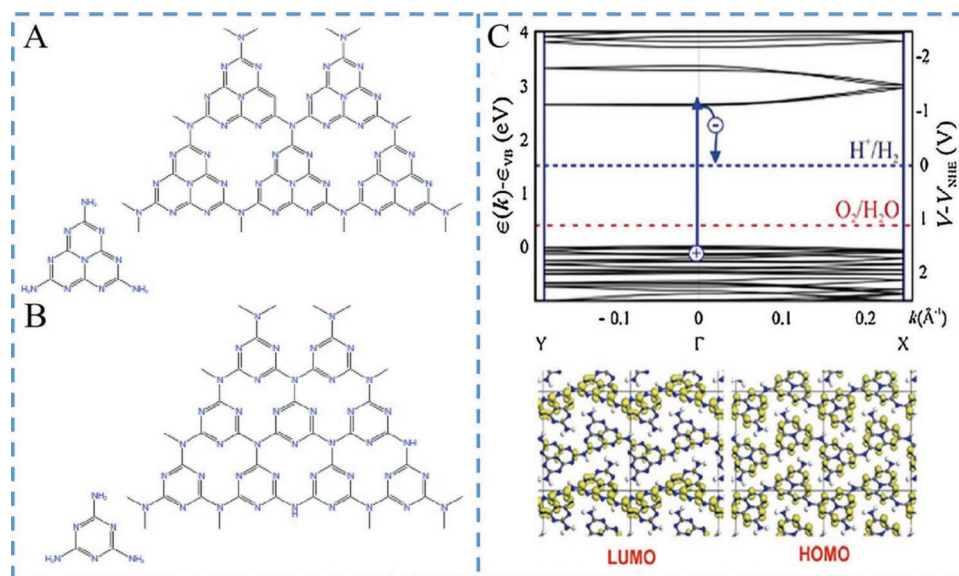


Figure 1. The g-C₃N₄ with a defect-N bridged A) s-triazine or B) tri-s-triazine; C) electron configuration of aggregate melon. Adapted with permission.^[18] Copyright 2008, Nature Publishing Group.

by coupling with other semiconductors are considered as a reliable and effective method. This is because g-C₃N₄-based composites are easier to synthesize, and not only overcome their limitations of individual components, but also successfully inherit their respective advantages.^[36,37]

0D quantum dots (QDs), as semiconductor nanocrystals with dimensions of 1–10 nm, became the culmination of research in 1998 when they were applied in the biological field due to their optical properties.^[38] Subsequently, QDs have stepped into the field of photocatalysis relying on their large surface area, significant quantum effects (high quantum yield), size-tunable spectral properties, and short charge migration distance and exhibit a good effect combining with other photocatalysts.^[39,40] Over other traditional semiconductor materials, using QDs to combine with g-C₃N₄ provides the following advantages over other traditional semiconductor materials: 1) QDs have a larger specific surface area and thus can provide abundant active sites for g-C₃N₄ with higher photocatalytic performance, which can increase material

utilization rate and save cost;^[41–43] 2) QDs can adjust the light response range of g-C₃N₄ due to their size-tunable spectral properties;^[44,45] 3) QDs have a shorter migration distance, which speed up the electron migration rate; and 4) reduction of catalyst nanoparticles of quantum scale (QDs) is a viable way to increase the probability with g-C₃N₄ and make the interface contact tighter, thus accelerating the separation of photogenerated e[−]–h⁺ pairs and effectively inhibiting their recombination.^[42,46] In turn, g-C₃N₄ can be used as a carrier to load QDs uniformly, avoiding the aggregation caused by the high surface energy and abundant surface defects of QDs.^[47,48] Based on these advantages, QDs and g-C₃N₄ are indeed good choices for each other (**Figure 3**). Therefore, QDs/g-C₃N₄ composites were first constructed for photocatalytic H₂ production in 2012.^[49] Later on, the last decade have witnessed rapid progress in QDs/g-C₃N₄ composites for photocatalytic reactions.^[33,50–56]

To date, research in related fields is vigorous and some related reviews cut a figure. Chen and Bai first summarized the

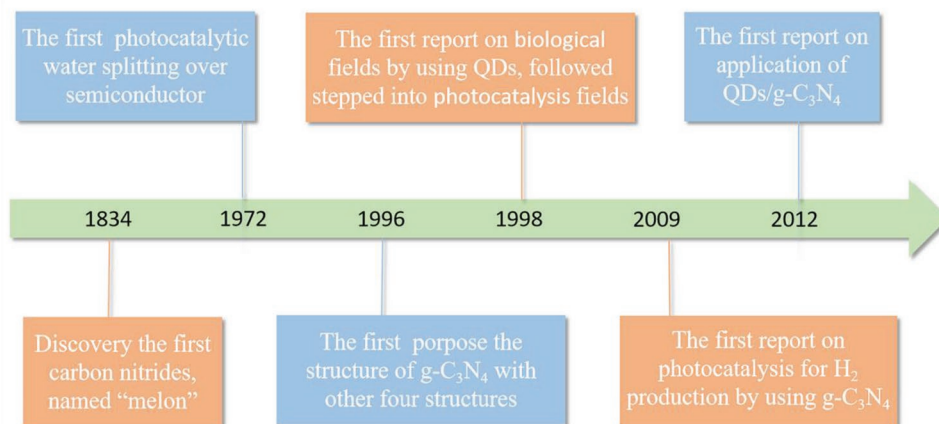


Figure 2. The timeline of important breakthroughs for QDs/g-C₃N₄ composites.

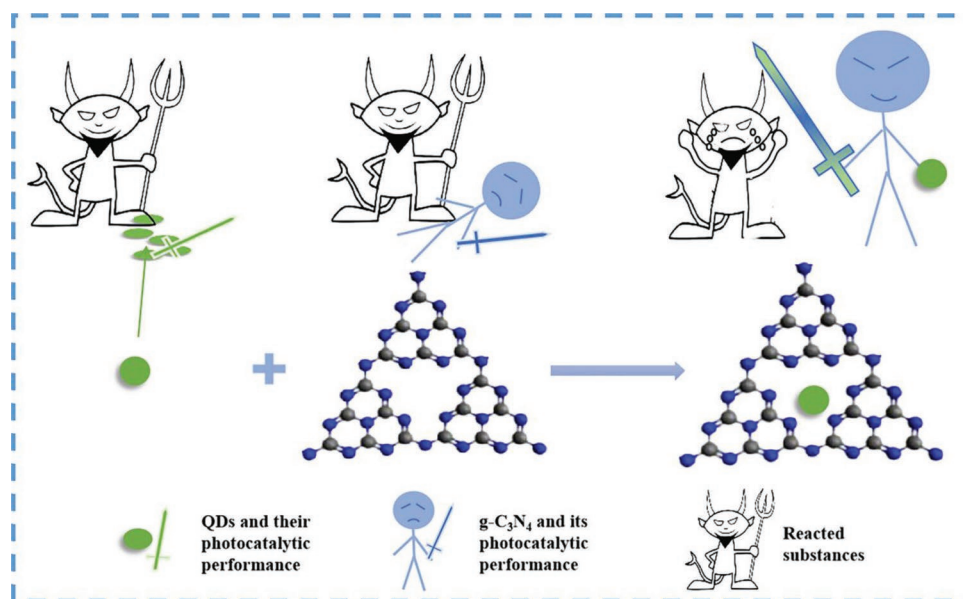


Figure 3. The collision between QDs and g-C₃N₄ for a high photocatalytic performance.

development of metal-free QDs/g-C₃N₄ composites.^[57] Subsequently, Hu et al. introduced the optical properties of QDs/g-C₃N₄ and their applications in H₂ production, CO₂ reduction, and pollutant degradation.^[58] However, as a rapidly changing research field, currently studies of QDs/g-C₃N₄ composites have been extended to apply in other fields such as H₂O₂ generation and NO oxidation. Considering the prospect of QDs/g-C₃N₄, it is indispensable to make a comprehensive summary of those composites in order to further analyze QDs/g-C₃N₄ and apply them to the real application as soon as possible. In this review, the synthesis methods of QDs/g-C₃N₄ composites are summarized as well as their applicability and properties are discussed. Second, the fundamental of QDs/g-C₃N₄ composites is briefly introduced, composing of the basic photocatalytic mechanism, the classification, the synergistic effects and the modification strategies with various charge transfer pathways. Particularly, the synergistic effects of QDs/g-C₃N₄ composites are analyzed comprehensively, including the factors that enhance the photocatalytic performance and the avoidance of QDs aggregation. Thirdly, on the basis of photocatalytic reaction, the photocatalytic applications of QDs/g-C₃N₄ composites in the fields of environment and energy are described, and the mechanisms are further revealed and summarized with the help of DFT calculation. Fourthly, the stability and reusability of QDs/g-C₃N₄ composites are analyzed to provide a direction for their practical application. Finally, the development of these composites and existing problems to be solved are prospected for the large-scale promotion and application of QDs/g-C₃N₄ composites photocatalysts.

2. Synthesis Strategies of QDs/g-C₃N₄ Composites

The microstructure and distribution of loaded QDs in QDs/g-C₃N₄ composites may differ under different synthetic

conditions, resulting in different properties of the composites. In order to optimize the properties of QDs/g-C₃N₄ composites, different synthetic strategies have been explored to prepare them. In this section, hydrothermal/solvent, impregnation, deposition, self-assembly and calcination method are introduced in detail. More importantly, the applicability of different synthetic routes and the properties of these systems are discussed and summarized.

2.1. Hydrothermal/Solvothermal Method

The hydrothermal/solvothermal method means that QDs/g-C₃N₄ composites are generated via heating the reaction system to a critical temperature with an aqueous/organic solution as reaction solvents in a closed reactor. Based on this method, Yao and co-workers prepared 0D/2D composites of g-C₃N₄ loaded with Cd_{0.5}Zn_{0.5}S QDs.^[59] Typically, ultrathin g-C₃N₄ can be attained from urea by pyrolysis and thermal-exfoliating. The raw materials of Cd_{0.5}Zn_{0.5}S QDs and as-prepared g-C₃N₄ were then heated at 180 °C for 24 h to obtain the composites. Cd_{0.5}Zn_{0.5}S QDs with a particle size of approximately 5 nm were uniformly dispersed on the surface of g-C₃N₄ by the image of high-resolution transmission electron microscope (HRTEM) (Figure 4A). More importantly, the pure Cd_{0.5}Zn_{0.5}S sample was gathered into microspheres with the ≈500 nm diameters without g-C₃N₄ under the same hydrothermal conditions (Figure 4B). The authors attributed this uniformly dispersed phenomenon to the rapid heterogeneous nucleation of Cd_{0.5}Zn_{0.5}S QDs by the oxygen-containing defects on the surface of g-C₃N₄, the amino groups that acted as anchor sites and the surface diffusion resistance of g-C₃N₄. Similarly, NiS₂ QDs/g-C₃N₄,^[60] g-C₃N₄/AgVO₃/SnO₂ QDs^[61] were also successfully fabricated by this method.

The hydrothermal method has advantages of convenience and low cost, but there are obvious drawbacks (e.g.,

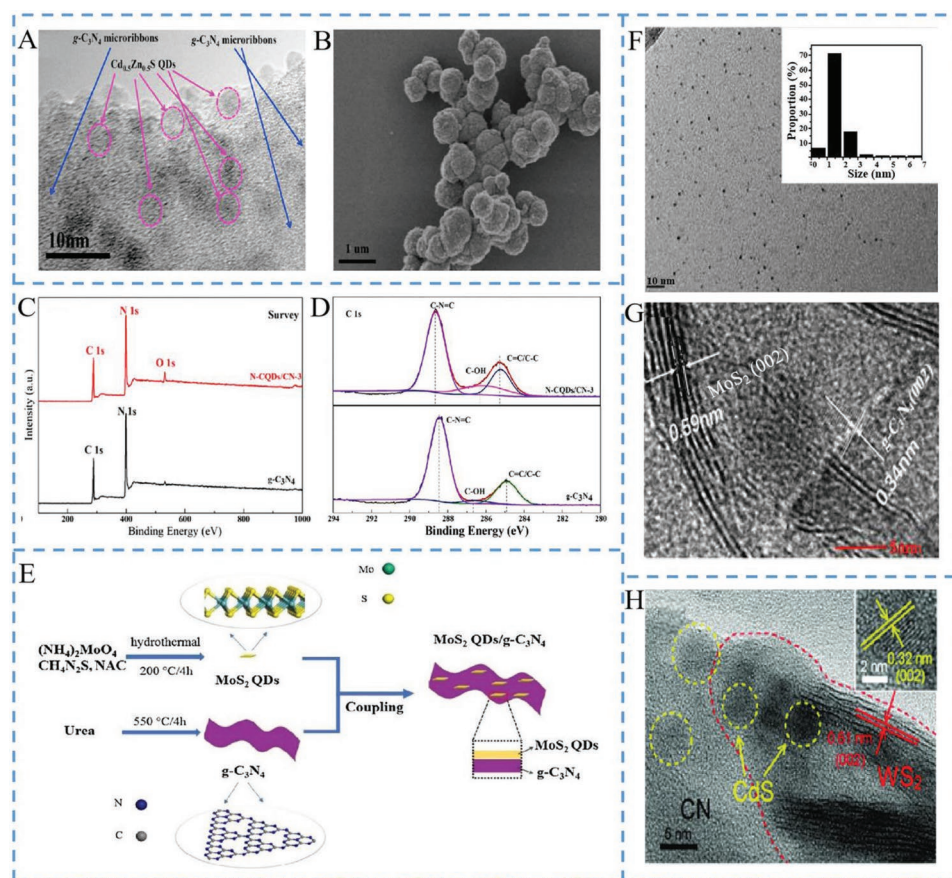


Figure 4. A) The HRTEM image of $\text{Cd}_{0.5}\text{Zn}_{0.5}\text{S}$ QDs/ $\text{g-C}_3\text{N}_4$; B) the SEM image of pure $\text{Cd}_{0.5}\text{Zn}_{0.5}\text{S}$ QDs. Adapted with permission.^[59] Copyright 2016, Elsevier. XPS spectra of N-CQDs/CN-3 and $\text{g-C}_3\text{N}_4$ composites C) survey; D) C 1s. Adapted with permission.^[63] Copyright 2021, Elsevier. E) Schematic illustration of a synthetic route for MSQD-CN; F) the TEM image of MoS_2 QDs; G) the HRTEM image of 5 wt% MSQD-CN. Adapted with permission.^[65] Copyright 2018, Elsevier. H) The TEM image of $\text{CdS}/\text{WS}_2/\text{CN}$. Adapted with permission.^[67] Copyright 2018, Wiley-VCH.

time-consuming) and usually confined to the metal sulfides or metal oxides materials.^[36] To solve the above problems, the solvothermal method uses organic solution as solvent, which greatly improves the dissolution, dispersion and chemical reactivity of reactants, thus accelerating the reaction and even realizing the reaction that cannot be carried out under conventional conditions. For instance, Liu et al. uniformly decorated $\text{g-C}_3\text{N}_4$ nanosheets (UCN) with carbon QDs (CQDs) of 2–5 nm particle size by the solvothermal method.^[62] Different amounts of CQDs suspension were added into 40 mL of ethanol to disperse on UCN. Then, the mixture was maintained in Teflon-lined autoclave at 120 °C for 2 h, and other steps were analogous to hydrothermal methods. Similarly, Chen et al. loaded N-CQDs on the $\text{g-C}_3\text{N}_4$ via C–O–C bonding and the composites maintained the primitive structure of $\text{g-C}_3\text{N}_4$ (Figure 4C,D).^[63]

In conclusion, the hydrothermal/solvothermal method has become an important way to combine QDs with $\text{g-C}_3\text{N}_4$ due to the advantages of simplicity and low cost. Furthermore, the obtained composites are characterized by the characteristic of crystal structure and controllable size.^[64] However, the waste liquid generated from the reaction needs further treatment.

2.2. Impregnation Method

Due to its simplicity, high utilization rate, and low cost, the impregnation method is commonly used to prepare QDs/ $\text{g-C}_3\text{N}_4$ composites. To be specific, the impregnation method mainly involves the immersion of the carrier into a solution containing the active substance, which is subsequently randomly immersed into the cavities or structures of the carrier, and finally, the catalyst is obtained after a post-processing step (e.g., drying). Liu et al. attained MoS_2 QDs and $\text{g-C}_3\text{N}_4$ via hydrothermal method and calcination method, respectively, and then used MoS_2 QDs to decorate $\text{g-C}_3\text{N}_4$ by vigorous stirring for 24 h after adding acetone (Figure 4E).^[65] Transmission electron microscope (TEM) images showed that MoS_2 QDs had the average diameter of 1.7 nm and were closely attached to the $\text{g-C}_3\text{N}_4$ nanostructure via (002) crystal planes (Figure 4F,G).

Fan et al. prepared the composite of CdS QDs/nanoporous $\text{g-C}_3\text{N}_4$ (np $\text{g-C}_3\text{N}_4$) by similar steps.^[66] However, the grain size of CdS QDs (≈ 10 nm) in the 10%-CdS QDs/np $\text{g-C}_3\text{N}_4$ was increased compared to pure CdS QDs (≈ 3 nm), which may be ascribed to the excessive load of CdS QDs under heating conditions and the addition of acetone. Moreover, the Brunauer-Emmett-Teller (BET) surface area of composites decreased with

the increasing of CdS QDs content, revealing that CdS QDs partially blocked the nanopores of $\text{ngp-C}_3\text{N}_4$. For a well-dispersed and a higher load of QDs on $\text{g-C}_3\text{N}_4$, Zou et al. prepared WS_2/CdS QDs/ $\text{g-C}_3\text{N}_4$ composites by a multiple chemical impregnation method.^[67] Specifically, the 2D/2D composites of $\text{WS}_2/\text{g-C}_3\text{N}_4$ were soaked in $\text{Cd}(\text{CH}_3\text{COO})_2$ and Na_2S solutions alternately, followed by soaking, washing, and drying for eight cycles to attain the CdS QDs/ $\text{WS}_2/\text{g-C}_3\text{N}_4$. TEM image displayed that the diameter of CdS QDs in the composites was 4–5 nm, which was close to that of pure CdS QDs (Figure 4H).

The above conclusion proves that the impregnation method is simple and suitable for loading with low QDs content (usually maintaining small sizes of QDs) in QDs/ $\text{g-C}_3\text{N}_4$ composites. However, once the content of QDs increases, the QDs may accumulate and then increase in size. In addition, QDs may be more likely to clog the pore, resulting in reduced specific surface area and active sites, and non-uniform loading, which are worthy of attention.

2.3. Deposition Method

The deposition method is a widely used and effective method to prepare $\text{g-C}_3\text{N}_4$ -based metallic photocatalysts with highly activity

and more uniform distribution due to the N-containing groups in $\text{g-C}_3\text{N}_4$ for binding with metal cation. Basically, composites are obtained by adding loaded material to the carrier suspension and then treating it with certain precipitating agents (e.g., adding ammonia to adjust pH). For example, Lu and co-workers prepared Ni_2P QDs/ $\text{g-C}_3\text{N}_4$ composites via a simple deposition and calcination process.^[42] The as-prepared $\text{g-C}_3\text{N}_4$ was well-dispersed in deionized water, followed by the slow addition of aqueous NaOH (0.15 M) and $\text{Ni}(\text{OAc})_2 \cdot 4\text{H}_2\text{O}$ solution to the above solution in turn. Then the attained greenish yellow precursors were ground with NaH_2PO_2 . At last, the mixture was calcined in a tube furnace under nitrogen (N_2) atmosphere for 4 h. The N 1s binding energy of the tertiary nitrogen groups of Ni_2P QDs/ $\text{g-C}_3\text{N}_4$ was reduced by 0.2 eV, demonstrated that the N–Ni bonds were formed for the tighter contact and better e^- – h^+ transfer capability (Figure 5A). Sreekanth et al. fabricated CeO_2 QDs/ $\text{g-C}_3\text{N}_4$ photocatalyst via a similar method,^[68] which constrained the over-growth and improved the crystallinity of QDs by N-bind and homogeneous reaction of $\text{g-C}_3\text{N}_4$ as well. Furthermore, it has been noted that the deposition method has been applied to combine QDs with 1D $\text{g-C}_3\text{N}_4$,^[69,70] which could impart a larger specific surface area. The fabrication process of CeO_2 QDs/S-doped CN nanotubes (SCN NTs) was described in Figure 5B.^[70] SCN NTs with a uniform fiber-like morphology via

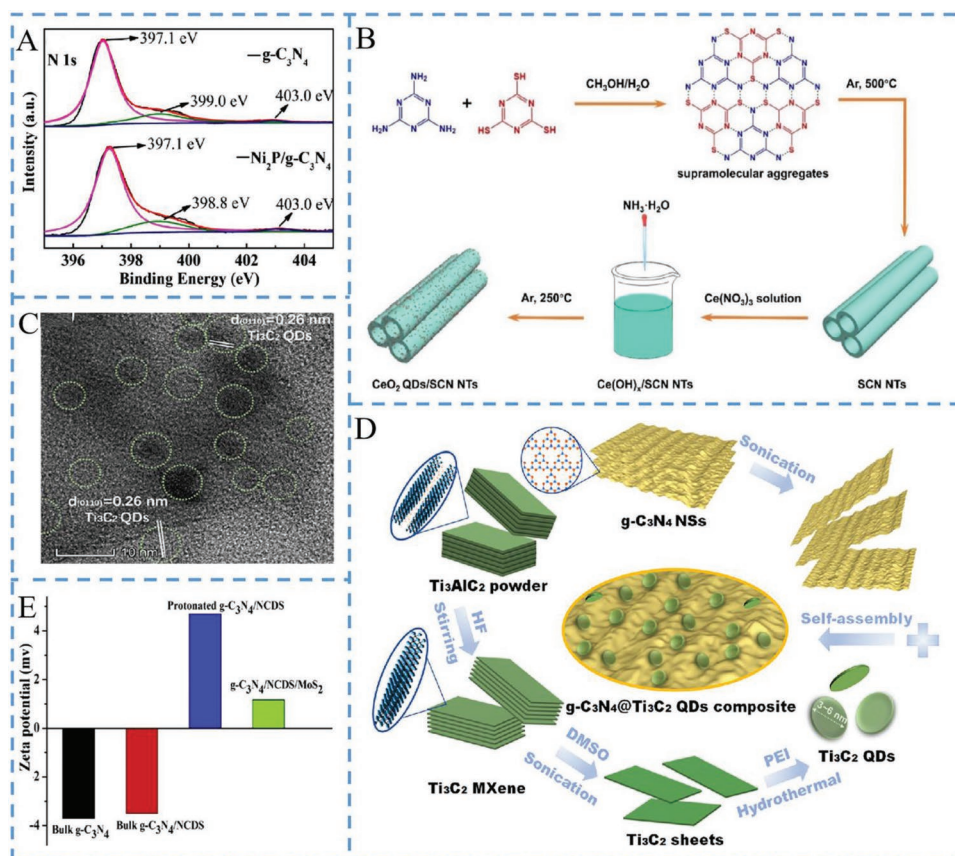


Figure 5. A) XPS spectra of $\text{g-C}_3\text{N}_4$ and $\text{g-C}_3\text{N}_4/\text{Ni}_2\text{P}$: N 1s. Adapted with permission.^[41] Copyright 2018, Elsevier. B) Preparation of CeO_2 QDs/SCN NTs by simple deposition method. Adapted with permission.^[42] Copyright 2020, Elsevier. C) The HRTEM image and D) Schematic Illustration of the preparation of $\text{g-C}_3\text{N}_4@/\text{Ti}_3\text{C}_2$ QD composites. Adapted with permission.^[50] Copyright 2019, American Chemical Society. E) The zeta potentials of bulk $\text{g-C}_3\text{N}_4$, bulk $\text{g-C}_3\text{N}_4/\text{NCDS}$, protonated $\text{g-C}_3\text{N}_4/\text{NCDS}$, and $\text{g-C}_3\text{N}_4/\text{NCDS}/\text{MoS}_2$ photocatalysts. Adapted with permission.^[70] Copyright 2019, Elsevier.

the thermal polymerization were added to $\text{Ce}(\text{NO}_3)_3$ solution, followed by depositing Ce^{3+} with the addition of $\text{NH}_3 \cdot \text{H}_2\text{O}$. Finally, the obtained composites were dried and calcined at 250°C under an Ar gas atmosphere for 4 h. The larger specific surface area of CeO_2/SCN NTs than that of SCN NTs was attributed to the active role of 1D SCN in the higher dispersion of CeO_2 QDs with the smaller particle size.

Obviously, the composites prepared by deposition method are relatively uniform and suitable for metallic substance due to the N-containing groups in $\text{g-C}_3\text{N}_4$ for binding with metal cation. However, the operating conditions (pH regulation) of this method are not easily controlled and time consuming.

2.4. Self-Assembly Method

Self-assembly is an effective method to intermix the components in composites. Considering the amphoteric nature of $\text{g-C}_3\text{N}_4$, its surface charge can be controlled through adjusting the pH of the suspension to combine with charged ions or substances. Thus, Li et al. designed 0D/2D Ti_3C_2 QDs/ $\text{g-C}_3\text{N}_4$ via a self-assembly method for H_2 production (Figure 5D).^[41] Specifically, CON_2H_4 was used as the precursor and sonicated to get uniform monolayers or few layers of $\text{g-C}_3\text{N}_4$. Ti_3C_2 sheets were prepared via selective etching the MAX phase (Ti_3AlC_2) with hydrofluoric (HF) acid, followed by destroyed through dimethyl sulfoxide (DMSO) intercalation and ultrasonic treatment. For purpose of strengthening the interfacial contact, negatively charged $\text{g-C}_3\text{N}_4$ and Ti_3C_2 QDs modified by polyethyleneimine (PEI) were mixed and then freeze-dried for 24 h. The HRTEM analysis demonstrated that the uniformly dispersion and close interaction were established between Ti_3C_2 QDs and $\text{g-C}_3\text{N}_4$ (Figure 5C), which were suitable for photocatalytic reactions. Correspondingly, Jiao et al. formed MoS_2 QDs/ $\text{g-C}_3\text{N}_4$ /NCDS by self-assembly and solvothermal methods.^[50] In this study, the obtained NCDS/ $\text{g-C}_3\text{N}_4$ was protonated and able to combine with negatively charged MoS_4^{2-} ($(\text{NH}_4)_2\text{MoS}_4$) via the electrostatic interaction (Figure 5E). Then, the mixture formed MoS_2 QDs/ $\text{g-C}_3\text{N}_4$ /NCDS by a hydrothermal reaction. Similar synthesis processes are produced in non-metal composites such as graphene quantum dots (GQDs)/ $\text{g-C}_3\text{N}_4$.^[71,72] Apart from electrostatic interaction, π - π stacking and hydrogen bonding between them were pointed out by the authors.

Briefly, the self-assembly method is a common combinatorial strategy to form a whole through mainly electrostatic interactions. The individuals in the composite maintain the ordered structure and morphology, but the stability of the composite nanomaterials may be relatively poor due to electrostatic interactions between each component without more stable covalent bonds.

2.5. Calcination Method

$\text{g-C}_3\text{N}_4$ is usually prepared via the calcination of urea, dicyandiamide or melamine at a certain temperature. Similarly, calcination as a heating method can be used to synthesize the metal,^[73] or metal oxide QDs/ $\text{g-C}_3\text{N}_4$ composites.^[74–76] For example, Ying et al. synthesized CoO QDs/hollow sphere $\text{g-C}_3\text{N}_4$ (SCNO)

through one-step calcination strategy (Figure 6A).^[75] A mixture containing melamine, $\text{Co}(\text{NO}_3)_2 \cdot 6\text{H}_2\text{O}$ and cyanuric acid was stirred to obtain white precipitates after standing and drying. Then, SCNO/CoO was obtained by calcining at 550°C for 4 h in air. During calcination, the growth of CoO QDs was limited by the produced volatile gas (NO_2 , NH_3), keeping their size at 5 nm.

Unlike calcination, the annealing reaction is carried out at a uniform cooling temperature on the basis of calcination.^[77,78] In the fabrication of Co_3O_4 QDs/ $\text{g-C}_3\text{N}_4$, Zhang et al. added Co_3O_4 QDs suspension into ethanol solution dispersing $\text{g-C}_3\text{N}_4$.^[78] Then the mixture was obtained by solvent evaporation with constant stirring at 100°C and annealed at different temperatures (180 , 250 , 300°C) in 2 h. Interestingly, the author pointed that the small pores were produced around Co_3O_4 QDs, which indicated strong interactions between Co_3O_4 QDs and $\text{g-C}_3\text{N}_4$. Furthermore, the pores and the specific surface area of the composites increased with the increasing treatment temperature, but Co_3O_4 QDs kept good crystallinity in all cases.

During heat treatment, the properties and porosity of composites varied under different temperatures, which indicated that the temperature may be one of the main influence factors in the heat treatment synthesis process. In fact, it is well known that reaction parameters such as heating rate and calcination atmosphere have a certain impact on the properties and porosity of QDs/ $\text{g-C}_3\text{N}_4$ composites, but the relevant discussions have not been reflected in the current research papers. All these factors and underlying mechanisms need to be paid more attention.

2.6. Other Synthesis Methods

Along with the above common synthesis methods, there are other methods to obtain the QDs/ $\text{g-C}_3\text{N}_4$ composites. Some studies have found that illumination also affected the composites during the synthesis process. Li et al. obtained NiO QDs- g-CN composites after refluxing the mixture for 3.5 h and irradiating for 4 h and used the same process to prepare NiO QDs@ g-CN without illumination (Figure 6B).^[79] It was worth mentioned that there was no significant difference in morphology, but illumination treatment was the key to form C–O bonds, which could effectively enhance the e^- - h^+ transfer capacity in composites. In addition, ultrasonic processing is also usually used as an auxiliary synthesis in the synthesis process. Wang et al. successfully prepared Bi_3TaO_7 QDs/ $\text{g-C}_3\text{N}_4$ composite under ultrasonic conditions for 6 h.^[80] The ultrasonic treatment accelerated the suspended solid particles and induced the collision between the particles, so that the particles were converted into Bi_3TaO_7 QDs (≈ 4.8 nm) more uniform and dispersive (Figure 6C–E). Specially, Bi_3TaO_7 QDs were adsorbed and coordinated at the N position and formed C=O bonds with $\text{g-C}_3\text{N}_4$ NSs, which indicated the strong bond coupling in this composite.

The synthesis steps, conditions, and states of the composites were described in detail in this section. It could be easily found that the structures and properties of composites (including the size and the distribution of QDs) were controlled under appropriate synthesis methods and conditions, which displayed

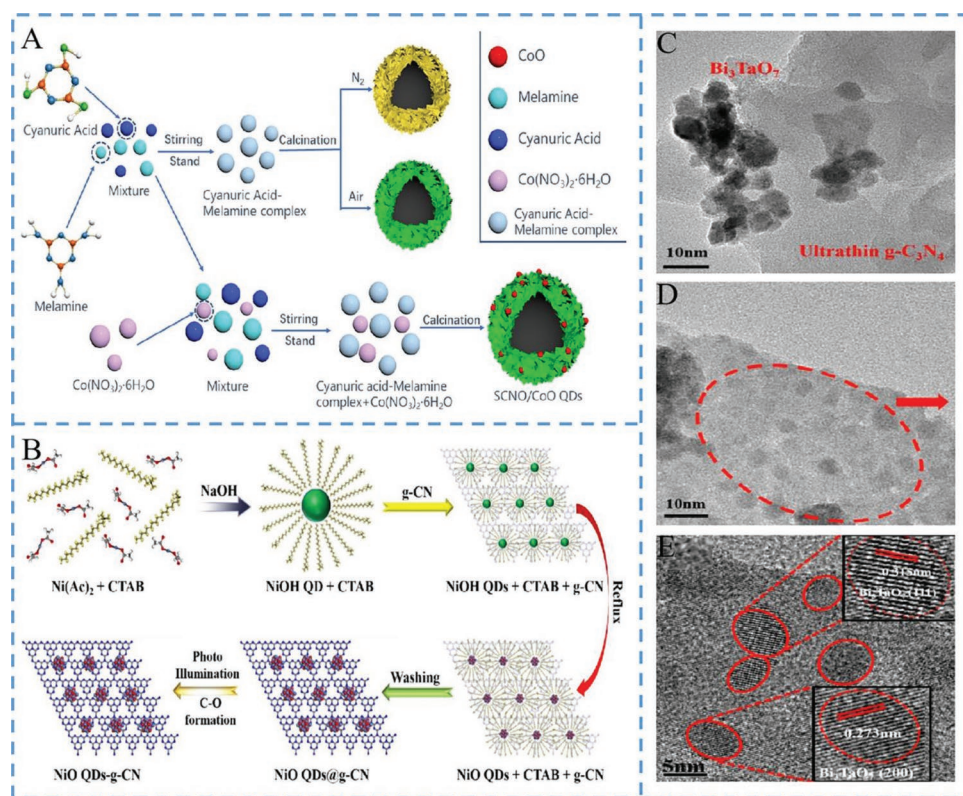


Figure 6. A) The formation process of SCNN, SCNO and SCNO/CoO. Adapted with permission.^[75] Copyright 2021, Elsevier. B) Schematic illustration of a refluxing route for synthesis of NiO QDs@g-CN (without photoillumination) and NiO QDs-g-CN (photoillumination). Adapted with permission.^[79] Copyright 2020, Elsevier. C) The TEM image of 20% of g-C₃N₄/Bi₃TaO₇ QDs before ultrasonic treatment; D) TEM and E) HRTEM images of 20% g-C₃N₄/Bi₃TaO₇ QDs composite. Adapted with permission.^[80] Copyright 2017, American Chemical Society.

through the corresponding characterization techniques.^[41,80] However, the effects of these synthesis conditions on the structure and properties of the composites, which could further affect the photocatalytic performance of QDs/g-C₃N₄ composites, have not been adequately analyzed or investigated.^[66,78] Therefore, clarifying the relationship between the synthesis conditions and the structure as well as the properties of the composites to design efficient photocatalysts is a major challenge in the future.

Furthermore, the advantages, disadvantages, and applicability of above-mentioned five main synthetic methods of QDs/g-C₃N₄ composites are summarized in Table 1. Among

them, hydrothermal/solvothermal, deposition and calcination methods mainly involve the in situ synthesis route. The route focuses on the attachment of precursors or raw materials of QDs to prepare QDs/g-C₃N₄ composites. In this route, the over-growth and aggregation of QDs are effectively restrained by g-C₃N₄, and the composites are linked by more stable covalent bonds. But inevitably the in-situ synthesis is complicated and time-consuming. In contrast, the post-synthesis route is obtained by mixing QDs and g-C₃N₄, which is mainly synthesized through electrostatic interactions by self-assembly method or impregnation method. Compared with the in situ growth route, QDs are formed in a single process that allows

Table 1. Advantages, disadvantages, and applicability of five main synthetic methods of QDs/g-C₃N₄ composites.

Methods	Applicability	Advantages	Disadvantages
a) Hydrothermal/ b) solvothermal method	Applicable to all types of QDs/g-C ₃ N ₄	Convenience, low cost, and controllable size of QDs	(a) Time-consuming and confined to metal oxides/some metal sulfides materials (b) The waste liquid
Impregnation method	Suitable for the with lowly loading QDs	Simplicity, high utilization rate and low cost	The aggregation of QDs with the highly loading QDs, more likely to clog the pores and non-uniform loading
Deposition method	Suitable for metallic composites	Relatively uniform	The no easily controlled operating conditions (pH regulation) and time-consuming
Self-assembly method	Applicable to all types of QDs/g-C ₃ N ₄	Maintaining the ordered structure and morphology of QDs	The relatively poor stability of the composites
Calcination method	Metal/metal oxide composites	The thermal stability	The waste gas

better control of the size and chemical composition.^[81] However, such QDs require the help of ligands (PEI,^[41] thioglycolic acid (TGA),^[51,82] etc.), otherwise they may be unstable during the synthesis process due to QDs aggregation, leading to potential issue such as higher cost.

3. The Fundamental of the Collision between g-C₃N₄ and QDs

3.1. Photocatalytic Mechanisms

The basic principles of photocatalysis have been discussed extensively in previous reports.^[83,84] As shown in **Figure 7**, the photocatalytic reactions of semiconductors consist of the following steps. First, the e^-h^+ pairs can be photogenerated when the semiconductor absorbs energy ($h\nu$) equal or higher than its bandgap. Subsequently, the photogenerated electrons migrate from the valence band (VB) of the semiconductor to the conduction band (CB). When the photogenerated electrons occupy the CB of the semiconductor, the photogenerated holes remain in the VB. Finally, the photogenerated electrons and holes are transferred to the active sites on the semiconductor surface for the reduction and oxidation of various substances, respectively.^[34] Thus, it is obviously that enhancing the optical properties and increasing the specific surface area (active sites) are the effective ways to improve the photocatalytic performance of photocatalysts.^[66,85] Another possible reaction is the recombination of e^-h^+ pairs, which rapidly happens after photoexcitation and release the absorbed energy in the form of light or heat.^[86] It is estimated that up to 90% of photogenerated e^-h^+ pairs recombine rapidly, leading to fewer participating in redox reactions and poor photocatalytic activity.^[87] Accordingly, the recombination of photogenerated e^-h^+ pairs must be prevented to prolonging the lifetime. QDs/g-C₃N₄ composites also follow the above basic photocatalytic processes, but pass through a more complex charge transfer pathway, which is closely related to the properties of materials (energy band, etc.).^[45,51] Detailed synergistic effects on efficient photocatalysis as well as the

charge transfer pathways of QDs/g-C₃N₄ composites are exhibited later (Sections 3.3 and 3.4).

3.2. Classifications of QDs/g-C₃N₄ Composites

In addition to the common advantages of QDs, there are some differences between different types of QDs, making QDs/g-C₃N₄ composites more task-applicable. This section briefly introduced oxide QDs, vanadate QDs, sulfide/phosphide/selenide QDs, carbide QDs and CQDs and GQDs according to the classification of QDs/g-C₃N₄ composites, which would contribute to better understand the differences in terms of synergistic effects, applications and mechanisms.

Oxide QDs generally have a wide bandgap, which may be unable to improve the optical performance of g-C₃N₄.^[88] Correspondingly, oxide QDs with the wide bandgap may have higher oxidation/reduction potential and form multi-types heterostructure with g-C₃N₄, which may bring QDs/g-C₃N₄ composites a stronger redox capacity to attain more active substances. Moreover, oxygen defects may be generated to speed up the separation of photogenerated carriers during the modification of g-C₃N₄ by oxide QDs.^[89–91] Based on these advantages, oxide QDs/g-C₃N₄ composites are more used in environmental fields for the treatment of pollutants. Similarly, vanadate QDs with wide energy bandgaps and likely oxygen vacancies can also form heterojunction with g-C₃N₄, resulting in better photocatalytic performance.^[92–94]

Different from oxide QDs, sulfide/phosphide/selenide QDs have a narrow bandgap, giving a wide range of light response (e.g., CdS QDs) and are therefore also known as photosensitizers.^[49,51] Moreover, most sulfides/phosphates QDs are ideal cocatalysts that accelerate the separation of photogenerated e^-h^+ pairs due to their high conductivity, which is hopeful to substitute Pt-based photocatalysts.^[42,43,95,96] However, sulfide/phosphide/selenide QDs are usually unable to enhance the redox capacity of g-C₃N₄. Thus, such QDs/g-C₃N₄ composites are more used in the field of energy due to their wider range of light response and quicker migration of photogenerated e^-h^+ pairs. Additionally, carbide QDs, such as Ti₃C₂ MXene QDs, can usually be served as cocatalysts because of their high conductivity and relatively stability as well.^[97]

CQDs and GQDs, as two categories of metal-free QDs, can be used as important cocatalysts in the field of photocatalysis due to their good electron storage performance. In addition, CQDs and GQDs possess abundant functional groups and up-conversion properties (displayed in detail later), which bring easier surface functionalization and excellent optical properties.^[98–101] Based on these advantages, CQDs/GQDs modified g-C₃N₄ can accelerate photoelectron transfer and broaden the range of light absorption, which are widely used in various photocatalytic reactions.

3.3. Synergistic Effects of g-C₃N₄ and QDs

As discussed above, both the pristine g-C₃N₄ and QDs have their own disadvantages. For pristine g-C₃N₄, its large-scale applications have considerably limited by the relatively low

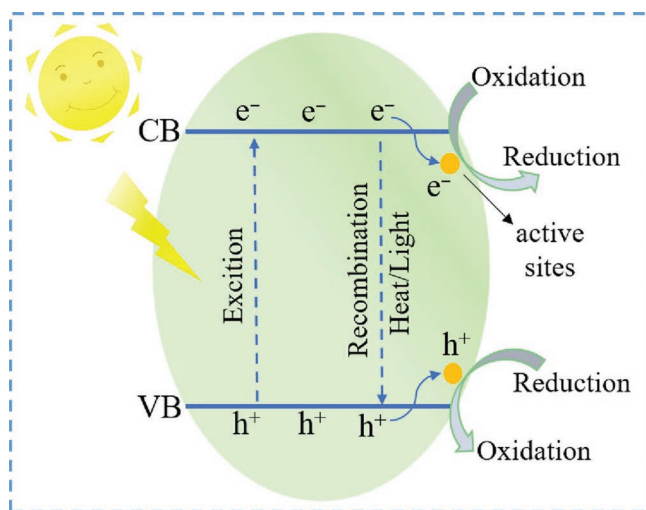


Figure 7. The photocatalytic reactions of semiconductors.

surface area, finite visible light absorption and fast photo-generated e^-h^+ pairs recombination.^[28,29] On the other hand, although QDs with small particle size bring abundant surface defects and high surface energy, they are prone to aggregate, leading to a reduced photocatalytic activity. However, the combinations of QDs and $g-C_3N_4$ successfully overcome each shortcoming and surprisingly produce enhanced properties. Few previous studies have specifically mentioned the synergistic effects of QDs/ $g-C_3N_4$, so this section summarizes the functions generated by synergistic effects.

3.3.1. Variations of Specific Surface Area and Active Sites

It is well known that the larger its surface area has, the more active sites a photocatalysts are, which are beneficial for photocatalytic performance.^[41,78] The high specific surface area due to the small size of QDs provides abundant active sites for QDs/ $g-C_3N_4$ composites, which can increase the reaction sites as well as the absorption sites.^[50,65,95,97,102,103] However, studies have found that most of QDs/ $g-C_3N_4$ composites remained constant or even actually decreased specific surface area than that of $g-C_3N_4$.^[95,104,105] For instance, Qin et al. prepared NiS_2 QDs/ $g-C_3N_4$ by hydrothermal method and the specific surface area of composites was reduced to $62.01\text{ m}^2\text{ g}^{-1}$, less than half of that of $g-C_3N_4$.^[104] Similarly, changes in specific surface area were presented in those composites, such as $1T-MoS_2$ QDs/ $g-C_3N_4$.^[95] S QDs/ $g-C_3N_4$,^[105] judging that QDs might block the mesoporous of $g-C_3N_4$ with a negative influence to photocatalytic reactions.

Interestingly, the opposite conclusion existed for a portion of QDs/ $g-C_3N_4$. Zhao and co-workers prepared $CsPbBr_3$ QDs with a particle size of 5–10 nm and uniformly loaded bulk $g-C_3N_4$ (CN) to form a ternary $Ag-CsPbBr_3$ QDs/CN composites.^[56] The largest specific surface area of $CsPbBr_3$ QDs/CN ($156.73\text{ m}^2\text{ g}^{-1}$) was 7.78 times than that of CN, providing more active sites for photocatalysts. Furthermore, the similar conclusion was reached in the CeO_2 / $g-C_3N_4$.^[91] Part of QDs have positive effects on specific surface area by the formation of new pores, which may be attributed to the suitably increasing of QDs and the tight interface contact.^[78] Moreover, the stripped 2D $g-C_3N_4$ ultrathin nanosheet or construct 1D/3D $g-C_3N_4$ structures could provide more contact area for QDs and thus more QDs could be loaded.^[53,70,75,106] Ultimately, it not only effectively prevented QDs from aggregation or blockage, but also increased the surface area of the composite material. Li et al. designed CeO_2 QDs/SCN via the thermos-condensation coupled in situ deposition method.^[70] The specific surface area of composite was larger ($59.1\text{ m}^2\text{ g}^{-1}$) than pristine SCN because CeO_2 QDs were evenly dispersed inside/outside of SCN. Liu et al. found that $CuFeO$ QDs were embedded into CNN film layers, leading to different degrees of tearing between CNN film layers, which sufficiently exposed more adsorption sites and the area of the composites increased from 69.0 to $150\text{ m}^2\text{ g}^{-1}$.^[107]

At present, the actual role of specific surface area in photocatalytic performance of QDs/ $g-C_3N_4$ is unclear enough. One reason is that the related studies are insufficient, and the other is that their catalytic reactions are controlled by various factors. Nevertheless, there is no doubt that the larger specific surface area endows composites with more active sites, which plays a

positive role in photocatalytic performances and deserves continuous attention.

3.3.2. Transmission of Optical Properties

Solar radiation is mainly concentrated in the visible region (50%), partially in the infrared region (43%), and very little in the ultraviolet region (7%). Thus, it is expected to explore the power of visible and even infrared light to use solar energy more efficiently.^[44,108] Previous reports have shown that the pristine $g-C_3N_4$ possesses a relatively wide bandgap ($\approx 2.73\text{ eV}$) and an absorption edge of $\approx 450\text{ nm}$, which limits its light absorption capacity in a longer wavelength range.^[44] The small size of QDs endows its quantum confinement, which means that the bandgap of may be wider than that of bulk phase semiconductor when the material is reduced to the quantum level.^[40,44,51,109,110] Additionally, the different bandgaps have selective absorption of photons with different abilities, endowing the composites with adjustable light absorption properties.

Due to some materials with narrow bandgaps, the combination of those quantum size materials and $g-C_3N_4$ can make the composites process a wider range of light absorption and stronger light absorption capacity. For example, CdS QDs/ $g-C_3N_4$ was prepared by Ge and co-workers through an impregnation method.^[49] The composite showed enhanced light absorption with an extended range ($\approx 700\text{ nm}$) compared with pure $g-C_3N_4$. Also, the light absorption capacity was further boosted with the increase of QDs, then improving the photocatalytic performance to a great extent.^[50,53,111] More importantly, it was necessary to avoid the aggregation by an appropriate load of QDs. There are many materials having been reported to enhance the light range and light absorption capacity, including some metallic sulfide,^[59,60,112] metallic selenide,^[113,114] and perovskite.^[56,115]

Studies have found that controlling the morphology of $g-C_3N_4$ to construct composites is also acted as an effective method to enhance the light absorption performance.^[53,85] Liang et al. further reported CdS QDs/P-doping carbon nitride hollow tube (P-CNT) composite via an in-situ oil bath method.^[85] The multiple reflections of hexagonal tubes successfully broadened the light absorption capacity for the heightened photocatalytic performance and even the possibility of practical applications. Multiple reflections of light would also be discovered in Ti^{3+} - TiO_2 / $g-C_3N_4$ / MoS_2 QDs and others.^[103,106,116] In general, metal oxides have wider bandgaps (e.g., SnO_2 , TiO_2 , CeO_2). The combination of SnO_2 QDs or TiO_2 QDs with $g-C_3N_4$ showed almost unchanged in light absorption performance compared with pure $g-C_3N_4$.^[88,89,117,118] even causing the blue shift of UV-vis diffuse reflectance spectra.

The up-conversion process mentioned in a recent correlation review is an anti-Stokes emission process in which low-energy photons are absorbed sequentially and shorter photons are emitted.^[58] Its essence is the conversion of low-energy photons into high energy photons. In simple terms, up-conversion materials can obtain long waves (near infrared light) and produce short waves (UV or visible light). A large number of studies have shown that nonmetallic CQDs and GQDs have up-conversion photoluminescence properties.^[100,119,120] As an example, Zhang et al. designed the $FeOOH$ QDs/CQDs/ $g-C_3N_4$

composites (FCCN) by modifying $g\text{-C}_3\text{N}_4$ with double QDs.^[121] When CQDs were injected into the original UCN, the optical response range was significantly widened. However, the amorphous FeOOH QDs were just attached to the surface of the UCN nanosheet without affecting the light absorption performance. This confirmed that the CQDs underwent a two-photon or multi-photon reaction that allowed reactants to absorb near-infrared light and motivate the short wave to $g\text{-C}_3\text{N}_4$, thereby improving the efficiency of sunlight utilization.

In conclusion, QDs share their adjustable light absorption performance with $g\text{-C}_3\text{N}_4$ and have a quite positive effect on capturing near-infrared photons. In addition, strategies such as changing the morphology of composites can further enhance the light absorption ability. Most of QDs containing metal mentioned have good photosensitivity, but it is inevitable to consider the secondary pollution caused by metal leaching. Fortunately, the up-conversion materials can overcome the disadvantage while bringing good light absorption performances with excitingly practical application prospects.^[100,119–121] Recently, studies have proved that shell QDs/ $g\text{-C}_3\text{N}_4$ photocatalysts can be made, which not only possess high photocatalytic activity, but also avoid the leaching of heavy metal ions.^[44]

3.3.3. Tighter Interface Contact

As everyone knows, $g\text{-C}_3\text{N}_4$ has a wide bandgap (≈ 2.73 eV), which is limited its photocatalytic performance because of the incomplete charge separation and rapid recombination of e^-h^+ pairs.^[14,30,36] An interesting phenomenon is that the specific surface area of QDs increases with decreasing particle sizes. On the one hand, the number of surface phase atoms of QDs increases with the decreased sizes of QDs, resulting in insufficient surface atomic coordination and the increase of unsaturated bonds and suspended bonds.^[103,105] In other words, the surface atoms of QDs are more active and likely to bond with $g\text{-C}_3\text{N}_4$, which bring about the tighter interface contact to overcome above challenges.^[65] On the other hand, both the small size of QDs and stripping the bulk $g\text{-C}_3\text{N}_4$ to form 2D film or construct 1D, 3D or even 0D $g\text{-C}_3\text{N}_4$ can reduce photocarriers migration distance. Therefore, under visible light, tighter interface contact and shorter photocarriers migration distance between QDs and $g\text{-C}_3\text{N}_4$ can effectively promote faster e^-h^+ pairs migration and inhibit the recombination of e^-h^+ pairs for a high photocatalytic performance.^[122]

In the report by Lu et al.,^[42] they synthesized Ni_2P QDs/ $g\text{-C}_3\text{N}_4$ composites, which successfully constructed the charge transfer path by the Ni–N bond on the surface. The electron migration resistance was decreased, which facilitated the separation of photocarriers and generated photocurrent 11-fold stronger than pure $g\text{-C}_3\text{N}_4$. Recently, Wang et al. reported that 0D/2D S-QDs/ $g\text{-C}_3\text{N}_4$ composites provided an effective channel for charge transfer and induced effective charge separation through N–S bond coupling.^[105] No significant coupling effect was found in the composite system of large CN and S particles,^[123,124] which effectively proved that reducing the size of S particles and constructing CN with porous structure and reduced thickness were essential to couple composites. It was

worth mentioning that the separation of photogenerated e^-h^+ pairs would take two forms in the QDs/ $g\text{-C}_3\text{N}_4$ composites. In the former, QDs were regarded as cocatalysts (electron acceptors) that captured electrons generated by photogenerated $g\text{-C}_3\text{N}_4$ to improve the separation efficiency.^[43,95–97,125] In the latter, QDs were combined with $g\text{-C}_3\text{N}_4$ to form heterostructures with the matching band and mainly classified to two types of heterojunctions (type-II, and Z-scheme). Both forms were efficiently separated and restrained the recombination of photogenerated e^-h^+ pairs.^[56,90,93,117]

3.3.4. Maintained Morphologies of QDs and $g\text{-C}_3\text{N}_4$

Many literatures have reported that QDs with small sizes tend to aggregate due to their abundant surface defects and high surface energy, resulting in the reduced photocatalytic performance.^[126] Fortunately, $g\text{-C}_3\text{N}_4$ as a stable carrier can be used to uniformly loading QDs by covalent bonds or electrostatic interactions, which efficiently avoids the aggregation phenomenon of QDs, as reported in the section of “2. Synthesis strategies of QDs/ $g\text{-C}_3\text{N}_4$ composites.”^[47,48] Of course, there is a special case that when there are excess QDs, the aggregation can still occur and even shield the active sites of $g\text{-C}_3\text{N}_4$, affecting the light absorption performance of $g\text{-C}_3\text{N}_4$.^[50,59,85] Therefore, it is essential to control the appropriate QDs load on $g\text{-C}_3\text{N}_4$ for subsequent applications.

On the other hand, $g\text{-C}_3\text{N}_4$ possesses high mechanical and chemical stability. Considering the small size of QDs, the morphology of $g\text{-C}_3\text{N}_4$ can be not broken with the introduction of QDs in QDs/ $g\text{-C}_3\text{N}_4$ composites, which is also reflected in many studies.^[92,106,127] For example, Wang et al. prepared composites by interspersing vanadate (AgVO_3 , BiVO_4) QDs on $g\text{-C}_3\text{N}_4$.^[92] The AgVO_3 QDs/ $g\text{-C}_3\text{N}_4$ and BiVO_4 QDs/ $g\text{-C}_3\text{N}_4$ composites remained the sheet morphology of $g\text{-C}_3\text{N}_4$. The quantum size of materials determines its high utilization rate and relatively low content in QDs/ $g\text{-C}_3\text{N}_4$ composites compared with other $g\text{-C}_3\text{N}_4$ based materials, so that the structure of $g\text{-C}_3\text{N}_4$ is basically unaffected by the addition of QDs.^[44] Therefore, QDs can not only be uniformly loaded on $g\text{-C}_3\text{N}_4$, but also maintain the morphology and structure of $g\text{-C}_3\text{N}_4$, which is conducive to the stability of $g\text{-C}_3\text{N}_4$ inherited by the composites and enhance the possibility of practical application.

3.4. Different Modification Strategies with Various Charge Transfer Pathways

This section briefly introduces QDs as an electron carrier for a cocatalyst and as a semiconductor to form heterostructures to combine with $g\text{-C}_3\text{N}_4$, which is beneficial for understanding the mechanism of photocatalysis.

3.4.1. As Cocatalyst

Owing to the high conductivity and photoelectric properties, some QDs are considered as cocatalysts when combined with $g\text{-C}_3\text{N}_4$. Such QDs mainly include some phosphide/sulfide/carbide QDs (1T-MoS_2 QDs,^[43,95,96] Ni_2P QDs,^[42] Ti_3C_2 QDs,^[97]

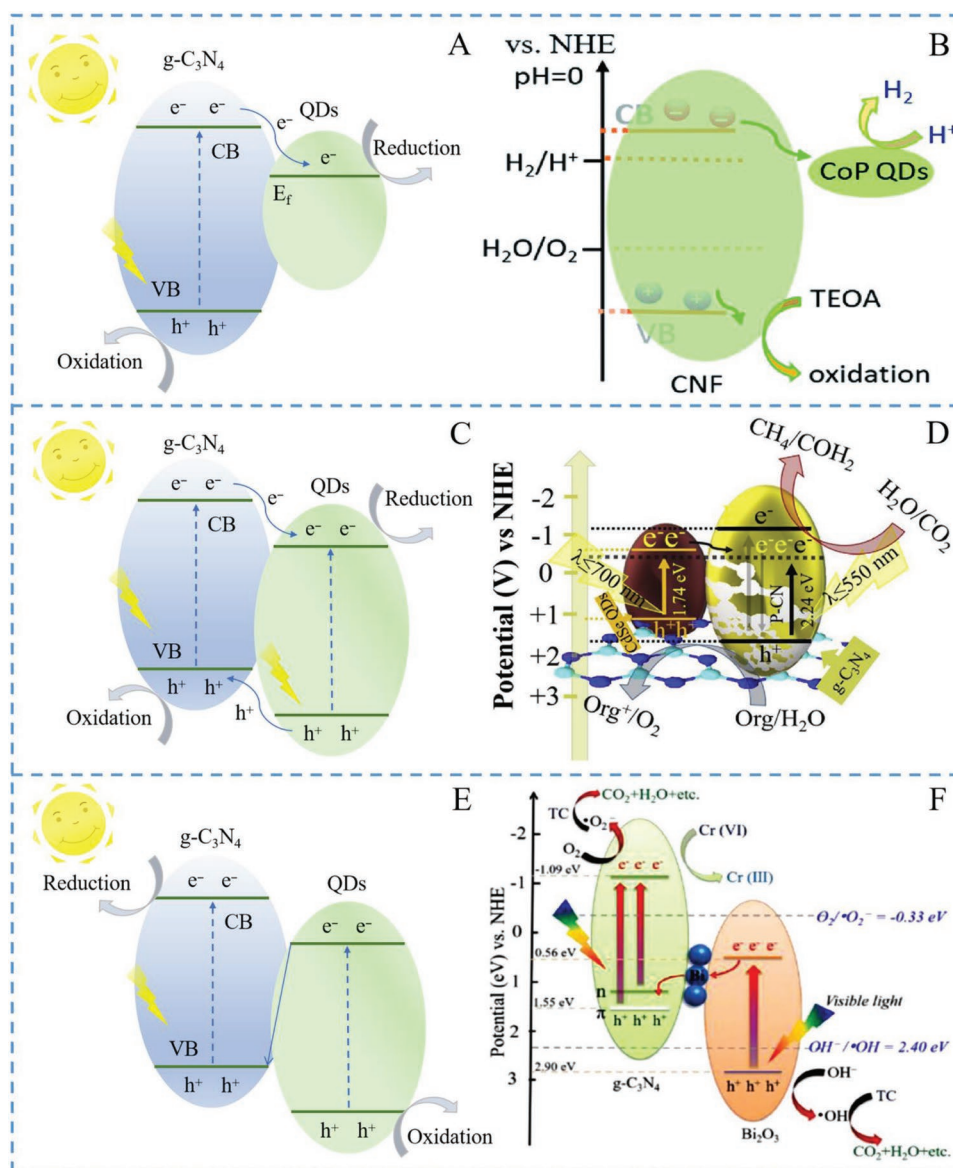


Figure 8. A) The charge transfer path of QDs acting as the cocatalysts in QDs/g-C₃N₄ composites; B) photocatalytic hydrogen generation mechanism on CoP/CNF under visible light. Adapted with permission.^[69] Copyright 2019, Royal Society of Chemistry. C) The charge transfer path of type-II heterojunction QDs/g-C₃N₄ photocatalysts; D) schematics for charge separation and transfer mechanism for redox reactions of CdSe/P-CN. Adapted with permission.^[45] Copyright 2020, Elsevier. E) The charge transfer path of Z-scheme heterojunction QDs/g-C₃N₄ photocatalysts; F) the possible charge separation of Bi₂O₃ QDs/g-C₃N₄ (ii) photocatalyst under visible-light irradiation. Adapted with permission.^[46] Copyright 2021, Elsevier.

etc.) and non-metallic QDs (CQDs,^[101,128–130] GQDs,^[125] etc.). Specifically, cocatalysts can be acted as electron carriers to accept electrons from photogenerated g-C₃N₄ to their Fermi level, which inhibit the recombination of e⁻-h⁺ pairs, and then provide abundant active sites to react with absorbed substance (Figure 8A).^[25,131,132] Excitingly, some studies have shown that these QDs/g-C₃N₄ might be a promising alternative to noble metal and avoid high cost.^[42,69,97] For instance, Zeng et al. adopted a facile strategy to synthesize CoP QDs/ultrafine g-C₃N₄ fiber (CoP QDs/CNF) photocatalysts.^[69] In the aforementioned composites, CoP QDs were uniformly dispersed on the surface of CNF without aggregation, and there was a close interface between them. Meanwhile, electrons from photogenerated CNF

could be injected into CoP QDs, which could greatly restrain the recombination of e⁻-h⁺ pairs and lengthen the lives of electrons. Subsequently, the H⁺ absorbed by CNF was successfully reduced by photogenerated electrons for H₂ on the surface of CoP QDs (Figure 8B). Ultimately, CoP QDs/CNF enhanced photocatalytic activity of H₂ production (2.42 mmol h⁻¹), which was over 207.1 and 32 times that of CNF and Pt/CNF, respectively.

3.4.2. As Semiconductors to form Heterojunction

In general, a heterojunction is defined as an interface region formed by the compounding of two semiconductors with

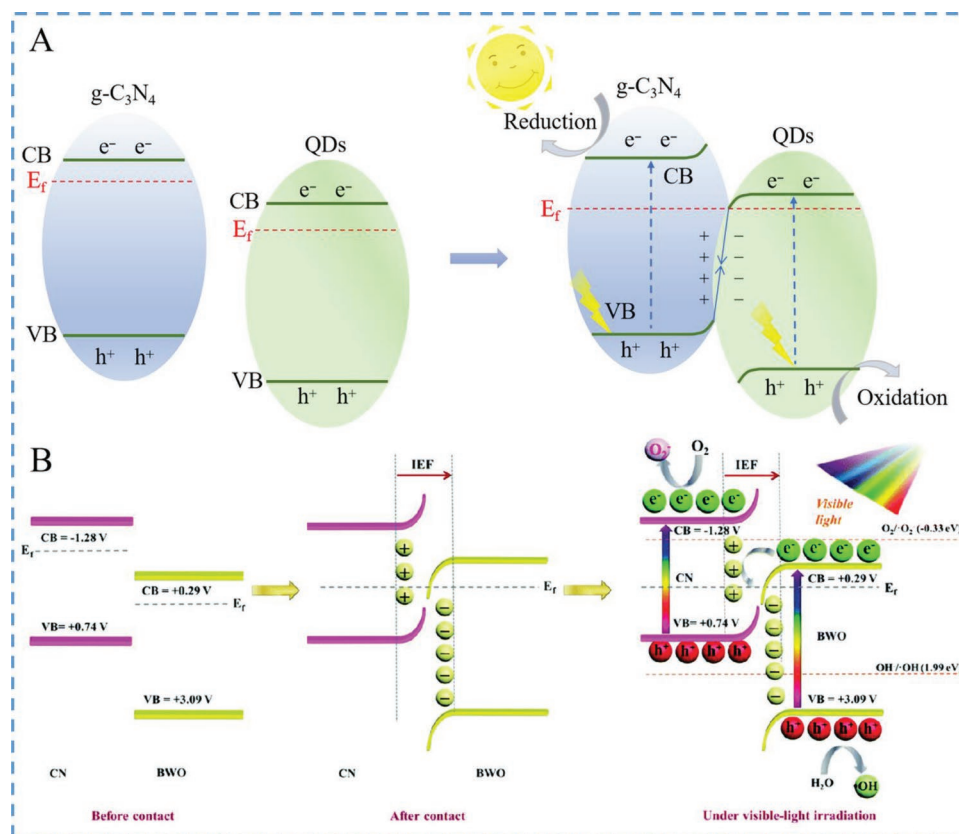


Figure 9. A) The charge transfer path of S-scheme heterojunction QDs/g-C₃N₄ photocatalysts before and after contact; B) S-scheme charge transfer for the photocatalytic elimination of TC and Cr⁶⁺ over CN/BWO. Adapted with permission.^[140] Copyright 2022, Partner Organisations.

inequitable energy band structure, which may result in aligning energy band.^[9,86] Both g-C₃N₄ and some QDs can be excited to produce e⁻-h⁺ pairs under visible light, followed by the separation and transfer of electrons and holes.^[70,88,133] According to the studies of modifying g-C₃N₄ with QDs, various heterojunctions have been shown (Figures 8 and 9).

For type-II heterojunction photocatalysts, the CB and the VB levels of one semiconductor are higher than the corresponding levels of the other semiconductor (Figure 8C).^[34] Therefore, the charge transfer of type-II heterojunction photocatalysts relies on a suitable energy band structure of components, which can make electrons and holes in a spatial separation.^[134] In recent years, g-C₃N₄ has been combined with various QDs semiconductors to jointly construct type-II heterojunction photocatalysts. For example, Fazal et al. constructed CdSe QDs/P doping CN photocatalysts for H₂ generation, CO₂ reduction and 2,4-dichlorophenol degradation (2,4-DCP).^[45] The doping P substituted for carbon in g-C₃N₄, which produced the lower conduction band minimum (CBM) of CN than that of the CBM for CdSe QDs to form type-II heterojunctions (Figure 8D). The well-matched energy band structure made the photogenerated electrons of CN transferring to CdSe QDs as well as the photogenerated holes from CdSe QDs to CN for the reduction/oxidation of H₂O, CO₂ and 2,4-DCP. Overall, the optimized nanocomposites offered the high photocatalytic activity of overall water splitting (H₂: 113 and O₂: 55.5 μmol h⁻¹ g⁻¹), conversion efficiency of CH₄ (47 μmol h⁻¹ g⁻¹), and 2,4-DCP degradation

(78%). Similar high photocatalytic performances were also demonstrated in type-II heterojunction photocatalysts such as oxide QDs/g-C₃N₄,^[89–91] and vanadate QDs/g-C₃N₄.^[92–94,133]

The above contents effectively prove the advantages of type-II heterojunction photocatalysts, but there are still some problems restricting its practical application. For example, the redox reactions of type-II heterojunction photocatalysts usually occur at lower potentials, resulting in the inhibition of redox capacity. Furthermore, electrostatic repulsion is not conducive to the migration of electrons on the CB and the holes on the VB of two semiconductors.^[9,34,135] Therefore, the development of more effective heterojunctions is the most urgent matter. It is a challenge to construct QDs/g-C₃N₄ photocatalysts, which can achieve efficient separation of photogenerated e⁻-h⁺ pairs and maintain the high redox abilities.

Until 1979, Bard et al. first developed the Z-scheme charge transfer mechanism to address these challenges and it was also helpful to construct Z-scheme heterojunction QDs/g-C₃N₄ photocatalysts (Figure 8E).^[136] From past research, the Z-scheme systems can be divided into three categories: traditional Z-scheme (only react in water without physical contact), all-solid-state Z-scheme (via the interface contact and a conductor as a bridge), direct Z-scheme (like all-solid-state Z-scheme without a bridge). Moreover, studies found that Z-scheme heterojunctions were prone to form when g-C₃N₄ meet the materials with high VB potential.^[46,80,93,101,110] Thus, Liang et al. grafted Bi₂O₃ QDs on g-C₃N₄ with the help of EDTA via a facile

two-step method for the high photocatalytic activity to degrade tetracycline (TC) and reduce Cr^{6+} , respectively.^[46] Under visible light, Z-scheme photocatalysts caused the photogenerated electrons to flow from the CB of Bi_2O_3 QDs to the VB of $\text{g-C}_3\text{N}_4$, thus retaining electrons in the CB of $\text{g-C}_3\text{N}_4$ (-1.09 eV) and holes in the VB of Bi_2O_3 QDs (+2.90 eV) (Figure 8F). The generated $\cdot\text{O}_2^-$, $\cdot\text{OH}$, and h^+ would react with TC as well as the photo-generated electrons directly reduced Cr^{6+} . Additionally, this system possessed the reduced Bi^0 as a bridge between Bi_2O_3 QDs and $\text{g-C}_3\text{N}_4$ to accelerate the interfacial transfer of carriers, which could be proved by the higher photocurrent density.

Although Z-scheme heterojunctions show great advantages, the idea of traditional Z-scheme and all-solid-state Z-scheme heterojunctions may be too ideal.^[137] On the one hand, the photogenerated electrons and holes with higher potential are more likely to be annihilated due to the larger redox potential difference, resulting in the electrons and holes to stay at CB and VB with lower redox potential. On the other hand, the Schottky barriers formed at the interface between the conductor and a semiconductor may prevent the continuous electron transfer after equalizing their Fermi levels. Ultimately, in this case, the mentioned heterojunctions may fail to achieve maximized oxidation and reduction capacities. Considering their problems, direct Z-scheme heterojunctions formed from traditional Z-scheme and all-solid-state Z-scheme heterojunctions are susceptible to be misunderstood.

Under this background, Yu and co-workers proposed a step-scheme (S-scheme) heterojunction consisting of two N-type semiconductor photocatalysts (oxidation photocatalysts (OP) and reduction photocatalysts (RP)).^[90,138,139] When OP (with relatively lower VB positions) meet PR (with relatively higher CB positions), an internal electric field (IEF) is created. Then, the photogenerated electrons pass through the interface from RP to OP until the achievement of the same Fermi level (E_f) at the interface, resulting in an upward and downward bending in the band edges of RP and OP. Finally, the relatively useless electron and holes are recombined at the interface; while the photogenerated electrons and holes with strong reduction and oxidation capacity are reserved on the CB of RP and the VB of OP as well as produce reduction reductions and oxidation reactions (Figure 9A).^[94,137] Recently, Li et al. synthesized a high N ratio graphite carbon nitride (C_3N_5)/ Bi_2WO_6 composites by an in-situ route.^[140] The IEF, band bending and Coulombic attraction between C_3N_5 and Bi_2WO_6 were created with the formation of S-scheme (Figure 9B). The powerful electrons (in the CB of C_3N_5) and holes (in the VB of Bi_2WO_6) were maintained to produce much active species ($\cdot\text{O}_2^-$, $\cdot\text{OH}$) with high redox capacity for TC degradation and Cr^{6+} reduction. Ultimately, various QDs/ $\text{g-C}_3\text{N}_4$ composites have been used in the fields of energy and environment by these charge transfer pathways, bringing the considerable photocatalytic performances.^[90,94]

4. Applications of QDs/ $\text{g-C}_3\text{N}_4$ Composites in Energy Fields

The global energy crisis is caused by over-reliance and over-use of fossil fuel during last few decades. Therefore, it is imperative to develop green energy resources (H_2 , H_2O_2) as a long-term

fuel. Furthermore, this problem can be also solved by reducing CO_2 to the transitional fuel. As a combination of two novel materials, QDs/ $\text{g-C}_3\text{N}_4$ composites can be widely applied in energy fields, which introduces in this section.

4.1. H_2 Production

H_2 is considered as an ideal substitute to fossil resources due to its high specific enthalpy and environmentally friendly combustion products.^[134,141,142] Meanwhile, photocatalysis technology has emerged for its advantages of clean green and efficiency in H_2 production since the first photocatalysis water splitting experiment reported by Fujishima and co-workers.^[10] Compared with other photocatalysts, $\text{g-C}_3\text{N}_4$ has a moderate and matched energy band structure, which was successfully applied to produce H_2 under visible light.^[18,143] Recently, the integration composites of QDs with $\text{g-C}_3\text{N}_4$ has shown remarkable photocatalytic water splitting ability, and the latest research progress is summarized in Table 2.

In 2012, Ge et al. synthesized CdS QDs/ $\text{g-C}_3\text{N}_4$ photocatalysts with excellent light absorption performance for H_2 production by chemical impregnation method.^[49] To further release H_2 , it is necessary to introduce additional cocatalyst to reduce the excessive overpotential during the H_2 production process.^[49,56,65,70] The author used Pt as a cocatalyst to load on the composite by stirring and irradiation. Under visible light, the photogenerated electrons transferred from the CB of $\text{g-C}_3\text{N}_4$ to the CB of CdS QDs, and accumulated on Pt, and then participated in H_2 production (Figure 10A). Based on the synergistic effects of Pt, CdS QDs and $\text{g-C}_3\text{N}_4$, the composites showed high photocatalytic activity. Ultimately, the maximum H_2 production rate of composites reached to $171 \mu\text{mol g}^{-1} \text{h}^{-1}$ (9.1 times higher than pure $\text{g-C}_3\text{N}_4$) in methanol aqueous. Considering the relatively wide bandgap, $\text{g-C}_3\text{N}_4$ as a main component might hinder the visible light response potential of these composites. Thus, the $\text{Zn-AgIn}_5\text{S}_8$ QDs as a main component were combined with $\text{g-C}_3\text{N}_4$ to enhance the light absorption ability by Yang and co-workers.^[144] Pt was used as an additional cocatalyst to accelerate the reaction kinetics of H_2 production as well. With the excellent light absorption properties and the highly photogenerated charges separation efficiency by a tighter interface contact from $\text{Zn-AgIn}_5\text{S}_8$ QDs and $\text{g-C}_3\text{N}_4$, H_2 production efficiency of composites reached to $346.4 \mu\text{mol g}^{-1} \text{h}^{-1}$. Besides, Na_2SO_3 and Na_2S were employed as sacrificial reagents to consume photogenerated holes and prevent the photocatalyst from photo-corrosion. Ultimately, the H_2 production rate of composites exhibited no obvious reduction during three H_2 production cycles in 15 h (Figure 10B). It could be seen that noble metals (Pt, Ag, etc.) were widely supported in composites for efficient H_2 production.^[56,70] However, because of the high price as well as low reserves of noble metals, the search for alternatives or cocatalysts without the use of noble metals remains an ongoing task.^[143,145]

Recent progress has been made in photocatalytic H_2 production by combining some QDs as a cocatalyst with $\text{g-C}_3\text{N}_4$, solving the problems of noble metals.^[41,43,52,69,95] In consideration of Ti_3C_2 QDs with high conductivity and abundant active edge sites, Li et al. prepared a novel Ti_3C_2 QDs/ $\text{g-C}_3\text{N}_4$

Table 2. Summary of the QDs/g-C₃N₄ composites for H₂ production.

Composites	Synthetic method	Conditions	H ₂ production rate [μmol h ⁻¹ g ⁻¹]	Stability and reusability	Refs.
Ag QDs/g-C ₃ N ₄	One-step calcination method	50 mg of catalyst, 200 mL of 20% methanol aqueous solution; 300 W Xe lamp (λ > 420 nm)	HER: 18.09	a maintained hydrogen production performance in a 10 h continuous reaction (three recycles)	[73]
Ag ₂ S QDs/g-C ₃ N ₄	Self-assembly method	30 mg of catalyst, 100 mL of aqueous solution with 10 vol% triethanolamine (TEOA); 300 W Xe lamp (λ > 420 nm)	HER: 471.1	Slight decrease of hydrogen evolution activity of the sample after the accumulation of cycle times	[147]
CdS QDs/g-C ₃ N ₄	Chemical impregnation method	100 mg of catalyst, 120 mL of 25% methanol aqueous solution; 300 W Xe lamp (λ > 400 nm); loaded Pt	HER: 172.7	No obvious decrease of H ₂ evolution after irradiation for 28 h; no significant change in the XRD patterns of the catalyst after reaction	[49]
Cd _{0.5} Zn _{0.5} S QDs/g-C ₃ N ₄	Hydrothermal method	20 mg of catalyst, 100 mL of 0.35 M Na ₂ S and 0.15 M Na ₂ SO ₃ aqueous solution; 300 W Xe lamp (λ = 450 ± 20 nm)	HER: 33410	No obvious decrease in the H ₂ generation rate after five recycles; no detectable change in chemical state and morphology of the sample	[59]
MoS ₂ QDs/g-C ₃ N ₄	Wetness impregnation method	50 mg of catalyst, 90 mL of deionized water, 10 mL of TEOA; 300 W Xe lamp (λ > 420 nm); loaded Pt	HER: 393.2	The average H ₂ evolution rate maintained after 12 h cycle experiment	[148]
MoS ₂ QDs/g-C ₃ N ₄	One-pot hydrothermal process	50 mg of catalyst, 120 mL of 25% methanol aqueous solution; 300 W Xe lamp (λ > 420 nm); loaded Pt	HER: 363.9	Only a slight decrease of photocatalytic H ₂ evolution after three recycling runs, no apparent change in the XRD and FT-IR patterns of the catalyst after reaction	[65]
MoS ₂ QDs/ 3D spongy-like g-C ₃ N ₄	Photoassisted reduction method	50 mg of catalyst, 100 mL of 10 vol% lactic acid solution; 300 W Xe lamp (λ > 400 nm)	HER: 817.1	A negligible decrease of H ₂ evolution rate by the reaction after 12 hours reaction	[103]
1T-MoS ₂ QD/C ₃ N ₄ NRs	Sonication-assisted hydrothermal method	20 mg of catalyst, 100 mL of 20 vol% TEOA aqueous solution; 300 W Xe lamp (λ > 420 nm)	HER: 565	No obvious decay of photocatalytic activity under prolonged simulated solar light irradiation for 21 h; no obviously change of structure in XPS patterns of the catalyst after the reaction	[95]
1T-MoS ₂ QDs/g-C ₃ N ₄	Ultrasonic mixing method	20 mg of catalyst, 100 mL of 20 vol% TEOA aqueous solution; 300 W Xe lamp (λ > 420 nm)	HER: 1857	No obvious decay of photocatalytic activity under prolonged simulated solar light irradiation	[43]
NiS ₂ QDs/g-C ₃ N ₄	A seed-mediated hydrothermal method	5 mg of catalyst, 36 mL of water and 4 mL of TEOA in a solution; 300 W Xe lamp (λ > 420 nm)	HER: 968.2	A continuous H ₂ evolution without notable deactivation during a consecutive 15 h photocatalytic reaction	[104]
Ti ₃ C ₂ MXene QDs/g-C ₃ N ₄	Self-assembly method	10 mg of catalyst, 100 mL of 15% aqueous TEOA solution; 300 W Xe lamp (λ > 420 nm)	HER: 5111.8	A slight decrease of the H ₂ generation rate after three runs of catalyst	[41]
Cd _{0.5} Zn _{0.5} S QDs/ honeycomb-like g-C ₃ N ₄	In situ precipitation method	10 mg of catalyst, 100 mL deionized water that contained Na ₂ S (0.25 M) and Na ₂ SO ₃ (0.35 M); 300 W Xe lamp (λ > 420 nm)	HER: 5145	No noticeable decrease of H ₂ evolution rate by the reaction for four cycles	[112]
Ni ₂ P QDs/g-C ₃ N ₄	Evaporative deposition combined calcination method	20 mg of catalyst, 20 mL of 20% TEOA aqueous solution; 300 W Xe lamp (λ > 420 nm)	HER: 1503	No obvious decrease of the H ₂ generation rate after five runs, the no change of microstructure in the TEM patterns of the catalyst after reaction	[42]
CoP QDs/g-C ₃ N ₄	Deposition method	10 mg of catalyst, 70 mL water containing 10 mL of TEOA; 350 W Xe lamp (λ > 420 nm)	HER: 936	–	[52]
CoP QDs/g-C ₃ N ₄ fiber	Deposition and then low temperature phosphatization treatment	20 mg of catalyst, 80 mL of 15% TEOA solution; 300 W Xe lamp (λ > 420 nm)	HER: 2420	The maintained catalytic activity as high as 95.6% after nine cycles, no obviously change in the HRTEM, SEM and XPS patterns of the catalyst after the cycling experiment	[69]

Table 2. Continued.

Composites	Synthetic method	Conditions	H ₂ production rate [$\mu\text{mol h}^{-1} \text{g}^{-1}$]	Stability and reusability	Refs.
CQD/g-C ₃ N ₄ nanotubes (CCTs)	Polymerization method	50 mg of catalyst, 80 mL of 25 vol% methanol aqueous solution; 300 W Xe lamp ($\lambda > 400 \text{ nm}$)	HER: 3538.3	The maintaining significant leveling-off tendency over four cycles for 20 h	[149]
CN QDs/g-C ₃ N ₄	Impregnation-precipitation method	20 mg of catalysts, 50 mL of 10 vol% TEOA aqueous solution; 300 W Xe lamp ($\lambda > 420 \text{ nm}$)	HER: ≈ 300	A continuous H ₂ evolution without obvious loss during the reaction process	[150]
SnO ₂ -ZnO QDs/g-C ₃ N ₄	In situ copolyolysis method	5 mg of catalyst, 50 mL of 5% aqueous glycerol solution with vigorous; 300 W Xe lamp (Max 303 model) ($\lambda > 400 \text{ nm}$)	HER: 13673.61	Identical amounts of H ₂ produced in all five successive experiments; no change in the morphology and crystallinity after the recycling experiments by HRTEM and XRD	[151]
CeO ₂ QDs/S-g-C ₃ N ₄ (nanotubes)	In situ deposition-precipitation method	50 mg of catalyst, 100 mL of 20 vol% TEOA aqueous solution; 300 W Xe lamp ($\lambda > 420 \text{ nm}$)	HER: 2923.8	The amount of H ₂ increased linearly within 14 h of visible light irradiation, unchanged crystal structure, morphology, and chemical states of catalyst after photocatalytic reaction	[70]
CoO QDs/g-C ₃ N ₄	One-step calcination method	5 mg of catalyst, 100 mL of 10 vol% TEOA solvent water; 300 W Xe lamp ($\lambda > 420 \text{ nm}$)	HER: 11495	No apparent deactivation in the hydrogen evolution rate of catalyst after four recycles	[75]
Co ₃ O ₄ QDs/g-C ₃ N ₄	Evaporation deposition and annealing method	50 mg of catalyst, 100 mL buffered solution (the mixture of 0.022 M Na ₂ SiF ₆ and 0.028 M NaHCO ₃); 300 W Xe lamp ($\lambda > 420 \text{ nm}$)	oxygen evolution reaction (OER)	-	[78]
TiO ₂ QDs/g-C ₃ N ₄ NSs	Multi-step assembly method	50 mg of catalyst, 50 mL of 10 vol% TEOA aqueous solution; 300 W Xe lamp ($\lambda > 400 \text{ nm}$)	HER: 6308	Without obvious decrease of the cumulative H ₂ evolution in repeated runs; no noticeable change in the XRD, XPS, and FT-IR measurements after photocatalytic reaction	[90]
CdS QDs/P-g-C ₃ N ₄	In situ oil bath method	10 mg of catalyst, 100 mL aqueous solution having Na ₂ S (0.35 M) and Na ₂ SO ₃ (0.35 M); 300 W Xe lamp ($\lambda > 420 \text{ nm}$)	HER: 1579	The maintained H ₂ evolution rate of catalyst after 15 h reaction	[85]
CdS QD/MoO ₃ -OV/g-C ₃ N ₄	Microwave method	0.25 M Na ₂ S/Na ₂ SO ₃ ;	HER: 294.32	The amount of H ₂ generation maintained the proportionality for each 7 h continuous irradiation time, no obviously change of crystal structure in XRD patterns of the catalyst after the reaction	[152]
CdSe QDs/g-C ₃ N ₄	-	5 mg of catalysts, 10 mL of the water, 0.1 M L-ascorbic acid; 500 W high-pressure Hg lamp ($\lambda > 420 \text{ nm}$)	HER: 615	A steady increase of photocatalytic H ₂ under continuous illumination for 12 h and a maintained rate after three cycles; no apparent change of crystal structure after photocatalytic reaction	[113]
CdSe QDs/TF-g-C ₃ N ₄	In situ growth technique	5 mg of catalyst, 20 mL aqueous solution of 0.1 M Na ₂ S electrolyte and 0.1 M Na ₂ SO ₃ ; 400 W Xe lamp ($\lambda > 420 \text{ nm}$)	HER: 31000	No visible decrease in the performance and maintaining the H ₂ evolution rate during three successful repetitions	[133]
WS ₂ /CdSe QDs/g-C ₃ N ₄	Chemical impregnation method	10 mg of catalyst, 20 mL of 10% TEOA aqueous solution; 300 W Xe lamp ($\lambda > 420 \text{ nm}$)	HER: 1174.5	The almost unchanged H ₂ evolution rate after four runs under visible light irradiation	[67]
CdSe QD/B-rGO/O-g-C ₃ N ₄	Self-assembly method	30 mg of catalyst, 120 mL of aqueous solution containing 0.1 M ascorbic acid (AA); Xe arc lamp (CHF-XM-500 W) ($\lambda > 400 \text{ nm}$)	HER: 1435	-	[51]
TiO ₂ /CQDs/g-C ₃ N ₄	Impregnation method	50 mg of catalyst, 100 mL deionized water; 300 W Xe lamp ($\lambda > 400 \text{ nm}$)	HER: 6.497	-	[153]
TiO ₂ -x nanobelts/CdS QDs/g-C ₃ N ₄	Calcination-chemical bath deposition method	100 mg of catalyst, 100 mL of 20% methanol/H ₂ O solution; 300 W Xe lamp ($\lambda > 420 \text{ nm}$)	HER: 2233	No significant loss of activity after four texts	[154]

Table 2. Continued.

Composites	Synthetic method	Conditions	H ₂ production rate [$\mu\text{mol h}^{-1} \text{g}^{-1}$]	Stability and reusability	Refs.
NCDS/MoS ₂ QDs/g-C ₃ N ₄	Self-assembly and solvothermal methods	50 mg of catalyst, 100 mL of 10 vol% TEOA water; 300 W Xe lamp ($\lambda > 420 \text{ nm}$)	HER: 212.41	No obvious decrease of the photocatalytic hydrogen evolution activity after for four consecutive cycling photocatalytic experiments	[50]
Zn-AgIn ₅ S ₈ QDs/g-C ₃ N ₄	In situ hydrothermal method	50 mg of catalyst, 100 mL aqueous solution of 0.25 M Na ₂ SO ₃ and 0.35 M Na ₂ S; 300 W Xe lamp ($\lambda > 420 \text{ nm}$); loaded Pt	HER: 346.4	No obvious reduction of H ₂ evolution rate during three photocatalytic hydrogen production cycles in 15 h	[144]
Ti ³⁺ -TiO ₂ /MoS ₂ QDs/g-C ₃ N ₄ hollow nanosphere	Chemical template deposition and sculpture-reduction processes	50 mg of catalyst, 100 mL of 10 vol% TEOA aqueous solution; 300 W Xe lamp ($\lambda > 420 \text{ nm}$)	HER: 1524.37	A decent cycling stability and a higher average in consecutive 30 h (six cycles) photocatalytic hydrogen production process	[116]
SnO ₂ QDs/AgVO ₃ /g-C ₃ N ₄	Hydrothermal method	5 mg of catalyst, 50 mL aqueous solution containing 0.25 mol L ⁻¹ of each Na ₂ SO ₃ and Na ₂ S, 300 W Xe lamp ($\lambda > 420 \text{ nm}$)	HER: 9500	The highly stable with recyclability of catalyst after five successive cycles.	[61]
Ag/CQDs/g-C ₃ N ₄	Polymerization method	5 mg of catalyst, 70 mL water solution containing 10 mL TEOA; 300 W Xe lamp ($\lambda > 420 \text{ nm}$);	HER: 626.93	No distinguishable discrepancy in catalytic effect after four periods under visible light illumination; no obvious differences in the XRD patterns and FT-IR spectra of 3SCCN before and after the circulation test	[155]
xCo(dcbpy) ₂ (NCS) ₂ /CQDs/CN	Ultrasonic assisted method	50 mg of catalyst, 100 mL of 10 vol% TEOA solvent water; 300 W Xe lamp (PLS-SXE 300/300UV) ($\lambda > 420 \text{ nm}$)	HER: 295.9	Slight decrease in catalytic effect after four cycles in 16 h under visible light illumination	[156]
CQDs/Cl/3DOM-CN	Impregnation method	30 mg of catalyst, 100 mL of aqueous solution with 10 vol% TEOA and 2 wt% Pt; 250 W Xe lamp ($\lambda > 420 \text{ nm}$)	HER: 8120	No significant decrease for the photocatalytic activities of the sample after four cycles experiment	[157]
MoC QDs/carbon film/g-C ₃ N ₄ (3D)	Ultrasonic evaporation assisted method	30 mg of catalyst, 10 mg Eosin Y (EY) and 30 mL of 15% v/v TEOA solution; 300 W Xe lamp ($\lambda > 420 \text{ nm}$)	HER: 300.9	–	[158]
MoC QDs-C/g-C ₃ N ₄ (MCCN)	Self-assembly method	20 mg of catalyst, 100 mL of aqueous solution with 10 vol% TEOA; 300 W Xe lamp ($\lambda > 420 \text{ nm}$)	HER: 2989	Without any significant decrease of reproducible photocatalytic activity in four cycling tests; no noticeable change in the XRD characterization before and after the photocatalytic stability test	[159]

composite for H₂ production by a simple self-assembly method.^[41] The tiny size of Ti₃C₂ QD attained a larger specific surface area (40.149 m² g⁻¹) with abundant active sites. Furthermore, the photogenerated electrons could be transferred from g-C₃N₄ to Ti₃C₂ QDs, which quickly participated in H₂ production on the active sites of Ti₃C₂ QDs (Figure 10E). The optimized Ti₃C₂ QDs/g-C₃N₄ composite achieved a significantly photocatalytic H₂ yield (Figure 10C,D), which was nearly three-fold higher than Pt/g-C₃N₄. Also, a trigonal phase MoS₂ (1T-MoS₂) has the unique edge activity, dense active sites as well as the excellent electrical conductivity.^[131] Thus, Liang et al. loaded a number of 1T-MoS₂ QDs on the edge of g-C₃N₄ (Figure 10F), which exposed abundant active sites and attained H₂ precipitation rate of 15% 1T-MoS₂ QDs/g-C₃N₄ up to 1857 $\mu\text{mol g}^{-1} \text{h}^{-1}$.^[43] The similar transition metal phosphates (like Ni₂P) in composites with g-C₃N₄, efficiently inhibited the recombination of photogenerated e⁻-h⁺ pairs, which endowed an excellent photocatalytic performance without noble metals.^[25,42,52,69] Apart from CQDs or GQDs considered as cocatalysts to enhance charge transfer ability, researchers have taken advantage of

their up-conversion properties, which stimulated composites to form more e⁻-h⁺ pairs.^[100,119,120]

Recently, a breakthrough study has found that the more uniform and ordered combination of QDs and g-C₃N₄ endowed better photocatalysis of the composite. Raheman and co-workers prepared a novel photocatalyst CdSe QDs supported on thiol (-SH) functionalized g-C₃N₄ sheets (TF-g-C₃N₄) for H₂ evolution.^[133] The strong affinity of the -SH group to CdSe QDs was beneficial to high coverage density and uniform dispersion of CdSe QDs, which endowed this system more light-absorption as well as the photogenerated e⁻-h⁺ pairs (Figure 11A-C). It was worth mentioning that the -SH group acted as a hole quencher and inhibited photogenerated e⁻-h⁺ pairs recombination. Both of them would promote high charge separation efficiency and endow an outstanding photocatalytic activity (31 000 $\mu\text{mol g}^{-1} \text{h}^{-1}$), which was almost 12.3 times greater than that of TF-g-C₃N₄. Therefore, the uniform and ordered combination of functionalized g-C₃N₄ gave the composite better photocatalytic effect, and similar strategies should be developed intensively.

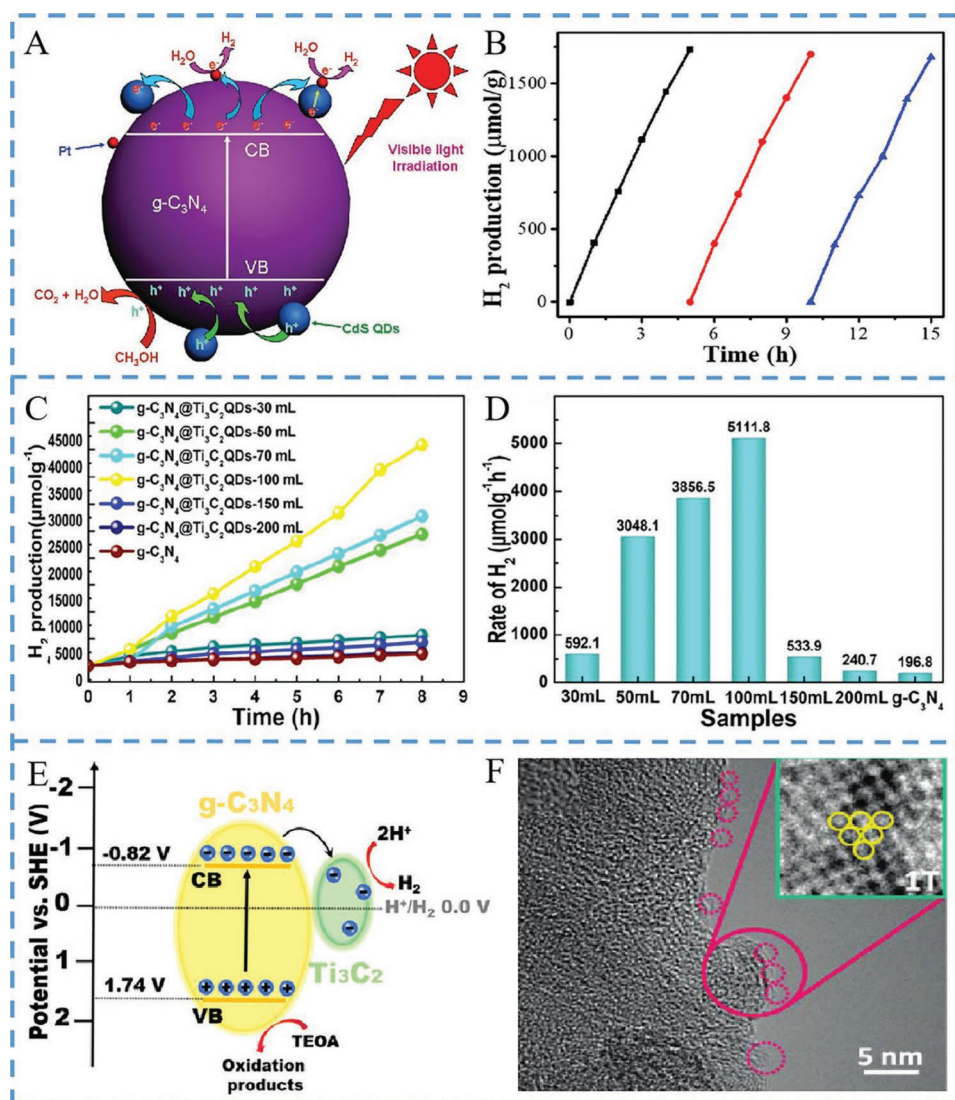
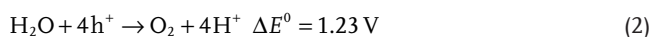
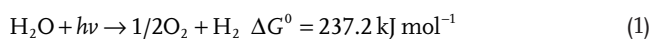


Figure 10. A) Schematic of photogenerated charge transfer in the CdS QDs/g-C₃N₄ system under visible light irradiation. Adapted with permission.^[49] Copyright 2012, Royal Society of Chemistry. B) Stability study of photocatalytic hydrogen production over the 0D/2D Zn-AgIn₅S₈/g-C₃N₄-10%nanocomposite. Adapted with permission.^[144] Copyright 2019, Elsevier. C) Photocatalytic H₂ evolution and D) rate of g-C₃N₄ NSs, Pt/g-C₃N₄, Ti₃C₂ MXene/sheet/g-C₃N₄, and g-C₃N₄@Ti₃C₂ QDs; E) schematic photocatalytic mechanism of g-C₃N₄@Ti₃C₂ QD composites. Adapted with permission.^[41] Copyright 2019, American Chemical Society. F) HRTEM image of 1T-MoS₂ QD@g-C₃N₄ composites (15 wt%) (inset shows the magnification of the region enclosed by the pink circle). Adapted with permission.^[43] Copyright 2019, Royal Society of Chemistry.

In general, photocatalytic water splitting should obtain sufficient energy to active reactions Equation (1). This is to say that the photons with $h\nu$ should be greater than or equal to the bandgap of photocatalysts. The water splitting involves two equations (Equations (2) and (3)).^[146]



G-C₃N₄ can satisfy the redox potential of water splitting, but its easy recombination of photogenerated e⁻-h⁺ pairs and the

limited visible light range have to be considered. The combination of QDs and g-C₃N₄ can solve these problems and brings a high H₂ production efficiency. Moreover, the use of cocatalyst such as noble metals reduce the excessive overpotential during the H₂ production process and enhances the photocatalytic performance of H₂ production.^[49,56,65,70] Interestingly, some QDs/g-C₃N₄ with high conductivity can endow photocatalytic performance corresponding to noble metal/g-C₃N₄ composites with high efficiency.^[25,41-43,52,69] The uniform load of QDs is also an effective way to promote H₂ production.^[133] The general mechanism of H₂ production is shown in Figure 11D. Under visible light, QDs/g-C₃N₄ composites produce e⁻-h⁺ pairs. Then, the photogenerated electrons transfer to QDs (abundant active sites) and even reach the additional cocatalysts, which finally

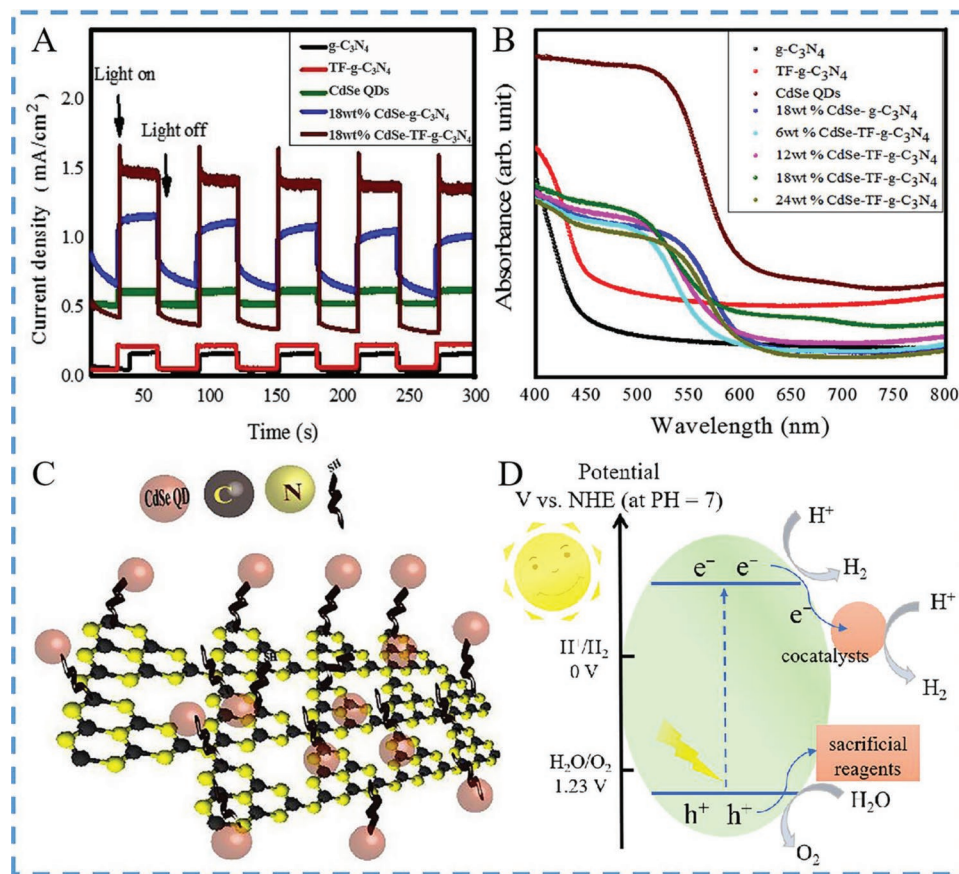


Figure 11. A) Transient photoelectrochemical activities of photocatalyst on-off cycles; B) UV-vis diffuse reflectance spectra (DRS) of as-prepared photocatalysts; C) schematic representation of CdSe QDs sensitized thiol-functionalized g-C₃N₄ sheet; D) the general mechanism of H₂ production by QDs/g-C₃N₄ composites. Adapted with permission.^[133] Copyright 2020, Elsevier.

reduce H⁺ to H₂. At the same time, the photogenerated holes can oxidize H₂O to produce O₂ or be consumed by sacrificial agents when H₂O cannot be oxidized.

4.2. H₂O₂ Production

Recently, H₂O₂ has been found to be promising as a substitute for H₂ due to its application in fuel cell energy carriers, which has attracted significant attention.^[160,161] Among the methods of H₂O₂ production, photocatalysis is considered as a superior method by reasons of its nonpolluting nature and safety.^[162] G-C₃N₄ has been an ideal materials for H₂O₂ production since water/alcohol was mixed with O₂ for selective formation of H₂O₂ under visible light in 2014.^[160,163,164] The latest reports show that a variety of QD/g-C₃N₄ composites have used the transformation of O₂ into H₂O₂ production.^[54,165,166]

For example, Yang et al. constructed a metal-free boron nitride QDs/ultrathin porous g-C₃N₄ (BNQDs/UPCN) photocatalyst by a facial stirring.^[165] Results demonstrated that the photogenerated electrons efficiently separated and transferred based on the BN QDs as cocatalysts as well as the ultrathin and porous nanostructure of g-C₃N₄ (Figure 12A,B). Moreover, isopropanol (IPA) was used to enhance the H₂O₂ production as a proton donor. Benefiting from these, the production of H₂O₂

reached to 72.3 μmol L⁻¹ h⁻¹ by a two-electron reduction of O₂ (O₂ + 2 H⁺ + 2 e⁻ → H₂O₂) because the negative CB level of BNQDs/UPCN (-0.95 V vs NHE) was more than the redox potential of O₂/H₂O₂ (0.69 V vs NHE).

Interestingly, some studies have demonstrated that photocatalytic H₂O₂ generation can also be achieved through two-step single-electron O₂ reduction reaction and even H₂O oxidation reaction by photogenerated holes. Chen et al. fabricated a Z-scheme photocatalyst of α-Fe₂O₃/CQDs@g-C₃N₄ in polyvinylpyrrolidone (PVP) solution through solvothermal method.^[54] Apart from a broad absorption range (up to 800 nm) of CQDs (Figure 12C), the composites load α-Fe₂O₃ QDs provided an efficient photocatalytic reaction. Results from various active species and rotating ring-disk electrode tests demonstrated that the high production of H₂O₂ in two-step single-electron (O₂ + e⁻ → ·O₂⁻, ·O₂⁻ + 2 H⁺ + e⁻ → H₂O₂) was substituted by α-Fe₂O₃/CQDs@g-C₃N₄. Moreover, the E(VB) of α-Fe₂O₃ QDs was more positive than E(H₂O₂/H₂O) (1.76 V vs NHE), so the photogenerated holes on α-Fe₂O₃ QDs might oxidize H₂O to H₂O₂ as schematically illustrated in Figure 12D. In this system, H₂O and O₂ were converted to H₂O₂, avoiding the use of sacrifice agents and reducing costs.

Recently, it has been found that although composites have good photocatalytic performance, the lattice and band mismatch between two materials still hinder the separation and

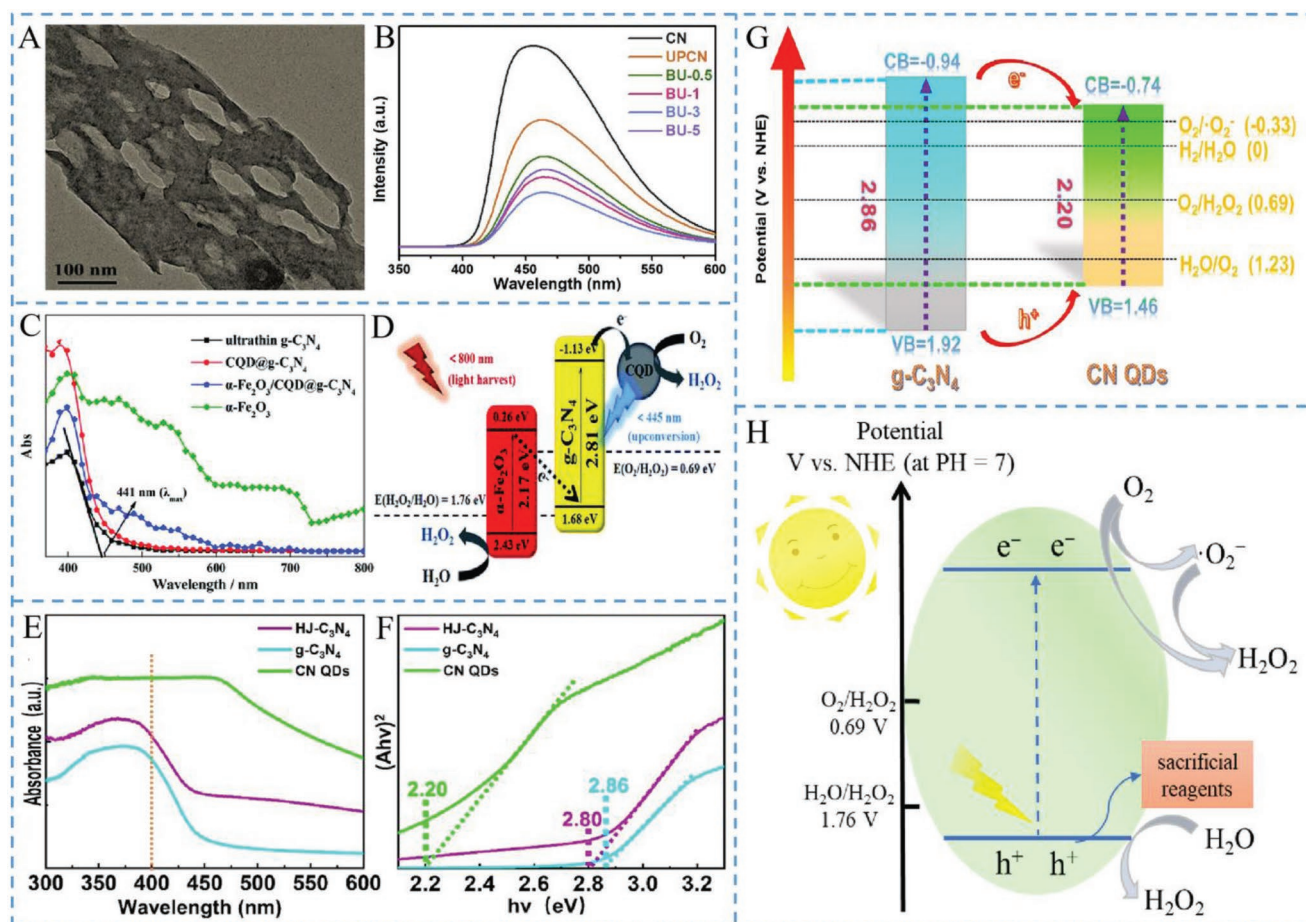


Figure 12. A) TEM images of BU-3; B) steady-state photoluminescence spectra. Adapted with permission.^[165] Copyright 2018, Elsevier. C) UV-vis DRS spectra of g-C₃N₄, CQD@g-C₃N₄, α-Fe₂O₃/CQD@g-C₃N₄, and α-Fe₂O₃; D) the photocatalytic H₂O₂ generation mechanism of α-Fe₂O₃/CQDs@g-C₃N₄ featuring the Z-scheme charge transfer route. Adapted with permission.^[54] Copyright 2020, Royal Society of Chemistry. E) (A·hν)² versus hν curve and F) UV-vis absorption spectra of CN QDs, bare g-C₃N₄, and HJ-C₃N₄; G) the estimated energy band structure of CN QDs and bare g-C₃N₄; H) the general mechanism of H₂O₂ production by QDs/g-C₃N₄ composites. Adapted with permission.^[166] Copyright 2021, Elsevier.

transport of photogenerated e⁻-h⁺ pairs. To overcome the incompatibility of different materials, Ma et al. constructed a novel 0D CN QDs/g-C₃N₄ homogeneous junction (HJ-C₃N₄) by a calcination method. The composites were first applied to H₂O₂ production with a yield of 115 μmol L⁻¹ h⁻¹ (the highest yield among non-metallic materials) by a two-electron O₂ reduction reaction.^[166] The type-I homojunction (Figure 12G) without a Schottky barrier was more conducive to the rapid separation of carriers compared with the traditional type-I heterojunction. Furthermore, O₂ was introduced into CN QDs during the calcination process. Thus, the oxygen-containing groups in CN QDs caused the defective energy level, which endowed CN QDs the advantages of capturing photogenerated electrons and inhibiting the recombination of e⁻-h⁺ pairs. The CN QDs with narrow bandgap supplied a benefit of unique light absorption performance and up-conversion effect, exhibiting the better light absorption range and light absorption capacity of HJ-C₃N₄ (Figure 12E,F). Furthermore, HJ-C₃N₄ had a high stability after four cycle experiments. All above fully reflected that the HJ-C₃N₄ obtained by green and simple method had a promising application prospect.

Typically, the photocatalytic reduction of O₂ to H₂O₂ needs the addition of sacrificial agents as proton donors (mainly alcohols), which increases the cost of H₂O₂ production.^[54,165,166] Currently, the reduction of O₂ and H₂O to H₂O₂ is a way that avoids the use of sacrificial agents. However, the H₂O₂ production with sacrificial agents is more efficient than the system without sacrificial agents.^[54,167] Although researchers have made many efforts, there are still many challenges. Therefore, more experimental and theoretical works are needed to further reveal the mechanism of reaction and improve the efficiency of H₂O₂ production without sacrificial agents. The probable mechanism of photocatalytic H₂O₂ production is demonstrated in Figure 12H. Under visible light, g-C₃N₄ and even QDs are photogenerated to produce e⁻-h⁺ pairs as well as the photo-generated electrons transferred to the CB of g-C₃N₄/QDs. The active electrons in CB reduce O₂ to H₂O₂ by two-electron (O₂ + 2 H⁺ + e⁻ → H₂O₂) or two-step single-electron (O₂ + e⁻ → ·O₂⁻, ·O₂⁻ + 2 H⁺ + e⁻ → H₂O₂) reaction, while the CB level of composites is negative than O₂/H₂O₂ (0.69 V vs NHE). Moreover, when the VB level of composites is positive than H₂O/H₂O₂ (1.76 V vs NHE), the active holes in VB oxidize H₂O to H₂O₂.

by directly oxidation reaction ($2 \text{H}_2\text{O} + 2 \text{h}^+ \rightarrow \text{H}_2\text{O}_2 + 2 \text{H}^+$), or else react with sacrificial agents.

4.3. CO₂ Reduction

Spurred by the exhaustion of fossil fuel resources and the excessive CO₂ emission, the utilization of CO₂ as feedstock for the production of chemical fuels has been investigated worldwide.^[168,169] Since Inoue and co-workers first attempted it in 1979s,^[170] artificial photosynthesis has been widely used in the photocatalytic conversion of CO₂ and considered as a promising way to sustainably recycle of CO₂ under green conditions.^[168,169] Theoretically, g-C₃N₄ exhibits a π -conjugated structure on its surface, which can be used for CO₂ reduction by absorbing CO₂ through π - π interactions.^[171] Nevertheless, the lack of CO₂ adsorption and activation sites, slow surface reaction kinetics and inefficient charge separation are the main obstacles for g-C₃N₄ to reduce CO₂.^[172] Recently, challenges have been addressed in the reduction of CO₂ to CH₄ and/or CO by using QD/g-C₃N₄ composites, and the corresponding studies are summarized in Table 3.

For instance, Li et al. demonstrated oxygen-doping CN (OCN) decorated with CQDs exhibited a higher CH₄ production (14 times) than pure CN.^[172] The results showed that the CQD/OCN-25% and OCN-25% exhibited the stronger physically absorbed CO₂ on the relatively weak basic sites. Moreover, CQDs played a role of accelerating the charge transfer and providing abundant active sites to the activation process of CO₂. Ultimately, the OCN with high nitrogen defects facilitated the dissociation of H₂O to supply more H⁺, which provided an important prerequisite and accelerated the reaction

kinetics for the higher selective production (70%) of CH₄ (Figure 13A).

Besides, the adsorption of CO₂ is a major process and prerequisite for reducing CO₂ via the photocatalyst. Researchers found that the 3D porous g-C₃N₄ material showed convenient transfer channels, long contact times and good CO₂ absorption capacity.^[173] To achieve higher CO₂ conversion efficiency, Sun et al. exploited a novel Z-scheme heterojunction Cu₂O QDs/3D g-C₃N₄ foam (CFC) composite through a simple photo-deposition treatment.^[53] On the one hand, the 3D g-C₃N₄ foam endowed QDs with a carrier, which greatly improved the performance of CO₂ adsorption and mass transfer properties as well as enhanced the excellent photocatalytic activity (Figure 13B–D). On the other hand, the Cu₂O QDs loading on the 3D g-C₃N₄ foam caused a slight decrease in CO₂ adsorption due to the inevitable disruption of the framework structure of the foam. However, the Cu₂O QDs acted as an effective electron store to accelerate the charge carrier transfer and provided active sites for the reduction of CO₂ (Figure 13E,F). All samples could achieve the thermodynamic requirements (reducing CO₂ to CO) in terms of their strong reducibility. Eventually, the Cu₂O QDs/g-C₃N₄ foam exhibited CO, CH₄ production rate arriving 8.182 $\mu\text{mol g}^{-1} \text{h}^{-1}$ and 0.0805 $\mu\text{mol g}^{-1} \text{h}^{-1}$, respectively, which was 3.9-fold and 11-fold higher than that of g-C₃N₄ foam. Compared with CQDs/OCN, this composite showed the higher production of CO than CH₄. This is because the conversion of CO₂ to CO needs only 2-electron, while the conversion of CO₂ to CH₄ needs 8-electron, making it easier to form CO rather than CH₄.

In recent years, the emergence of density functional theory (DFT) provides a clearer and more intuitive explanation for the mechanism of reaction. Gong and co-workers constructed

Table 3. Summary of the QDs/g-C₃N₄ composites for CO₂ reduction.

Composites	Synthetic method	Conditions	Reduced productions [$\mu\text{mol h}^{-1} \text{g}^{-1}$]	Stability and reusability	Refs.
CsPbBr ₃ QDs/g-C ₃ N ₄	Self-assembly method	8 mg of catalysts; 30 mL of acetonitrile/ethyl acetate with 100 μL of deionized water	148.9 (CO)	No obvious changes of XRD patterns and FTIR spectra of catalysts before and after stability test	[115]
Cu ₂ O QDs/ g-C ₃ N ₄ foam	Photodeposition method	50 mg of catalysts; 10 mL of water	8.182 (CO) 0.0805 (CH ₄)	No significant decrease of photocatalytic activity after five continuous cycles	[53]
rGO/g-C ₃ N ₄ QDs/g-C ₃ N ₄ NFs	Hydrothermal method	15 mg of catalysts; 30 mL of Na ₂ CO ₃ solution (0.01 M)	170 (HCHO)	No significant loss in activity even after the fourth cycle	[175]
CQDs/O-g-C ₃ N ₄	One-pot hydrothermal approach	50 mg of catalysts; water	1.73 (CO) 0.15 (CH ₄)	The identical FTIR spectra of the sample before and after the photocatalytic reactions	[172]
CdSe QDs/ P doped g-C ₃ N ₄	Self-assembly method	50 mg of catalysts; 3 mL of water	25 (CO) 48 (CH ₄)	No deactivation even after 6 runs each of 7 h	[45]
Bi ₂ S ₃ QDs/g-C ₃ N ₄	Hydrothermal process	50 mg of catalysts; 100 mL deionized water	6.84 (CO) 1.57 (CH ₄)	The stable yield of CO during three experimental runs	[60]
NiS ₂ QDs/ g-C ₃ N ₄	Hydrothermal process	50 mg of catalysts; 100 mL deionized water	10.68 (CO)	No obvious structural change and deactivation after three cycling tests for 15 h	[48]
InVO ₄ QDs/CN	Chemical solution growth method	5 mg of catalysts; 10 mL of mixed solvents (acetonitrile/water = 2:3), 2 mL of TEOA	69.8 (CO)	The negligible decline and no change of morphology after 4 consecutive cycles for 40 h	[94]

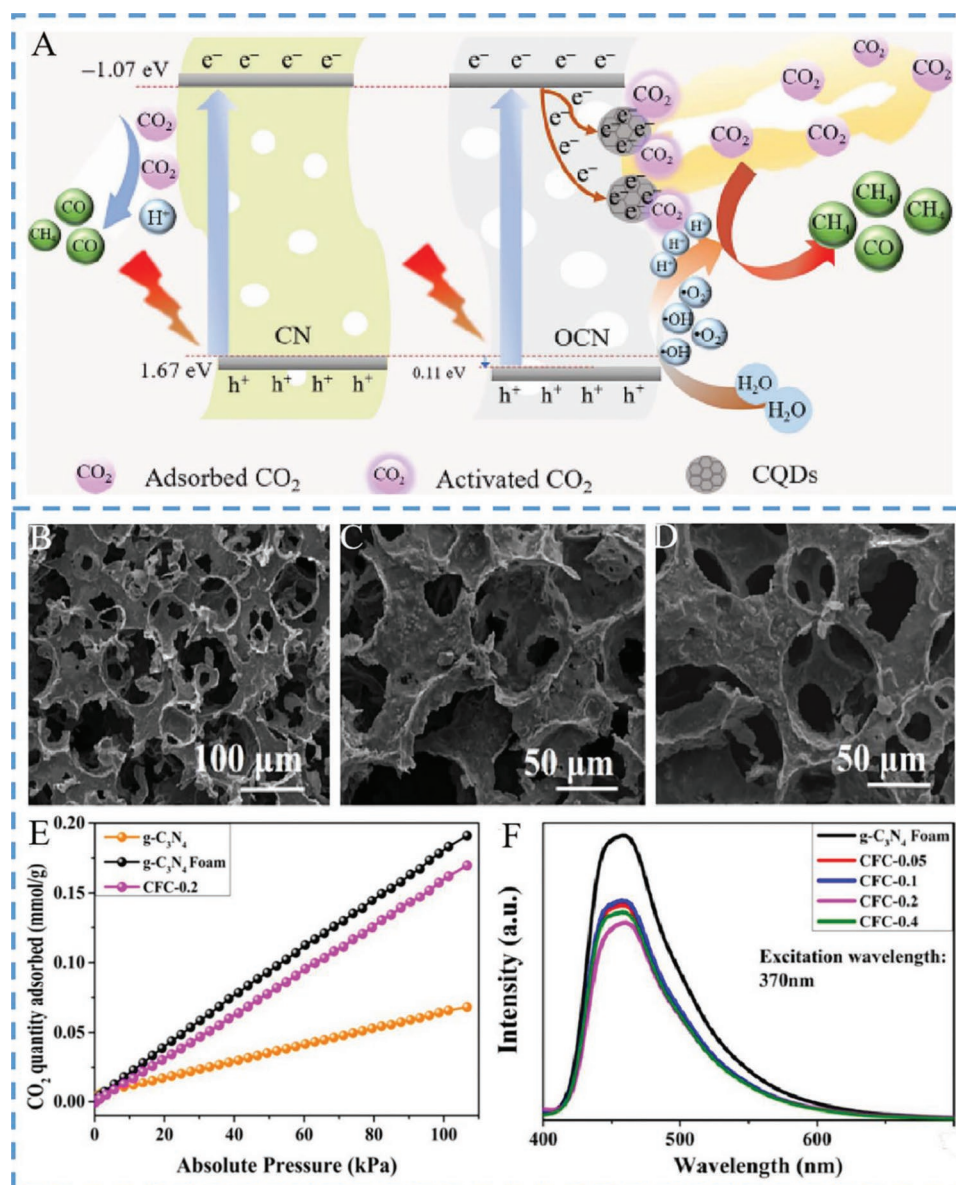
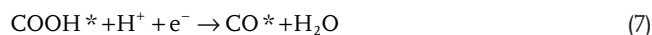
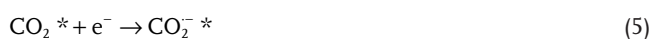


Figure 13. A) The schematic mechanism of CO₂ photocatalytic reduction over CQDs/OCN-x under visible light irradiation. Adapted with permission.^[172] Copyright 2019, Tsinghua University Press. SEM images of B) pure g-C₃N₄ foam, C) CFC-0.05, D) CFC-0.1; E) CO₂ quantity adsorbed of g-C₃N₄, g-C₃N₄ foam and CFC-0.2; F) the room-temperature PL spectrum of g-C₃N₄ foam and CFC samples. Adapted with permission.^[153] Copyright 2019, Elsevier.

InVO₄ QDs/g-C₃N₄ with S-scheme heterojunctions by a chemical solution growth method and produced a selective conversion of CO₂ to CO (93.3%) at a decent rate of 69.8 μmol g⁻¹ h⁻¹ under visible light irradiation.^[94] The reaction process for CO₂ reduction and the transport mechanism of InVO₄ QDs/g-C₃N₄ were discussed through DFT calculations for the adsorption energy and electronic structure. On the basis of experimental results and references, the reduction of CO₂ to CO was been proposed in Equations (4)–(8).^[94]



CO₂* adsorbed on the photocatalyst was activated to CO₂^{·-} and then combined with H⁺ to COOH*, which was proved as the main process in the whole CO₂ reduction. The final product CO* was formed through the combination of COOH* with e⁻–H⁺ pairs. The relative free energy (ΔG) of the g-C₃N₄ and InVO₄ QDs/CN for reduction of CO₂ to CO were shown in Figure 14A, from which it could be seen that the lower ΔG (-0.46 eV) of InVO₄ QDs/CN indicated its enhanced adsorption ability for

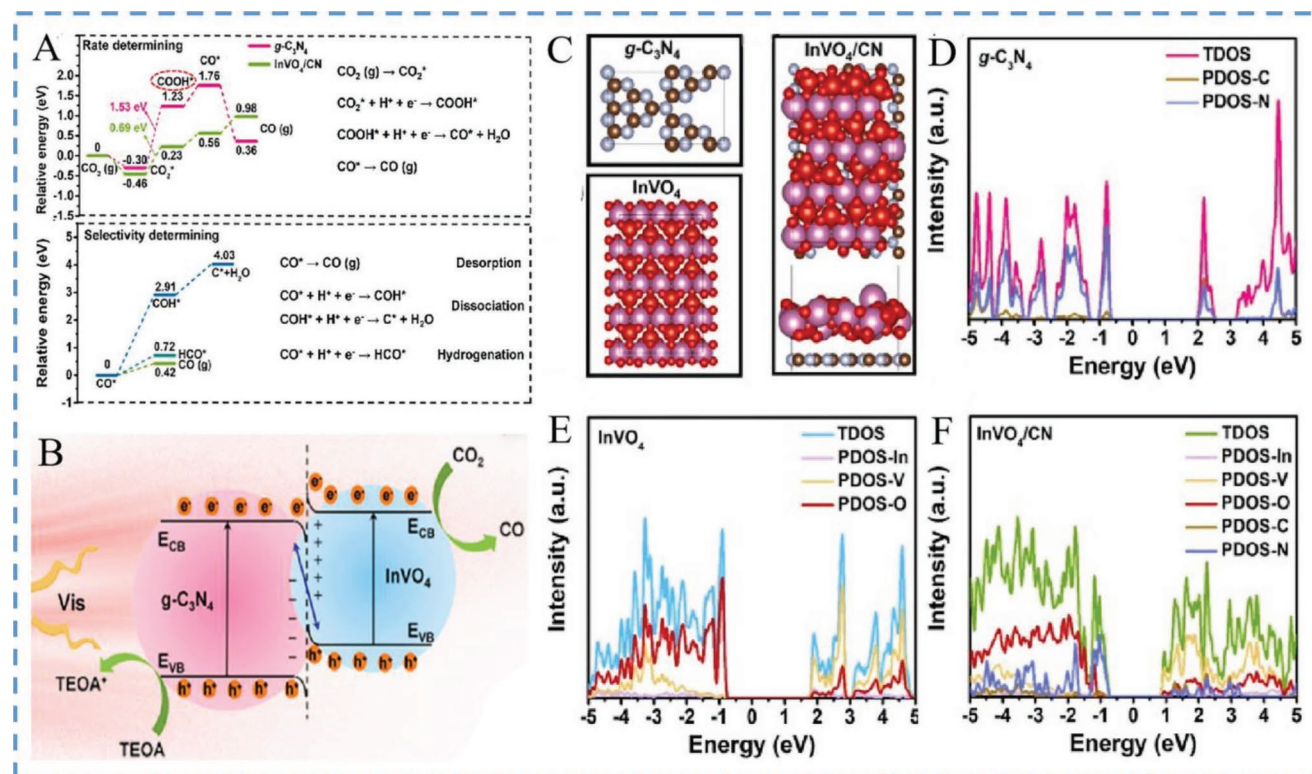


Figure 14. A) Relative free energy profiles for CO₂ reduction to CO: rate determining and Selectivity determining; B) the mechanism of S-scheme 0D/2D InVO₄/CN as a photocatalyst for CO₂ reduction; C) the simulation models of g-C₃N₄, InVO₄, InVO₄/CN heterostructure; the density of states of D) g-C₃N₄ atomic slab, E) InVO₄ atomic slab, and F) InVO₄/CN heterostructure. Adapted with permission.^[94] Copyright 2021, Elsevier.

CO₂. Obviously, the heterojunction of InVO₄ QDs/CN would reduce the activation energy barrier of CO₂. Moreover, the desorption of CO from the composites needed a lower energy (0.42 eV) than that for hydrogenation (0.72 eV) or dissociation (2.91 eV). Thus, CO would preferentially absorb from the composites instead of further reacting, which acted as the major products. The density of states (DOS) of g-C₃N₄, InVO₄ QDs and InVO₄ QDs/CN were calculated to insight into the electron-hole transport as well (Figure 14C–F). The author pointed out that the electronic structure of InVO₄ QDs/CN showed a considerable change and a narrow bandgap were brought on account of strong interface interaction. Based on the experimental analysis and DFT calculation, electrons were more easily transferred to CB for CO₂ reduction via the S-scheme heterostructure, which provided a strong driving force for CO₂ reduction (Figure 14B). This experiment exhibited a theoretical support for the photocatalytic process of CO reduction.

According to the previous studies, the reduction of CO₂ can be summarized as a multi-electron transfer process (Figure 15). In detail, the QDs/g-C₃N₄ photocatalysts are stimulated to produce e[−]–h⁺ pairs. Then, CO₂ absorbed on the surface can be reduced to other substances by the activated electrons. The possible reaction processes and corresponding redox potentials are listed below (Equations (9)–(13)).^[34,174] Therefore, increasing the adsorption capacity of CO₂, the number of activation sites and charge separation ability are the main ways to enhance the reduction efficiency of CO₂. Moreover, studies have found

that DFT calculation may provide a theoretical support for the photocatalytic process of CO reduction as much as possible.^[94] In the future, further combining experiments with DFT

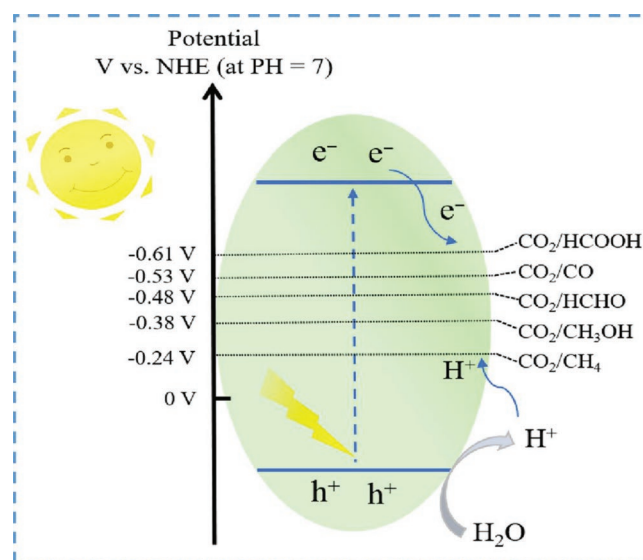
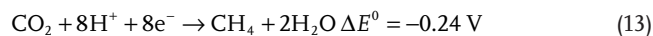
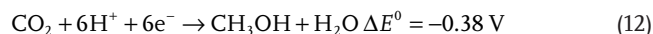
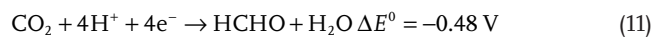


Figure 15. The general mechanism of CO₂ production by QDs/g-C₃N₄ composites.

calculation may be expected to design QDs/g-C₃N₄ photocatalysts with high yield and high efficiency for CO₂ reduction.



5. Applications of QDs/g-C₃N₄ Composites in Environmental Fields

Due to the quick development of society, industrial production and human activities have generated a large amount of pollution over the decades. The release of pollutants (e.g., organic pollutants, poisonous gas) has adversely affected on animal and human health and become a serious environment concern.^[9,176] It is reported that QDs/g-C₃N₄ composites also act as a vital role in the fields of environment (the treatment of pollutants) due to their excellent photocatalytic properties.

5.1. Organic Pollutants Degradation

Organic pollutants (e.g., antibiotics and dyes) in industrial wastewater are persistent, aquatic toxic, and mutagenic and of widespread concern for their adverse ecological effects.^[9] Photocatalysis has been widely used as an effective strategy for the degradation of organic pollutant. A large number of studies have shown that QDs/g-C₃N₄ composites are ideal photocatalysts for the removal of organic pollutants.

Fan et al. designed CdS QDs/nanoporous g-C₃N₄ (CdS QDs/png-C₃N₄) photocatalysts for rhodamine B (RhB) degradation.^[66] The composite achieved high degradation performance (close to 88.2%) because of the expanding light absorption range and efficient separation of e⁻-h⁺ pairs. This work illustrated the mechanism of CdS QDs/png-C₃N₄ for degradation under visible light irradiation as following (**Figure 16A**): i) photogenerated carriers separated and migrated under visible light irradiation (Equation (14)); ii) the photogenerated electrons captured O₂ to produce ·O₂⁻, which degraded RhB and finally generated CO₂ and H₂O (Equations (15) and (20)). However, the redox reactions of type-II heterojunction photocatalysts occur at lower potentials respectively, limiting the redox capacity. For purpose of enhancing the degradation efficiency of the composite by stronger redox capacity, Bi₃TaO₇ QDs/g-C₃N₄ nanosheets (NSs) with Z-scheme heterojunction was designed for antibiotic degradation by Wang and co-workers.^[80] Abundant ·OH and ·O₂⁻ as the main active substances were produced in the composite by effective Z-scheme charge transfer on the heterogeneous interface, shown in **Figure 16B**. Apart from that, due to excellent photoelectronic properties, noble

metals (Ag,^[56,177] etc.) and carbon material (CQDs,^[101,178,179] GQDs,^[119] etc.) were also used as cocatalysts to enhance the separation of photogenerated e⁻-h⁺ pairs and produce more active substances.

Due to the good light absorption performance of certain pollutants, there may be photosensitization between them after these pollutants being adsorbed by photocatalysts with relatively large specific surface area. Liu et al. composited CQDs/g-C₃N₄ composites via a facile polymerization method for the degradation of diclofenac (DCF) and showed a 100% removal efficiency within 60 min.^[178] **Figure 16C,D** shows that the C—O—C bond between CQDs and g-C₃N₄ provided the tight interface contact to transfer photogenerated electrons from DCF to g-C₃N₄, enhancing the photocatalytic activity of CNC. The activated electrons on CB of g-C₃N₄ reacted with O₂ to generate ·O₂⁻. Apart from most direct reactions with DCF, some of ·O₂⁻ will be converted to ·OH to degrade DCF. This mechanism might provide a new perspective for photocatalytic degradation reactions under visible light irradiation.

Interestingly, the photo-Fenton processes catalyzed by Fe-based QDs/g-C₃N₄ materials have been acted as an effective method for organic pollutant degradation.^[180] To explore the photocatalytic performance in the presence of H₂O₂, Qian et al. successfully coupled amorphous FeOOH QDs with g-C₃N₄ as a light-driven photo-Fenton photocatalyst for the degradation of methylene orange (MO).^[127] They proposed that g-C₃N₄ was excited to generate e⁻-h⁺ pairs under visible light, and then the photogenerated electrons partaken in the Fe(II)/Fe(III) cycle and produced ·O₂⁻ with O₂. More than that, the photogenerated electrons were also snatched by H₂O₂ (strong oxidant), which facilitated the generation of ·OH as well as the effective separation of photocarriers (Equation 16). Ultimately, the ·OH as the predominant oxidants, h⁺ and ·O₂⁻ contributed to degrade MO under visible light irradiation (**Figure 16E**). In the same year, Hao et al. constructed crystalline Fe₂O₃ QDs/g-C₃N₄ photocatalysts, which offered fast carriers transport ways through the tight interface contact between Fe₂O₃ QDs and g-C₃N₄.^[181] This composite endowed 85.2% degradation efficiency of MO by the same way.

However, these photocatalysts in powder state are tough to recycle from water treatments and lead to secondary pollution. Considering that, Zhu et al. fabricated magnetic QDs@Co-doped g-C₃N₄ (Fe₃O₄ QDs@Co-CN) composites for TC degradation.^[182] The authors pointed out that the red-shifted absorption edge of composites and the enhanced absorption capacity were ascribed to the Co doping effect reducing the bandgap and the quantum effect of Fe₃O₄QDs. More importantly, the reduced bandgap by Co doping promoted the rapid separation of e⁻-h⁺ pairs and the transferred photogenerated electrons to Fe₃O₄ QDs. Due to the synergistic effects of Co doping and the formation of Fe₃O₄ QDs, the composite showed excellent TC degradation efficiency (80.5%). Additionally, the magnetic Fe₃O₄ QDs@Co-CN could be easily recovered from solution and retained 79% degradation effect and magnetization saturation value (≈5.48 emu g⁻¹) after 4 cycles.

In fact, the additional H₂O₂ increases the cost and safety risks, limiting the photo-Fenton reaction. Recently, researchers have discovered generating and utilizing H₂O₂ in situ in Fenton system with ideal g-C₃N₄ materials could effectively

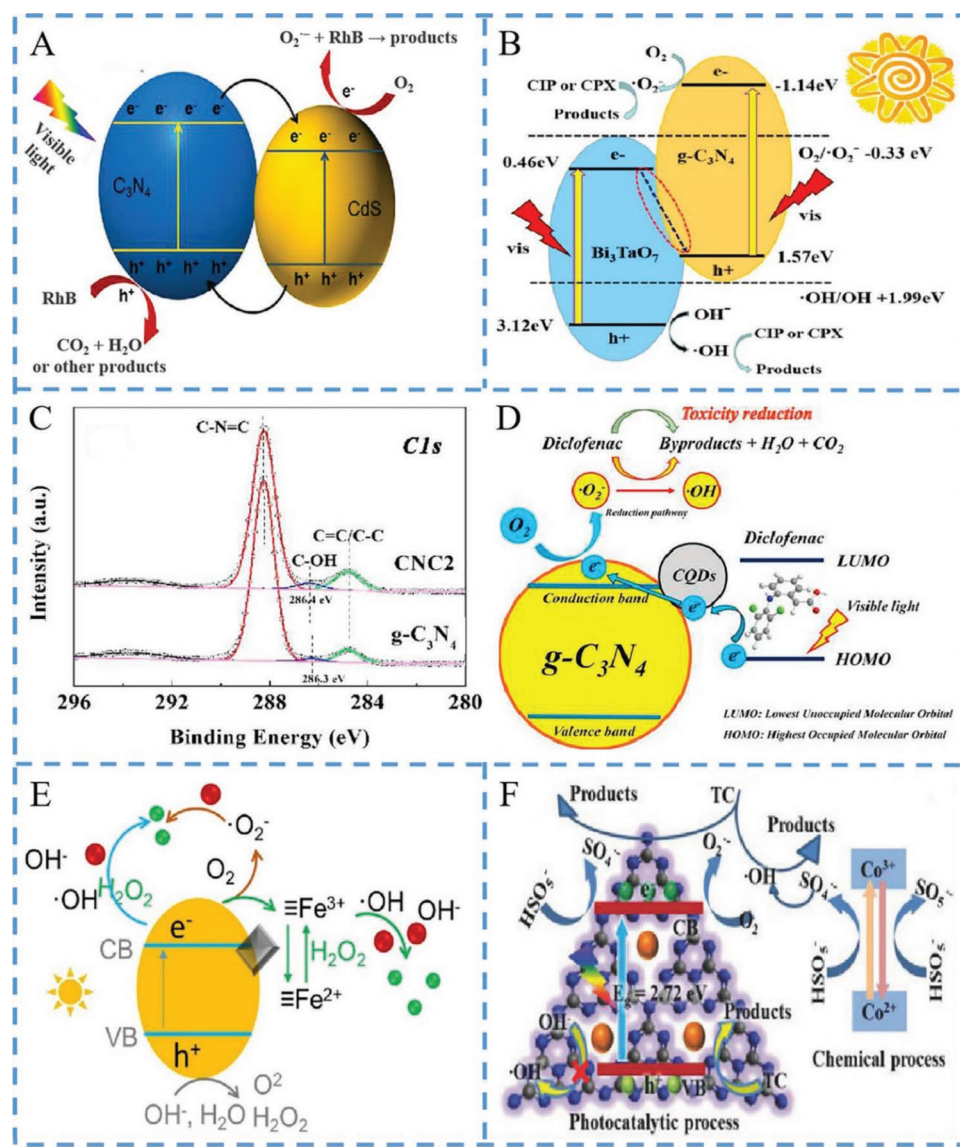


Figure 16. A) Schematic of photogenerated charge transfer in the CdS QDs/npg-C₃N₄ system under visible light. Adapted with permission.^[66] Copyright 2015, Elsevier. B) Z-scheme photocatalytic mechanism for Bi₃TaO₇ QDs/g-C₃N₄ NSs composite. Adapted with permission.^[80] Copyright 2017, American Chemical Society. C) The high-resolution XPS spectra of C 1s of pure g-C₃N₄ and CNC2. D) Schematic illustration of photosensitization-like degradation of DCF. Adapted with permission.^[178] Copyright 2018, Elsevier. E) A schematic illustration of visible light driving photo-Fenton oxidation of organic pollutants over FeOOH QDs coupled g-C₃N₄. Adapted with permission.^[127] Copyright 2018, Elsevier. F) Proposed catalytic degradation mechanism of Co₃O₄ QDs/CNNS in PMS/vis system. Adapted with permission.^[111] Copyright 2018, Wiley-VCH.

avoid this problem.^[161,164] Shi et al. utilized the coupling of FeOOH QDs and ultrathin porous g-C₃N₄ (UPCN) to degrade Oxytetracycline (OTC).^[161] On the one hand, the in-situ producing H₂O₂ of UPCN combining with FeOOH QDs formed the photo-Fenton system. On the other hand, the structure of UPCN accelerated the photogenerated electrons transferring to FeOOH QDs, which reduced Fe³⁺ to Fe²⁺ for participating in Fenton reaction. Under visible light, the produced H₂O₂ by 20% FeOOH/UPCN composites participated in photo-Fenton reaction to reach 86.23% removal efficiency within 120 min. These findings suggested that the combination of Fenton reaction and photocatalysis has an incredible effect on the degradation of pollutants, mainly due to H₂O₂ (oxides) for the

acquisition of electrons, which prompt the separation of photo-generated e⁻-h⁺ pairs.

To date, sulfate radicals (SO₄⁻) based advanced oxidation processes (SR-AOPs) have attracted extensive attention due to their adaptability and strong oxidation capacity.^[176,183,184] The combination of catalyst and peroxymonosulfate (PMS) or peroxydisulfate (PDS) is an effective measure to generate sulfate radicals (SO₄⁻) (Equations (17)–(19)).^[168]

For the sake of understanding the role of PMS in QDs/g-C₃N₄ system, Cao et al. prepared Co₃O₄ QDs/CNNS heterostructure photocatalyst for the degradation organic pollutant by activating PMS.^[111] The author investigated the main mechanism: i) Co₃O₄ QDs/CNNS generated photocarriers under

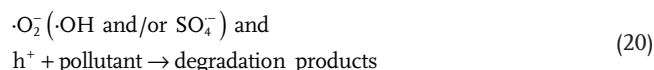
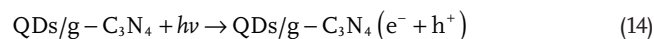
visible light irradiation. Subsequently, the photogenerated e^- transferred to CNN (the lower CB) were captured by O_2 to produce $\cdot O_2^-$ and activated PMS to produce $SO_4^{\cdot-}$, further producing $\cdot OH$; ii) The chemical reaction of Co_3O_4 QDs in the composite also activated PMS for the generation of $SO_4^{\cdot-}$. These free radicals with strong oxidation capacity could degrade organic pollutants into H_2O and CO_2 ; and iii) h^+ accumulated on the surface of Co_3O_4 QDs could directly degrade pollutants (Figure 16F). The author also testified that Co_3O_4 QDs/CNNS/PMS system had a universal applicability and an excellent degradation efficiency of multiple organic pollutant.

However, the traditional metal-containing photocatalyst is more easily to leach and may cause secondary pollution.^[129] Therefore, recent studies have also shown the possibility of metal-free QDs and g- C_3N_4 being used to activate PMS/PDS for the degradation of organic pollutants.^[63,129] Ming et al. constructed CQDs/polymer carbon nitride (PCN) via a hydrothermal method and removed bisphenol A (BPA) through the activation of PMS under the visible light irradiation.^[129] The heightened light properties of CQDs/g- C_3N_4 composites were attributed to the up-conversion effect. The shorter PL intensity indicated the easier separation of photocarriers due to the strengthened interface structure connection and the grab of photogenerated electrons by oxidants. Eventually, CQDs/PCN/PMS/vis system exhibited an optimal BPA degradation efficiency (95% removal within 30 min).

Generally, CN has become a van der Waals (VDWs) heterostructure with CQDs to construct a fast channel and decrease the energy consumption of charge transfer.^[120] However, the charge carriers of CN must overcome a large barrier to reach the CQDs as well, which cannot maximize the utilization of photogenerated electrons.^[185] Thus, lateral heterostructures (LHSs) are constructed between CQDs and CN to solve this limitation and gave a closer contact than the traditional CQDs/CN (CCN).^[149] Si et al. prepared a lateral CQDs/CN (LCCN) photocatalyst via a thermal polymerization method for TC degradation.^[120] The author used DFT calculations to attain the adsorption energies and the I(O–O) length between dissolved oxygen (DO) and the samples at different location. It was verified that the LHSs constructed a micro-regional electron delocalization for the better absorption and the easier activation of DO (Figure 17A–C). Besides, TC was adsorbed around LHSs on LCCN, causing the unpaired electrons of TC activated and transferred to CB of g- C_3N_4 . Plenty of $\cdot O_2^-$ as single active species were generated by the photoelectrons, the unpaired e^- of TC and the better absorption of DO (Figure 17D). The photocatalytic activity of LCCN increased 14-fold in the presence of the LHSs structure compared to CN. Moreover, in view of the importance of predicting the degradation pathways, the author obtained the Fukui index f^0 by using the Fukui function, which could basically represent the active site of the reactants. In general, the higher site the f^0 presented, the more vulnerable to free radical attack (Figure 17E). Thus, in this system, the mainly attacked atoms included C10, C15, C21, C22, O25, O32, O39 and N41 (Figure 17F). Combining with LC-MS/TOF, it was determined that the degradation process mainly includes four steps: hydroxylation, ring formation, demethylation and ring opening. The toxicity analysis showed that the toxicity of the intermediates had been greatly decreased. The above results indicate that

this system presented a novel perspective and promising prospect for metal-free photocatalyst with LHSs.

Finally, a series of studies on photocatalytic degradations of pollutants are summarized in Table 4, including synthesis methods, pollutants, experimental conditions, degradation efficiency, stability, and reusability. Noticeably, the photocatalytic degradation of pollutants requires more active substances with greater oxidation capacity. Z-scheme photocatalysts tend to produce more active substances and higher oxidation capacity. In some systems, the combination of photocatalysis and Fenton reaction or SR-AOPs also promotes more active substances with stronger oxidation capacity for an efficient and quicker degradation process.^[78,127,161] DFT calculation can be used not only to further analyze the reaction mechanism of photocatalyst, but also to predict and analyze the degradation paths and products in the practical applications. In summary, the mechanism is generally summarized as follows: under visible light, QDs/g- C_3N_4 photocatalysts produce e^- - h^+ pairs. Then, the photogenerated electrons produce free radicals with strong redox capacity by reducing O_2 , H_2O_2 and even PDS/PMS when the corresponding potential is satisfied. Both the free radicals and the photogenerated holes successfully oxidize pollutants into harmless products (CO_2 and H_2O) (Equations (14)–(20)).



5.2. Photocatalytic Disinfection

Microbial contaminations bring various infectious waterborne diseases to human health around the world, and cause millions of deaths each year.^[186,187] Common pathogenic microorganisms include *Escherichia coli*, *Salmonella* H9812, and *Staphylococcus aureus* (*S. aureus*). In the past, traditional disinfection methods, like adding oxidants (e.g., chlorine and its compounds), have many disadvantages.^[92,188] Thus, the safe and green antibacterial method (photocatalysis) has attracted much attention of scientists around the world.^[189] Considering the excellent photocatalytic ability, QDs/g- C_3N_4 composites has been attempted for photocatalytic disinfection with high performance.

Wang et al. fabricated vanadate QDs/g- C_3N_4 composites and proved their outstanding photocatalytic disinfection toward 0.75 mg mL⁻¹ *Salmonella* H9812 (96.4%).^[92] This study pointed out that the abundant ROS (e.g., $\cdot O_2^-$) and e^- were generated

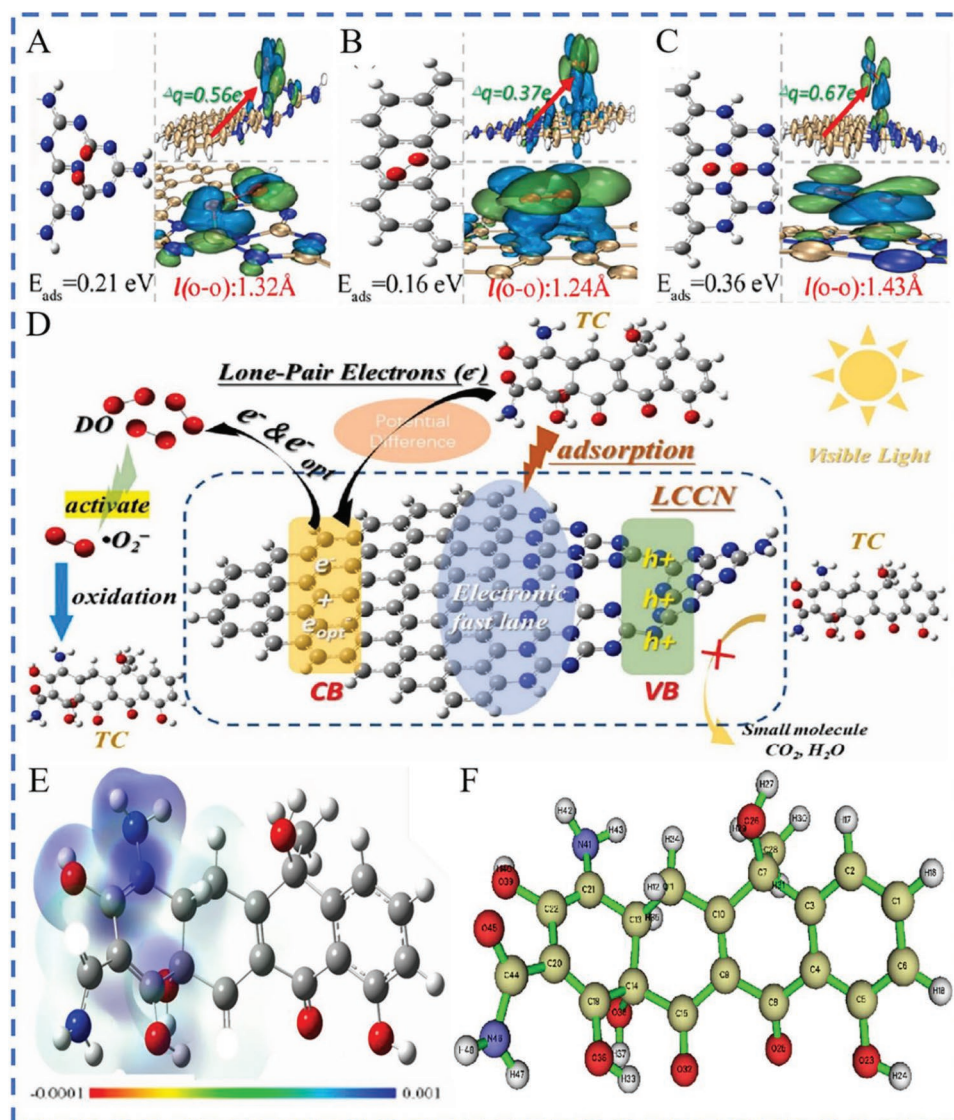


Figure 17. The adsorption energies and charge density difference (CDD) of O_2 molecules and the O—O bond length ($l(O-O)$) of isolated O_2 molecules at the different positions (CN (A), CQDs (B) and LHS (C)) of LCCN. The blue and green areas represent depletion and accumulation of electrons; D) schematic illustration for the possible mechanism of removing TC by LCCN in visible light; E) contour surfaces of Fukui function values of F° for radical attack; F) the number of each atom of TC. Adapted with permission.^[120] Copyright 2021, Elsevier.

from vanadate QDs/g- C_3N_4 in vitro, attributing to the effective visible light absorption and e^- - h^+ pairs separation. Ultimately, the bacterial cells membranes might be attacked by the ROS and e^- , and then the cell metabolism might be disrupted by bacterial contents. Such metal-containing QDs may be likely to produce secondary pollutions such as metal leaching, resulting in certain harm. For the sake of avoiding secondary pollution and toxicity caused by metal materials, Tang et al. successfully synthesized a metal-free photocatalyst CQDs/g- C_3N_4 for the inactivation of *S. aureus*.^[190] In this study, the cell membrane was destroyed due to the high level of ROS and the leakage of K^+ increased rapidly (Figure 18A,B). Moreover, the bacterial loaded in mice was decreased and the injury of CQDs/g- C_3N_4 was recovered compared with the treatment group by g- C_3N_4 . The toxicity analysis in vivo/vitro revealed that the toxicity of

CQDs/g- C_3N_4 was negligible, which could open up the way to use CQDs/g- C_3N_4 for the application of disinfection.

Due to the high electronegativity of S atoms, doping S in CQDs (S-CQDs) have better electron transfer effect, which can greatly enhance their photocatalytic activity. Thus, Wang et al. prepared low-toxic S-CQDs modified hollow porous tubular g- C_3N_4 photocatalyst (HTCN-C (x), where x represented the S-CQDs volume) by an ultrasonic-assisted method and investigated the photocatalysis disinfection activity of the composite.^[47] In the photocatalytic disinfection system, the rapid leakage of K^+ was detected as well, indicating the destroyed structure of *Escherichia coli*. The results showed that HTCN-C(2) exhibited the inactivation of $6.88 \log_{10} \text{ cfu mL}^{-1}$ of bacterial cells (about 99.99% destruction rate). S-CQDs not only acted an electronic medium to reduce the recombination of

Table 4. Summary of the QDs/g-C₃N₄ composites for degradation pollutant.

Composites	Synthetic method	Pollutant	Conditions		Catalytic efficiency [min]	Stability and reusability	Refs.
			Catalysts	Pollutant			
CdS QDs/g-C ₃ N ₄	In situ deposition method	Rhodamine B	100 mg	100 mL (10 mg mL ⁻¹)	88.2% (90 min)	Little decrease of the photocatalytic activity after four cycle evaluations; the same XRD patterns as that of the fresh photocatalyst after 4th cycling experiment	[66]
Bi ₃ TaO ₇ QDs/g-C ₃ N ₄ NSs	Ultrasonic assisted method	Ciprofloxacin, Cephalixin	50 mg	100 mL (10 mg mL ⁻¹)	91% (120 min) 77% (240 min)	The stable XRD patterns and FTIR spectrums after several runs of photocatalytic tests	[80]
Bi ₂ O ₃ QDs/g-C ₃ N ₄	Wet impregnation and manual grinding method	Tetracycline	50 mg	100 mL (10 mg mL ⁻¹)	83.1% (120 min)	The maintaining removal rate under visible light irradiation and the same phase and structure of catalysts the after six times running	[46]
ZnSe QDs-Ag/g-C ₃ N ₄	Self-assembly method	Ceftriaxone sodium	100 mg	100 mL (10 mg mL ⁻¹)	89.24% (90 min)	The similar XRD patterns and FTIR spectrums before and after ceftriaxone sodium degradation	[177]
CQDs/g-C ₃ N ₄	Thermal polymerization method	Diclofenac	10 mg	50 mL (10 mg mL ⁻¹)	100% (60 min)	The removal efficiency of DCF maintaining over 90% even in the fifth cycle	[178]
FeOOH QDs/g-C ₃ N ₄	Chemical deposition method	Methylene orange	80 mg	20 mL (50 mg mL ⁻¹)	100% (60 min)	The above 100% removal efficiency of MO in five cycles within 80 min; no detectable soluble iron ion concentrations in solution	[127]
Fe ₃ O ₄ QDs/Co-CN	Calcination deposition technology	Tetracycline	50 mg	100 mL (20 mg mL ⁻¹)	80.5% (90 min)	The hardly reduced photocatalytic activity of catalysts after recycling for four runs	[182]
FeOOH QDs/UPCN	In situ deposition method	Oxytetracycline	20 mg	50 mL (20 mg mL ⁻¹)	86.23% (120 min)	A nearly constant degradability of the OTC and the consistent XRD spectra and FT-IR spectra of catalysts after running 4 cycles of photo-Fenton degradation OTC	[161]
Co ₃ O ₄ QDs/CNNS+PMS	Chemical reaction and annealing	Tetracycline	10 mg	50 mL (50 mg mL ⁻¹)	99% (60 min)	No obvious decrease in the catalytic efficiency of catalysts in TC degradation and the similar TEM after five recycles	[111]
CQDs/PCN+PMS	Thermal polymerization strategy	Bisphenol A	50 mg	150 mL (20 mg mL ⁻¹)	95% (30 min)	A slight deactivation but more than 90% removal rate in the fourth run; no significant change in crystalline and chemical structure	[129]
Lateral CQDs/CN (LCCN)	Thermal polymerization strategy	Tetracycline	30 mg	50 mL (20 mg mL ⁻¹)	100% (60 min)	—	[149]

photocarriers, but also played a role of photosensitizer, which broadened the visible absorption range and transmitted energy to HTCNC. Noteworthy, the structure of HTCNC also endowed the composites with larger pore volume and higher specific surface area, shortening the mass transfer path and increasing the active sites (Figure 18C,D). Finally, the possible reaction mechanism was raised (Figure 18E). The electrons accumulated on the CB of HTCNC-C effectively reduced O₂ to ·O₂⁻, which react with H⁺ to form H₂O₂ for the ·OH. The photogenerated h⁺ retained on the VB of HTCNC-C. All these (·O₂⁻, ·OH and h⁺) might attend the photocatalytic disinfection of Escherichia coli. The removal rate of degrading TC reached 82.67% by this composite, showing a surprising variety of reactions produced

by HTCNC-C. DFT calculation has been applied to the research of QDs/g-C₃N₄ photocatalytic CO₂ reduction, pollutant degradation and other fields, and some achievements have been made in the reaction mechanism. However, it has not been used in disinfection research at present. In the future, it is hoped that the combination of DFT calculation can be used to gain enough insight to provide more effective assistance for practical application.

5.3. Cr⁶⁺ Reduction

Hexavalent chromium (Cr⁶⁺), as one of the main heavy metals, has been a research hotspot in environmental fields.^[191] In

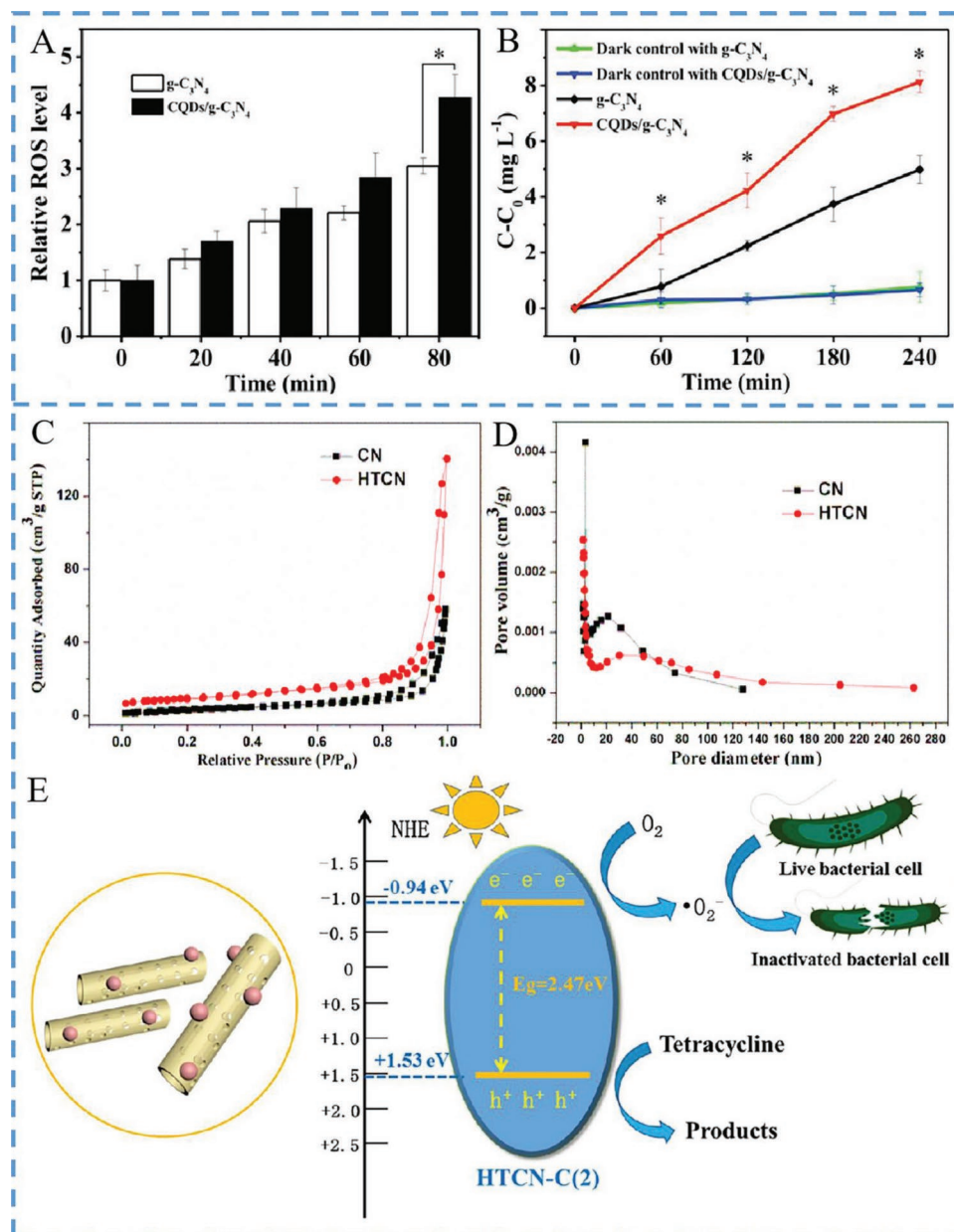


Figure 18. A) Intracellular ROS level (relative to initial fluorescence level at 0 min) of *S. aureus* treated by $g-C_3N_4$ or CQDs/ $g-C_3N_4$; B) leakage of intracellular K^+ of *S. aureus*. Adapted with permission.^[190] Copyright 2019, WILEY-VCH. C) N_2 adsorption–desorption isotherms of the prepared materials bulk $g-C_3N_4$ and HTCNC; D) the pore size distributions were determined from the desorption branch of the isotherm; E) possible photocatalytic mechanism scheme of HTCNC-C(2) composite for TC degradation and photocatalytic inactivation toward *Escherichia coli* under visible light irradiation. Adapted with permission.^[47] Copyright 2020, Elsevier.

common, Cr^{6+} accumulates in soil and organisms, which can adversely influence the ecosystem and cause harm to humans.^[192] The stronger reducibility of photogenerated electrons can sufficiently reduce Cr^{6+} to Cr^{3+} , thus a number of photocatalysts have been utilized for Cr^{6+} removal in wastewater. Of course, the outstanding photocatalytic QDs/ $g-C_3N_4$ composites also play a role of reducing Cr^{6+} .^[24,88]

Considering the excellent electrical and optical properties of black phosphorus (BP), Wang et al. introduced a promising metal-free BP QDs/tubular $g-C_3N_4$ (BPTCN) photocatalyst

and researched the Cr^{6+} reduction in wastewater with different pH.^[24] They found that the optimal pH value for photocatalytic reduction activity of composite was 4.65 (Figure 19B). The reason for this was that under acidic conditions Cr^{6+} presented mainly in the form of $Cr_2O_7^-$ or $HCrO_4^-$, which could be charge from Cr^{6+} to Cr^{3+} by abundant H^+ (Equation (21)); While under neutral or alkaline conditions, Cr^{6+} presented in the form of CrO_4^{2-} and could be transferred to $Cr(OH)_3$, which tended to cover the active sites of BPTCN, decreasing the photocatalytic activity (Equation (22)). Additionally,

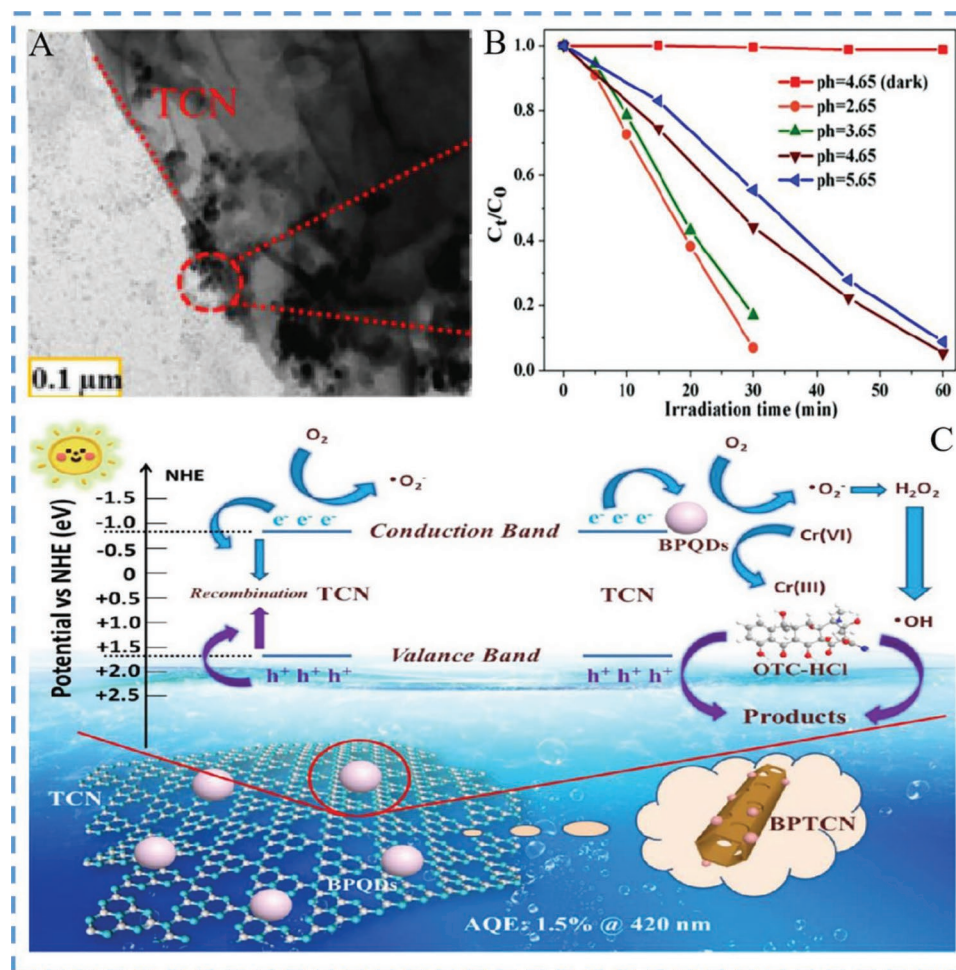
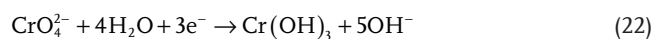
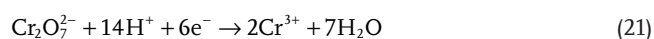


Figure 19. A) TEM images of BPTCN; B) effect of different pH values on Cr⁶⁺ reduction; C) possible photocatalytic mechanism scheme of the carrier separation process on the interface of BPTCN under visible light irradiation. Adapted with permission.^[24] Copyright 2020, Elsevier.

the light absorption ability of BPTCN was improved to a great extent. Meanwhile, the unique 0D/1D heterojunction (P-C bond) was obtained by a tight interaction between the uniformly distributed BP QDs and tubular g-C₃N₄ (TCN) (Figure 19A), which promoted electrons transfer for a highly photocatalytic performance. Ultimately, the mechanism of photocatalytic reduction of Cr⁶⁺ by BPTCN was shown in Figure 19C. First, BPTCN generated e⁻-h⁺ pairs under visible light. Then, the photogenerated electrons transferred from TCN to BP QDs (e⁻) as well as reduced Cr⁶⁺ to Cr³⁺ because of the more negative CB level of the photocatalyst than the redox potential of Cr⁶⁺/Cr³⁺ (0.57 V). In addition, above of H⁺, ·O₂⁻ and ·OH were produced to attack TC and the composite achieved efficient degradation effect. In this system, the composite could not only reduce Cr⁶⁺ but also degrade pollutants, demonstrating different reaction types with a certain application prospect.



5.4. NO Oxidation

Air pollution has been of great attention around the world. As one of the major air pollution, nitric oxide (NO) usually comes from vehicle exhaust and fuel combustion.^[193,194] Generally, NO has the potential to react with O₂ to provide the toxic NO₂/N₂O₄, leading to secondary pollution.^[169] Besides, NO is a major source of photochemical smog and acid rain, which severely affects the ecological environment. Recently, g-C₃N₄ coupled with QDs has been applied to remove NO. Zou et al. successfully prepared SnO₂ QDs/g-C₃N₄ composites to remove NO.^[117] The formation of heterojunction between SnO₂ QDs and g-C₃N₄ effectively prompted the separation of photogenerated e⁻-h⁺ pairs, which led to the production of ·O₂⁻ for the conversion of NO to NO₃⁻ as well as the inhibition of NO₂ (Figure 20A). Not only that, the photogenerated holes could directly transform NO to N₂O (1.03 eV), HNO₂ (0.99 eV) and HNO₃ (0.94 eV). Among all samples, the 10% SnO₂/g-C₃N₄ represented the best removal property (32%), which was 1.7-fold than that of g-C₃N₄. Although this photocatalyst played a certain role in NO oxidation, the oxidation efficiency was still not enough.

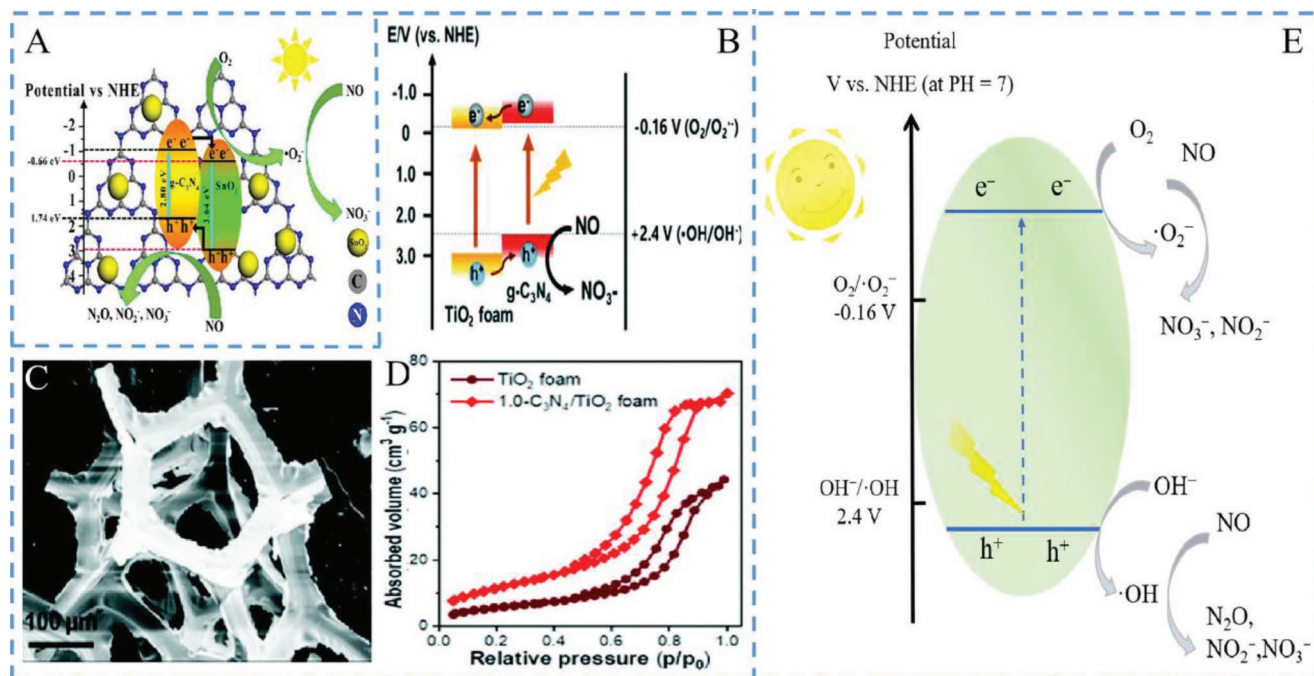


Figure 20. A) The illustration of photocatalysis mechanism on SnO₂/g-C₃N₄ for NO removal. Adapted with permission.^[17] Copyright 2019, Elsevier. B) The NO reaction mechanism catalyzed by 1.0-C₃N₄/TiO₂ foam; C) the SEM image of the 1.0-C₃N₄/TiO₂ foam; D) the nitrogen adsorption and desorption isotherm of the TiO₂ foam and the 1.0-C₃N₄/TiO₂ foam; E) the general mechanism of NO oxidation by QDs/g-C₃N₄ composites. Adapted with permission.^[7] Copyright 2021, Royal Society of Chemistry.

In the process of NO oxidation, the strong oxidizing ·OH may deeply oxidize NO and further restrain the formation of more toxic byproduct NO₂ to a great extent. Apart from that, it is also important to optimize the adsorption capacity of NO. In order to improve the removal of NO, Xiong et al. suggested a combination of g-C₃N₄ QDs with TiO₂ QDs using a pyrolysis process to construct a functional heterojunction foams filters, which displayed a higher photocatalytic activity for NO oxidation (65%).^[7] The author pointed out that a large amount of NO was absorbed and a high light utilization efficiency was achieved on account of the large specific surface area and continuous pores in unique foams (Figure 20C,D). Moreover, all the samples possessed very low NO₂ concentration (<5 ppb) profiles during the photocatalytic NO oxidation process, successfully avoiding the harm of byproduct. According to bandgap schematic, the reaction mechanism was further determined (Figure 20B). Under the light irradiation, both g-C₃N₄ QDs and TiO₂ QDs generated photogenerated e⁻-h⁺ pairs. The photogenerated electrons transferred to the CB of photocatalysts with negative potential than O₂/·O₂⁻ (-0.16 eV), leading to the impossibility of ·O₂⁻ production. The photogenerated holes were transferred to g-C₃N₄ QDs, which reacted with NO to NO⁺ or even directly oxidized OH⁻ to ·OH (Equations (23)–(24)). The intermediate products (NO⁺) would further be oxidized to NO₃⁻/NO₂⁻ by h⁺ and ·OH (Equations (25)–(27)), which exhibited a new oxidation pathway (NO → NO⁺ → NO₂⁻ or NO₃⁻).



In summary, the design of photocatalytic materials with stronger redox capacity is the critical key to avoid more toxic byproducts in the further. The mechanism of NO reduction by QDs/g-C₃N₄ photocatalysts generally summarized as shown in Figure 20E. QDs/g-C₃N₄ produce photogenerated e⁻-h⁺ pairs under visible light irradiation. The photogenerated electrons transferred to the CB of photocatalysts with negative potential than O₂/·O₂⁻ (-0.16 V), which produce ·O₂⁻ radicals. Moreover, the photogenerated holes transferred to the VB of photocatalysts with positive potential than OH⁻/·OH (+2.4 V), which can oxidize OH⁻ to ·OH. Ultimately, NO is mainly oxidized to NO₃⁻/NO₂⁻ by h⁺ and ROS (including ·O₂⁻, ·OH), or followed by other byproducts.

6. The Stability and Reusability of QDs/g-C₃N₄ Composites

The stability of photocatalyst is a key factor in determining their practical applications.^[195] For composites, the original structure may be destroyed due to the weak interactions between components.^[46,196] Additionally, some photocatalysts may suffer from photocorrosion.^[59,85] Therefore, according to the relevant literature, the stability of QDs/g-C₃N₄ composites

had been analyzed in most cases. As shown in Tables 2–4, X-ray diffraction (XRD), X-ray photoelectron spectroscopy (XPS) and Fourier transform infrared (FT-IR) techniques have been widely used to reflect the chemical stability of QDs/g-C₃N₄ composites. All the tested QDs/g-C₃N₄ composites exhibited no remarkable changes in crystal structures and chemical states before and after the reactions, which indicated their relative stability.^[49,65,90,151,152,155,159] Scanning electron microscopy (SEM), TEM, and HRTEM showed that the morphology of the tested composites before and after the reaction was well maintained.^[42,48,69,78,94,129] In some studies, the inductively coupled plasma (ICP) technique has also been used to detect the metal leaching during the reactions.^[44,127,182,197,198] The results displayed that these composites maintained a low leaching of metal species in solution. In particular, the release of metal was not even detected at all, indicating that QDs/g-C₃N₄ composites possessed good resistance to photocorrosion. Notably, the PbS@CdS@ZnS core@shell@shell QDs/g-C₃N₄ (PSZ QDs/g-C₃N₄) composites designed by Zhang et al. had near-infrared light absorption performance.^[44] No metal release was detected in the PSZ QDs/g-C₃N₄ composite solution, while the concentration of Pb and Cd in the PbS@CdS QDs solution increased with the increasing illumination time. The results were attributed to the metal leaching resistance of ZnS shell as well as the close contact between PSZ QDs and g-C₃N₄. As a result, QDs/g-C₃N₄ composites could be proved a long stability in the process of photocatalytic reaction.

The reusability of the photocatalysts is another factor that determines their practical applications. As shown in Tables 2–4, the photocatalytic performance of QDs/g-C₃N₄ composites remained close to that of the original materials after cycle experiments.^[45,53,85,144,154,156,178] Therefore, QDs/g-C₃N₄ composites can be reused in photocatalytic reactions, reducing the cost of the entire process. However, it should be of concern that the reuse of materials usually needs centrifugations or filtrations. In this case, the loss of QDs/g-C₃N₄ composites with the form of powders was inevitable, reducing the photocatalytic performance.^[56,91,92] Designing magnetic composites may be a way to solve the problem. Zhu et al. reported the Fe₃O₄ QDs/Co-CN composites with high reusability and easy separation from the reaction solution due to their satisfactory magnetic saturation value.^[182] In addition, the active sites of the photocatalysts might be covered by reactants or products, which would reduce the photocatalytic activity as well.^[91,117,172] For example, Zou et al. found that the photocatalytic activity of SnO₂ QDs/g-C₃N₄ was restored after being washed.^[117]

7. Conclusions and Prospects

The QDs/g-C₃N₄ composites not only successfully overcome the limitations of each component, but also combine the advantages of each component, leading to synergistic effects. In this system, the introduced QDs provide more active sites, superior light absorption performance, and tighter interfacial contacts to accelerate the separation as well as decrease the recombination of photocarriers. As a carrier, g-C₃N₄ maintains the small particle size of QDs by preventing them from aggregation. Furthermore, in addition to the common applications of

QDs/g-C₃N₄ (e.g., H₂ production, pollutant degradation), more comprehensive applications of QDs/g-C₃N₄ composites are introduced, including H₂O₂ generation, NO oxidation. Particularly, QDs/g-C₃N₄ photocatalysts are combined with DFT calculation and experiments to further elucidate the photocatalytic mechanism (adsorption energy, charge transfer, I(O–O) length, etc.) and degradation path (Fukui parameter *f*⁰, etc.). The analysis of the stability and reusability of the QDs/g-C₃N₄ composites also reflects the practical application possibility brought by the tighter interface contact. Although existing studies have shown that QDs/g-C₃N₄ composites have made considerable progress, the practical applications are still limited. To make the composites widely used in actual production, the following issues need to be considered in the future.

1. The introduced synthesis methods have certain corresponding advantages and disadvantages. However, their synthesis conditions need to be strictly controlled in order to ensure a high photocatalytic activity, so they are unsuitable for large-scale production in practical applications. To find a mild, efficient and low-cost synthesis method, the synthesis of large-scale QDs/g-C₃N₄ should be explored constantly in the future.
2. The synthesis conditions affect the structures and properties of QDs/g-C₃N₄ composites, which further control the photocatalytic performance.^[41,66,78,80] However, the effects of these synthesis conditions on the structure and properties of composites have not been adequately analyzed or investigated. Therefore, we look forward to uncover the relationship between the synthesis conditions, the structure and properties of the photocatalyst, and even the properties by advanced techniques and theoretical calculations, so as to design photocatalysts for practical applications.^[7,199]
3. In the energy fields, almost all QDs/g-C₃N₄ composites in the producing H₂/H₂O₂ inevitably need to add hole sacrifice agents to obtain higher photocatalytic efficiency. This not only increases the cost, but also wastes the oxidation capacity of photogenerated holes, which is not conducive to the practical applications of photocatalysts. Recently, studies have reported that some photocatalysts have been designed to achieve the simultaneous H₂ generation and organic conversion, which may also provide a new perspective for QDs/g-C₃N₄ composites.^[200]
4. In the field of environment, the application of QDs/g-C₃N₄ is relatively rare in removing heavy metals and Cr⁶⁺ is the only heavy metal studied in QDs/g-C₃N₄ composites. Therefore, it is necessary to extend the application of those composites. Moreover, it is an exciting but challenging task to construct multifunctional photocatalysts that can create simultaneous redox reactions. So far, H₂ production, CO₂ reduction and pollutants remediation have been completed in one system. Therefore, QDs/g-C₃N₄ is expected to produce more types of reactions in a system.
5. The coupling of QDs with g-C₃N₄ can enhance the interface contact as well as inhibit the photocorrosion as much as possible, but heavy metal leaching still needs to be considered. The research and development of metal-free efficient QDs/g-C₃N₄ have brought a surprise to the practical application and successfully avoided secondary pollution.^[100,119–121] Moreover,

researchers have designed shell QDs/g-C₃N₄ composites to solve this problem, but further exploration is needed.^[44]

6. Much of the work is based on laboratory-scale experiments with relatively simple pollutants. However, the influencing factors are more complex in the actual environment, including pH, temperature and other interfering substances, which may affect the photocatalytic performance of composites. Only a few studies of QDs/g-C₃N₄ composites have considered these issues.^[63,101] In the future, QDs/g-C₃N₄ composite should be used in the real environment for correlation experiments to improve the possibility of practical application.
7. Although QDs/g-C₃N₄ have good stability, they are mostly in powder form for laboratory research, which pose a challenge to large-scale processes involving the recovery efficiency. For example, designing composites with high magnetic properties, which can be easily separated from the reaction solution.^[182] Notably, some studies have been reported membrane photocatalysts that not only maintain similar photocatalytic efficiency as powder, but also retain activity and structural integrity after multiple cycle experiments.^[201] This also provides an idea for the film formation of QDs/g-C₃N₄ composites, which can be considered in the future.
8. Although QDs/g-C₃N₄ photocatalysts have been used to combine experiments with DFT calculation to further elucidate the photocatalytic mechanism and degradation path, the explored fields are relatively limited. Under the guidance of DFT calculation, QDs/g-C₃N₄ composites are expected to bring better photocatalytic performance and wider application ranges. Additionally, the guidance of DFT calculation is not comprehensive enough. For example, reactants or products tend to cover the active sites, which can reduce photocatalytic performance.^[91,117,172] If the DFT calculation can be applied to determine active sites in advance, it will certainly open a new door for the future of composite materials.
9. QDs have brought excellent photocatalytic performances to g-C₃N₄ both as a cocatalyst and as a semiconductor. The cocatalysts mainly speed up charge transfer and separation, and have a wide range of application in the field of energy production. Transition metal carbides, sulfides, and phosphates have successfully replaced the traditional cocatalysts (noble metals), and better cocatalysts are expected to be explored in the future.^[42,43,69,95–97] Furthermore, the exploration of S-scheme heterojunction QDs/g-C₃N₄ composites is still in the initial stage, which is worthy of attention.

Acknowledgements

This study was financially supported by the Program for the National Natural Science Foundation of China (51909084, 51909085, 52170161), the Natural Science Foundation of Hunan Province, China (2020JJ5069, 2020JJ3009), the Fundamental Research Funds for the Central Universities (531118010247), and the Hunan Researcher Award Program (2020RC3025).

Conflict of Interest

The authors declare no conflict of interest.

Keywords

energy, environment, graphitic carbon nitride, photocatalysis, quantum dots

Received: September 26, 2022

Revised: December 8, 2022

Published online:

- [1] B. Shao, Z. Liu, H. Zhong, G. Zeng, G. Liu, M. Yu, Y. Liu, X. Yang, Z. Li, Z. Fang, J. Zhang, C. Zhao, *Microbiol. Res.* **2017**, *200*, 33.
- [2] E. Kabir, P. Kumar, S. Kumar, A. A. Adelodun, K. Kim, *Renewable Sustainable Energy Rev.* **2018**, *82*, 894.
- [3] G. Wang, D. Huang, M. Cheng, S. Chen, G. Zhang, L. Lei, Y. Chen, L. Du, R. Li, Y. Liu, *Coord. Chem. Rev.* **2022**, *460*, 214467.
- [4] P. Zhang, P. Zhou, J. Peng, Y. Liu, H. Zhang, C. He, Z. Xiong, W. Liu, B. Lai, *Water Res.* **2022**, *219*, 118626.
- [5] F. Chen, Q. Yang, D. Wang, F. Yao, Y. Ma, X. Li, J. Wang, L. Jiang, L. Wang, H. Yu, *Chem. Eng. J.* **2018**, *354*, 983.
- [6] L. Wang, J. Zhao, H. Liu, J. Huang, *J. Taiwan Inst. Chem. Eng.* **2018**, *93*, 590.
- [7] Y. Liu, C. Tang, M. Cheng, M. Chen, S. Chen, L. Lei, Y. Chen, H. Yi, Y. Fu, L. Li, *ACS Catal.* **2021**, *11*, 13374.
- [8] Q. Shi, S. Deng, Y. Zheng, Y. Du, L. Li, S. Yang, G. Zhang, L. Du, G. Wang, M. Cheng, Y. Liu, *Environ. Res.* **2022**, *212*, 113340.
- [9] H. Liu, M. Cheng, Y. Liu, G. Zhang, L. Li, L. Du, B. Li, S. Xiao, G. Wang, X. Yang, *Coord. Chem. Rev.* **2022**, *458*, 214428.
- [10] A. Fujishima, K. Honda, *Nature* **1972**, *238*, 37.
- [11] Y. Huijun, *J. Mater. Chem. A* **2014**, *2*, 3344.
- [12] K. Nakata, A. Fujishima, *J. Photochem. Photobiol., C* **2012**, *13*, 169.
- [13] A. Sudhaik, P. Raizada, P. Shandilya, D. Jeong, J. Lim, P. Singh, *J. Ind. Eng. Chem.* **2018**, *67*, 28.
- [14] C. Zhang, Y. Li, D. Shuai, Y. Shen, W. Xiong, L. Wang, *Chemosphere* **2019**, *214*, 462.
- [15] L. Jiang, X. Yuan, Y. Pan, J. Liang, G. Zeng, Z. Wu, H. Wang, *Appl. Catal., B* **2017**, *217*, 388.
- [16] H. Wang, Y. Yang, X. Yuan, W. Liang Teo, Y. Wu, L. Tang, Y. Zhao, *Mater. Today* **2022**, *53*, 106.
- [17] K. He, R. Shen, L. Hao, Y. Li, P. Zhang, J. Jiang, L. Xin, *Acta Phys. Chim. Sin.* **2022**, *38*, 2201021.
- [18] X. Wang, K. Maeda, A. Thomas, K. Takanabe, G. Xin, J. M. Carlsson, K. Domen, M. Antonietti, *Nat. Mater.* **2009**, *8*, 76.
- [19] Y. Gong, M. Li, H. Li, Y. Wang, *Green Chem.* **2015**, *17*, 715.
- [20] M. Xiao, B. Luo, S. Wang, L. Wang, *J. Energy Chem.* **2018**, *27*, 1111.
- [21] D. M. Teter, R. J. Hemley, *Science* **1996**, *271*, 53.
- [22] L. Biswal, S. Nayak, K. Parida, *Catal. Sci. Technol.* **2021**, *11*, 1222.
- [23] Y. Zheng, J. Liu, J. Liang, M. Jaroniec, S. Z. Qiao, *Energy Environ. Sci.* **2012**, *5*, 6717.
- [24] W. Wang, Q. Niu, G. Zeng, C. Zhang, D. Huang, B. Shao, C. Zhou, Y. Yang, Y. Liu, H. Guo, W. Xiong, L. Lei, S. Liu, H. Yi, S. Chen, X. Tang, *Appl. Catal., B* **2020**, *273*, 119051.
- [25] L. H. Rongchen Shen, Q. Chen, Q. Zheng, P. Zhang, X. Li, *Acta Phys. Chim. Sin.* **2022**, *38*, 2110014.
- [26] D. Wang, J. Chen, X. Gao, Y. Ao, P. Wang, *Chem. Eng. J.* **2022**, *431*, 134105.
- [27] M. Majdoub, Z. Anfar, A. Amedlous, *ACS Nano* **2020**, *14*, 12390.
- [28] D. Huang, Z. Li, G. Zeng, C. Zhou, W. Xue, X. Gong, X. Yan, S. Chen, W. Wang, M. Cheng, *Appl. Catal., B* **2019**, *240*, 153.
- [29] Y. Xiao, G. Tian, W. Li, Y. Xie, B. Jiang, C. Tian, D. Zhao, H. Fu, *J. Am. Chem. Soc.* **2019**, *141*, 2508.
- [30] X. Liu, R. Ma, L. Zhuang, B. Hu, J. Chen, X. Liu, X. Wang, *Crit. Rev. Environ. Sci. Technol.* **2021**, *51*, 751.

- [31] X. Zhao, Y. Zhang, X. Zhao, X. Wang, Y. Zhao, H. Tan, H. Zhu, W. Ho, H. Sun, Y. Li, *ACS Appl. Mater. Interfaces* **2019**, *11*, 27934.
- [32] Q. Hao, G. Jia, W. Wei, A. Vinu, Y. Wang, H. Arandiyani, B. Ni, *Nano Res.* **2020**, *13*, 18.
- [33] B. Lin, Z. Chen, P. Song, H. Liu, L. Kang, J. Di, X. Luo, L. Chen, C. Xue, B. Ma, G. Yang, J. Tang, J. Zhou, Z. Liu, F. Liu, *Small* **2020**, *16*, 2003302.
- [34] J. Fu, J. Yu, C. Jiang, B. Cheng, *Adv. Energy Mater.* **2018**, *8*, 1701503.
- [35] Z. Fan, X. Guo, Z. Jin, X. Li, Y. Li, *Langmuir* **2022**, *38*, 3244.
- [36] X. Zhang, X. Yuan, L. Jiang, J. Zhang, H. Yu, H. Wang, G. Zeng, *Chem. Eng. J.* **2020**, *390*, 124475.
- [37] Y. Liu, Z. Liu, D. Huang, M. Cheng, G. Zeng, C. Lai, C. Zhang, C. Zhou, W. Wang, D. Jiang, H. Wang, B. Shao, *Coord. Chem. Rev.* **2019**, *388*, 63.
- [38] W. C. W. Chan, S. Nie, *Science* **1998**, *281*, 2016.
- [39] Y. E. Panfil, M. Oded, U. Banin, *Angew. Chem., Int. Ed.* **2018**, *57*, 4274.
- [40] A. A. Chistyakov, M. A. Zvaigzne, V. R. Nikitenko, A. R. Tameev, I. L. Martynov, O. Prezhdo, *J. Phys. Chem. Lett.* **2017**, *8*, 4129.
- [41] Y. Li, L. Ding, Y. Guo, Z. Liang, H. Cui, J. Tian, *ACS Appl. Mater. Interfaces* **2019**, *11*, 41440.
- [42] Z. Lu, C. Li, J. Han, L. Wang, S. Wang, L. Ni, Y. Wang, *Appl. Catal., B* **2018**, *237*, 919.
- [43] Z. Liang, B. Sun, X. Xu, H. Cui, J. Tian, *Nanoscale* **2019**, *11*, 12266.
- [44] Q. Zhang, F. Yang, S. Zhou, N. Bao, Z. Xu, M. Chaker, D. Ma, *Appl. Catal., B* **2020**, *270*, 118879.
- [45] F. Raziq, A. Hayat, M. Humayun, S. K. Baburao Mane, M. B. Faheem, A. Ali, Y. Zhao, S. Han, C. Cai, W. Li, D. Qi, J. Yi, X. Yu, M. B. H. Breese, F. Hassan, F. Ali, A. Mavlonov, K. Dhanabalan, X. Xiang, X. Zu, S. Li, L. Qiao, *Appl. Catal., B* **2020**, *270*, 118867.
- [46] Y. Liang, W. Xu, J. Fang, Z. Liu, D. Chen, T. Pan, Y. Yu, Z. Fang, *Appl. Catal., B* **2021**, *295*, 120279.
- [47] W. Wang, Z. Zeng, G. Zeng, C. Zhang, R. Xiao, C. Zhou, W. Xiong, Y. Yang, L. Lei, Y. Liu, D. Huang, M. Cheng, Y. Yang, Y. Fu, H. Luo, Y. Zhou, *Chem. Eng. J.* **2019**, *378*, 122132.
- [48] H. Qin, R. Guo, X. Liu, X. Shi, Z. Wang, J. Tang, W. Pan, *Colloids Surf., A* **2020**, *600*, 124912.
- [49] L. Ge, F. Zuo, J. Liu, Q. Ma, C. Wang, D. Sun, L. Bartels, P. Feng, *J. Phys. Chem. C* **2012**, *116*, 13708.
- [50] Y. Jiao, Q. Huang, J. Wang, Z. He, Z. Li, *Appl. Catal., B* **2019**, *247*, 124.
- [51] L. K. Putri, B. Ng, W. Ong, H. W. Lee, W. S. Chang, A. R. Mohamed, S. Chai, *Appl. Catal., B* **2020**, *265*, 118592.
- [52] K. Qi, W. Lv, I. Khan, S. Liu, *Chin. J. Catal.* **2020**, *41*, 114.
- [53] Z. Sun, W. Fang, L. Zhao, H. Chen, X. He, W. Li, P. Tian, Z. Huang, *Environ. Int.* **2019**, *130*, 104898.
- [54] X. Chen, W. Zhang, L. Zhang, L. Feng, C. Zhang, J. Jiang, T. Yan, H. Wang, *J. Mater. Chem. A* **2020**, *8*, 18816.
- [55] Y. Zhao, Y. Wang, H. Shi, E. Liu, J. Fan, X. Hu, *Mater. Lett.* **2018**, *231*, 150.
- [56] Y. Zhao, Y. Wang, X. Liang, H. Shi, C. Wang, J. Fan, X. Hu, E. Liu, *Appl. Catal., B* **2019**, *247*, 57.
- [57] Y. Chen, X. Bai, *Catalysts* **2020**, *10*, 142.
- [58] X. Hu, R. Guo, L. Hong, X. Ji, W. Pan, *ChemistrySelect* **2021**, *6*, 10854.
- [59] L. Yao, D. Wei, Y. Ni, D. Yan, C. Hu, *Nano Energy* **2016**, *26*, 248.
- [60] R. Guo, X. Liu, H. Qin, Z. Wang, X. Shi, W. Pan, Z. Fu, J. Tang, P. Jia, Y. Miao, J. Gu, *Appl. Surf. Sci.* **2020**, *500*, 144059.
- [61] G. Koyyada, N. Siva Kumar, E. H. Al-Ghurabi, M. Asif, K. Mallikarjuna, *Environ. Sci. Pollut. Res.* **2021**, *28*, 31585.
- [62] Q. Liu, T. Chen, Y. Guo, Z. Zhang, X. Fang, *Appl. Catal., B* **2016**, *193*, 248.
- [63] H. Chen, X. Zhang, L. Jiang, X. Yuan, J. Liang, J. Zhang, H. Yu, W. Chu, Z. Wu, H. Li, Y. Li, *Sep. Purif. Technol.* **2021**, *272*, 118947.
- [64] J. Guo, J. Liang, X. Yuan, L. Jiang, G. Zeng, H. Yu, J. Zhang, *Chem. Eng. J.* **2018**, *352*, 782.
- [65] Y. Liu, H. Zhang, J. Ke, J. Zhang, W. Tian, X. Xu, X. Duan, H. Sun, M. O. Tade, S. Wang, *Appl. Catal., B* **2018**, *228*, 64.
- [66] Q. Fan, Y. Huang, C. Zhang, J. Liu, L. Piao, Y. Yu, S. Zuo, B. Li, *Catal. Today* **2016**, *264*, 250.
- [67] Y. Zou, J. W. Shi, D. Ma, Z. Fan, L. Cheng, D. Sun, Z. Wang, C. Niu, *ChemSusChem* **2018**, *11*, 1187.
- [68] T. V. M. Sreekanth, P. C. Nagajothi, G. R. Dillip, Y. R. Lee, *J. Phys. Chem. C* **2017**, *121*, 25229.
- [69] Y. Zeng, Y. Xia, W. Song, S. Luo, *J. Mater. Chem. A* **2019**, *7*, 25908.
- [70] M. Li, C. Chen, L. Xu, Y. Jia, Y. Liu, X. Liu, *J. Energy Chem.* **2021**, *52*, 51.
- [71] J. Liu, H. Xu, Y. Xu, Y. Song, J. Lian, Y. Zhao, L. Wang, L. Huang, H. Ji, H. Li, *Appl. Catal., B* **2017**, *207*, 429.
- [72] T. Xu, D. Wang, L. Dong, H. Shen, W. Lu, W. Chen, *Appl. Catal., B* **2019**, *244*, 96.
- [73] T. Chen, W. Quan, L. Yu, Y. Hong, C. Song, M. Fan, L. Xiao, W. Gu, W. Shi, *J. Alloys Compd.* **2016**, *686*, 628.
- [74] D. Yang, H. Zou, Y. Wu, J. Shi, S. Zhang, X. Wang, P. Han, Z. Tong, Z. Jiang, *Ind. Eng. Chem. Res.* **2017**, *56*, 6247.
- [75] H. Ying, Z. Huang, G. Dong, Y. Zhang, *J. Photochem. Photobiol., A* **2021**, *415*, 113305.
- [76] S. Wang, F. Wang, Z. Su, X. Wang, Y. Han, L. Zhang, J. Xiang, W. Du, N. Tang, *Catalysts* **2019**, *9*, 439.
- [77] M. Xiong, Y. Tao, Z. Zhao, Q. Zhu, X. Jin, S. Zhang, M. Chen, G. Li, *Environ. Sci.: Nano* **2021**, *8*, 1571.
- [78] H. Zhang, W. Tian, L. Zhou, H. Sun, M. Tade, S. Wang, *Appl. Catal., B* **2018**, *223*, 2.
- [79] X. Li, H. Zhang, Y. Liu, X. Duan, X. Xu, S. Liu, H. Sun, S. Wang, *Chem. Eng. J.* **2020**, *390*, 124634.
- [80] K. Wang, G. Zhang, J. Li, Y. Li, X. Wu, *ACS Appl. Mater. Interfaces* **2017**, *9*, 43704.
- [81] J. M. Feckl, H. K. Dunn, P. M. Zehetmaier, A. Müller, S. R. Pendlebury, P. Zeller, K. Fominykh, I. Kondofersky, M. Döblinger, J. R. Durrant, C. Scheu, L. Peter, D. Fattakhova-Rohlfing, T. Bein, *Adv. Mater. Interfaces* **2015**, *2*, 1500358.
- [82] B. Sun, J. Dong, L. Cui, T. Feng, J. Zhu, X. Liu, S. Ai, *Biosens. Bioelectron.* **2019**, *124*, 1.
- [83] H. Wang, X. Li, X. Zhao, C. Li, X. Song, P. Zhang, P. Huo, X. Li, *Chin. J. Catal.* **2022**, *43*, 178.
- [84] X. Li, J. Yu, M. Jaroniec, X. Chen, *Chem. Rev.* **2019**, *119*, 3962.
- [85] Q. Liang, C. Zhang, S. Xu, M. Zhou, Y. Zhou, Z. Li, *J. Colloid Interface Sci.* **2020**, *577*, 1.
- [86] R. Molinari, M. Borgese, E. Drioli, L. Palmisano, M. Schiavello, *Catal. Today* **2002**, *75*, 77.
- [87] M. D. Hernández-Alonso, F. Fresno, S. Suárez, J. M. Coronado, *Energy Environ. Sci.* **2009**, *2*, 1231.
- [88] J. Wang, W. Lin, H. Hu, C. Liu, Q. Cai, S. Zhou, Y. Kong, *New J. Chem.* **2021**, *45*, 3067.
- [89] B. Babu, M. Cho, C. Byon, J. Shim, *Mater. Lett.* **2018**, *212*, 327.
- [90] F. Bi, Y. Su, Y. Zhang, M. Chen, J. A. Darr, X. Weng, Z. Wu, *Appl. Catal., B* **2022**, *306*, 121109.
- [91] S. Sun, X. Yuan, Y. Wang, W. Zhang, Y. Li, Z. Zhang, J. Su, J. Zhang, S. Hu, *Appl. Surf. Sci.* **2022**, *576*, 151901.
- [92] R. Wang, X. Kong, W. Zhang, W. Zhu, L. Huang, J. Wang, X. Zhang, X. Liu, N. Hu, Y. Suo, J. Wang, *Appl. Catal., B* **2018**, *225*, 228.
- [93] J. Wang, C. Liu, S. Yang, X. Lin, W. Shi, *J. Phys. Chem. Solids* **2020**, *136*, 109164.
- [94] S. Gong, X. Teng, Y. Niu, X. Liu, M. Xu, C. Xu, L. Ji, Z. Chen, *Appl. Catal., B* **2021**, *298*, 120521.
- [95] Z. Liang, Y. Guo, Y. Xue, H. Cui, J. Tian, *Mater. Chem. Front.* **2019**, *3*, 2032.
- [96] L. Shi, Z. He, S. Liu, *Appl. Surf. Sci.* **2018**, *457*, 30.

- [97] B. Chang, Y. Guo, H. Liu, L. Li, B. Yang, *J. Mater. Chem. A* **2022**, 10, 3134.
- [98] G. Di, Z. Zhu, Q. Dai, H. Zhang, X. Shen, Y. Qiu, Y. Huang, J. Yu, D. Yin, S. Küppers, *Chem. Eng. J.* **2020**, 379, 122296.
- [99] Y. Nie, F. Yu, L. Wang, Q. Xing, X. Liu, Y. Pei, J. Zou, W. Dai, Y. Li, S. L. Suib, *Appl. Catal., B* **2018**, 227, 312.
- [100] C. Feng, Y. Deng, L. Tang, G. Zeng, J. Wang, J. Yu, Y. Liu, B. Peng, H. Feng, J. Wang, *Appl. Catal., B* **2018**, 239, 525.
- [101] Z. Hu, X. Xie, S. Li, M. Song, G. Liang, J. Zhao, Z. Wang, *Chem. Eng. J.* **2021**, 404, 126541.
- [102] Y. Yang, Z. T. Zeng, G. M. Zeng, D. L. Huang, R. Xiao, C. Zhang, C. Y. Zhou, W. P. Xiong, W. J. Wang, M. Cheng, W. J. Xue, H. Guo, X. Tang, D. H. He, *Appl. Catal., B* **2019**, 258, 11.
- [103] B. Zhou, B. Yang, M. Waqas, K. Xiao, C. Zhu, L. Wu, *RSC Adv.* **2020**, 10, 19169.
- [104] F. Xue, M. Liu, C. Cheng, J. Deng, J. Shi, *ChemCatChem* **2018**, 10, 5441.
- [105] Y. Wang, H. Ma, J. Liu, Y. Yu, S. Zuo, X. Zhang, S. Zheng, *J. Mater. Sci.* **2022**, 57, 274.
- [106] D. Liu, C. Li, T. Ni, R. Gao, J. Ge, F. Zhang, W. Wu, J. Li, Q. Zhao, *Appl. Surf. Sci.* **2021**, 555, 149677.
- [107] M. Liu, H. Xia, W. Yang, X. Liu, J. Xiang, X. Wang, L. Hu, F. Lu, *Appl. Catal., B* **2022**, 301, 120765.
- [108] R. Shen, D. Ren, Y. Ding, Y. Guan, Y. H. Ng, P. Zhang, X. Li, *Sci. China Mater.* **2020**, 63, 2153.
- [109] Y. Zhong, Y. Shao, F. Ma, Y. Wu, B. Huang, X. Hao, *Nano Energy* **2017**, 31, 84.
- [110] M. Ye, Z. Zhao, Z. Hu, L. Liu, H. Ji, Z. Shen, T. Ma, *Angew. Chem., Int. Ed.* **2016**, 56, 8407.
- [111] H. Gao, H. Yang, J. Xu, S. Zhang, J. Li, *Small* **2018**, 14, 1801353.
- [112] Q. Liang, C. Zhang, S. Xu, M. Zhou, Z. Li, *Int. J. Hydrogen Energy* **2019**, 44, 29964.
- [113] Y. Zhong, W. Chen, S. Yu, Z. Xie, S. Wei, Y. Zhou, *ACS Omega* **2018**, 3, 17762.
- [114] S. Yu, S. Zhang, K. Li, Q. Yang, M. Wang, D. Cai, T. Tan, B. Chen, *ACS Sustainable Chem. Eng.* **2020**, 8, 15980.
- [115] M. Ou, W. Tu, S. Yin, W. Xing, S. Wu, H. Wang, S. Wan, Q. Zhong, R. Xu, *Angew. Chem., Int. Ed.* **2018**, 57, 13570.
- [116] J. Pan, Z. Dong, Z. Jiang, C. Zhao, B. Wang, W. Zhao, J. Wang, C. Song, Y. Zheng, C. Li, *Sol. RRL* **2019**, 3, 1900337.
- [117] Y. Zou, Y. Xie, S. Yu, L. Chen, W. Cui, F. Dong, Y. Zhou, *Appl. Surf. Sci.* **2019**, 496, 143630.
- [118] M. U. Yousaf, E. Pervaiz, S. Minallah, M. J. Afzal, L. Honghong, M. Yang, *Results Phys.* **2019**, 14, 102455.
- [119] M. Wang, H. Yu, P. Wang, Z. Chi, Z. Zhang, B. Dong, H. Dong, K. Yu, H. Yu, *Sep. Purif. Technol.* **2021**, 274, 118692.
- [120] Q. Si, W. Guo, H. Wang, B. Liu, S. Zheng, Q. Zhao, H. Luo, N. Ren, T. Yu, *Appl. Catal., B* **2021**, 299, 120694.
- [121] M. Zhang, C. Lai, B. Li, F. Xu, D. Huang, S. Liu, L. Qin, Y. Fu, X. Liu, H. Yi, Y. Zhang, J. He, L. Chen, *Chem. Eng. J.* **2020**, 396, 125343.
- [122] M. Aleksandrak, M. Baca, M. Pacia, K. Wleniska, B. Zielinska, R. J. Kalenczuk, E. Mijowska, *Nanotechnology* **2021**, 32, 355703.
- [123] F. Chang, W. Yan, W. Cheng, F. Wu, B. Deng, X. Hu, *Mater. Sci. Semicond. Process.* **2018**, 87, 1.
- [124] O. M. Bankole, T. D. Olorunsola, A. S. Ogunlaja, *J. Photochem. Photobiol., A* **2021**, 405, 112934.
- [125] M. F. R. Samsudin, H. Ullah, A. A. Tahir, X. Li, Y. H. Ng, S. Sufian, *J. Colloid Interface Sci.* **2021**, 586, 785.
- [126] F. Ding, P. Chen, F. Liu, L. Chen, J. Guo, S. Shen, Q. Zhang, L. Meng, C. Au, S. Yin, *Appl. Surf. Sci.* **2019**, 490, 102.
- [127] X. Qian, Y. Wu, M. Kan, M. Fang, D. Yue, J. Zeng, Y. Zhao, *Appl. Catal., B* **2018**, 237, 513.
- [128] V. Balakumar, M. Ramalingam, K. Sekar, C. Chuaicham, K. Sasaki, *Chem. Eng. J.* **2021**, 426, 131739.
- [129] H. Ming, D. Wei, Y. Yang, B. Chen, C. Yang, J. Zhang, Y. Hou, *Chem. Eng. J.* **2021**, 424, 130296.
- [130] L. Huang, J. Liu, P. Li, Y. Li, C. Wang, S. Shu, Y. Song, *J. Alloys Compd.* **2022**, 895, 162637.
- [131] Z. Liang, R. Shen, Y. H. Ng, P. Zhang, Q. Xiang, X. Li, *J. Mater. Sci. Technol.* **2020**, 56, 89.
- [132] R. Shen, J. Xie, Q. Xiang, X. Chen, J. Jiang, X. Li, *Chin. J. Catal.* **2019**, 40, 240.
- [133] S. Raheman Ar, H. M. Wilson, B. M. Momin, U. S. Annapure, N. Jha, *Renewable Energy* **2020**, 158, 431.
- [134] Y. Zou, J. Shi, L. Sun, D. Ma, S. Mao, Y. Lv, Y. Cheng, *Chem. Eng. J.* **2019**, 378, 122192.
- [135] J. Low, J. Yu, M. Jaroniec, S. Wageh, A. A. Al-Ghamdi, *Adv. Mater.* **2017**, 29, 1601694.
- [136] A. J. Bard, *J. Photochem.* **1979**, 10, 59.
- [137] S. Wageh, A. A. Al-Ghamdi, R. Jafer, X. Li, P. Zhang, *Chin. J. Catal.* **2021**, 42, 667.
- [138] J. Fu, Q. Xu, J. Low, C. Jiang, J. Yu, *Appl. Catal., B* **2019**, 243, 556.
- [139] J. Bai, R. Shen, Z. Jiang, P. Zhang, Y. Li, X. Li, *Chin. J. Catal.* **2022**, 43, 359.
- [140] S. Li, M. Cai, Y. Liu, J. Zhang, C. Wang, S. Zang, Y. Li, P. Zhang, X. Li, *Inorg. Chem. Front.* **2022**, 9, 2479.
- [141] T. Hisatomi, J. Kubota, K. Domen, *Chem. Soc. Rev.* **2014**, 43, 7520.
- [142] Q. C. Zhimin Jiang, Q. Zheng, R. Shen, P. Zhang, X. Li, *Acta Phys. Chim. Sin.* **2021**, 37, 2010059.
- [143] J. Shi, Y. Zou, L. Cheng, D. Ma, D. Sun, S. Mao, L. Sun, C. He, Z. Wang, *Chem. Eng. J.* **2019**, 378, 122161.
- [144] Y. Yang, B. Mao, G. Gong, D. Li, Y. Liu, W. Cao, L. Xing, J. Zeng, W. Shi, S. Yuan, *Int. J. Hydrogen Energy* **2019**, 44, 15882.
- [145] L. Cheng, S. Xie, Y. Zou, D. Ma, D. Sun, Z. Li, Z. Wang, J. Shi, *Int. J. Hydrogen Energy* **2019**, 44, 4133.
- [146] A. Kudo, Y. Miseki, *Chem. Soc. Rev.* **2009**, 38, 253.
- [147] Z. You, X. Yue, D. Zhang, J. Fan, Q. Xiang, *J. Colloid Interface Sci.* **2022**, 607, 662.
- [148] X. Jin, X. Fan, J. Tian, R. Cheng, M. Li, L. Zhang, *RSC Adv.* **2016**, 6, 52611.
- [149] Y. Wang, X. Liu, J. Liu, B. Han, X. Hu, F. Yang, Z. Xu, Y. Li, S. Jia, Z. Li, Y. Zhao, *Angew. Chem., Int. Ed.* **2018**, 57, 5765.
- [150] G. Cai, J. Wang, X. Wu, Y. Zhan, S. Liang, *Appl. Surf. Sci.* **2018**, 459, 224.
- [151] S. V. P. Vattikuti, P. A. K. Reddy, J. Shim, C. Byon, *ACS Omega* **2018**, 3, 7587.
- [152] K. C. Devarayapalli, K. Lee, N. D. Nam, S. V. P. Vattikuti, J. Shim, *Ceram. Int.* **2020**, 46, 28467.
- [153] J. Pan, M. You, C. Chi, Z. Dong, B. Wang, M. Zhu, W. Zhao, C. Song, Y. Zheng, C. Li, *Int. J. Hydrogen Energy* **2018**, 43, 6586.
- [154] T. Zhao, Z. Xing, Z. Xiu, Z. Li, S. Yang, Q. Zhu, W. Zhou, *Int. J. Hydrogen Energy* **2019**, 44, 1586.
- [155] J. Qin, H. Zeng, *Appl. Catal., B* **2017**, 209, 161.
- [156] Y. Zhang, W. Zhang, *Carbon* **2019**, 145, 488.
- [157] W. Liu, G. Liu, N. Shi, D. Liu, F. Wen, *ACS Appl. Nano Mater.* **2020**, 3, 12188.
- [158] T. Yan, Y. Wang, Y. Cao, H. Liu, Z. Jin, *Appl. Catal., A* **2022**, 630, 118457.
- [159] C. Cui, G. Zhang, Y. Yang, T. Wu, L. Wang, *J. Alloys Compd.* **2022**, 910, 164864.
- [160] W. Liu, P. Wang, J. Chen, X. Gao, H. Che, B. Liu, Y. Ao, *Adv. Funct. Mater.* **2022**, 32, 2205119.
- [161] W. Shi, W. Sun, Y. Liu, K. Zhang, H. Sun, X. Lin, Y. Hong, F. Guo, *J. Hazard. Mater.* **2022**, 436, 129141.
- [162] X. Li, P. Xu, M. Chen, G. Zeng, D. Wang, F. Chen, W. Tang, C. Chen, C. Zhang, X. Tan, *Chem. Eng. J.* **2019**, 366, 339.
- [163] Y. Shiraishi, S. Kanazawa, Y. Sugano, D. Tsukamoto, H. Sakamoto, S. Ichikawa, T. Hirai, *ACS Catal.* **2014**, 4, 774.

- [164] Y. Wu, J. Chen, H. Che, X. Gao, Y. Ao, P. Wang, *Appl. Catal., B* **2022**, 307, 121185.
- [165] Y. Yang, C. Zhang, D. Huang, G. Zeng, J. Huang, C. Lai, C. Zhou, W. Wang, H. Guo, W. Xue, R. Deng, M. Cheng, W. Xiong, *Appl. Catal., B* **2019**, 245, 87.
- [166] P. Ma, X. Zhang, C. Wang, Z. Wang, K. Wang, Y. Feng, J. Wang, Y. Zhai, J. Deng, L. Wang, K. Zheng, *Appl. Catal., B* **2022**, 300, 120736.
- [167] C. Tang, M. Cheng, C. Lai, L. Li, X. Yang, L. Du, G. Zhang, G. Wang, L. Yang, *Coord. Chem. Rev.* **2023**, 474, 214846.
- [168] G. Zhang, D. Huang, M. Cheng, L. Lei, S. Chen, R. Wang, W. Xue, Y. Liu, Y. Chen, Z. Li, *J. Mater. Chem. A* **2020**, 8, 17883.
- [169] T. Wu, X. Liu, Y. Liu, M. Cheng, Z. Liu, G. Zeng, B. Shao, Q. Liang, W. Zhang, Q. He, W. Zhang, *Coord. Chem. Rev.* **2020**, 403, 213097.
- [170] T. Inoue, A. Fujishima, S. Konishi, K. Honda, *Nature* **1979**, 277, 637.
- [171] J. Low, B. Cheng, J. Yu, M. Jaroniec, *Energy Storage Mater.* **2016**, 3, 24.
- [172] Q. Li, S. Wang, Z. Sun, Q. Tang, Y. Liu, L. Wang, H. Wang, Z. Wu, *Nano Res.* **2019**, 12, 2749.
- [173] N. Tian, Y. Zhang, X. Li, K. Xiao, X. Du, F. Dong, G. I. N. Waterhouse, T. Zhang, H. Huang, *Nano Energy* **2017**, 38, 72.
- [174] S. Cao, J. Low, J. Yu, M. Jaroniec, *Adv. Mater.* **2015**, 27, 2150.
- [175] M. Rakibuddin, H. Kim, *Beilstein J. Nanotechnol.* **2019**, 10, 448.
- [176] D. Huang, G. Zhang, J. Yi, M. Cheng, C. Lai, P. Xu, C. Zhang, Y. Liu, C. Zhou, W. Xue, R. Wang, Z. Li, S. Chen, *Chemosphere* **2021**, 263, 127672.
- [177] Y. Zhao, X. Liang, H. Shi, Y. Wang, Y. Ren, E. Liu, X. Zhang, J. Fan, X. Hu, *Chem. Eng. J.* **2018**, 353, 56.
- [178] W. Liu, Y. Li, F. Liu, W. Jiang, D. Zhang, J. Liang, *Water Res.* **2019**, 151, 8.
- [179] C. Zhao, Z. Liao, W. Liu, F. Liu, J. Ye, J. Liang, Y. Li, *J. Hazard. Mater.* **2020**, 381, 120957.
- [180] W. Fu, J. Yi, M. Cheng, Y. Liu, G. Zhang, L. Li, L. Du, B. Li, G. Wang, X. Yang, *J. Hazard. Mater.* **2022**, 424, 127419.
- [181] Q. Hao, Z. Mo, Z. Chen, X. She, Y. Xu, Y. Song, H. Ji, X. Wu, S. Yuan, H. Xu, H. Li, *Colloids Surf., A* **2018**, 541, 188.
- [182] Z. Zhu, X. Tang, W. Fan, Z. Liu, P. Huo, T. Wang, Y. Yan, C. Li, *J. Alloys Compd.* **2019**, 775, 248.
- [183] Z. Wang, E. Almatrafi, H. Wang, H. Qin, W. Wang, L. Du, S. Chen, G. Zeng, P. Xu, *Angew. Chem., Int. Ed.* **2022**, 61, e202202338.
- [184] H. Che, P. Wang, J. Chen, X. Gao, B. Liu, Y. Ao, *Appl. Catal., B* **2022**, 316, 121611.
- [185] M. Li, G. Wu, Z. Liu, X. Xi, Y. Xia, J. Ning, D. Yang, A. Dong, *J. Hazard. Mater.* **2020**, 397, 122766.
- [186] O. K. Dalrymple, E. Stefanakos, M. A. Trotz, D. Y. Goswami, *Appl. Catal., B* **2010**, 98, 27.
- [187] L. G. Corbellini, E. D. F. Costa, M. Cardoso, M. Nauta, *Microbiol Risk Anal.* **2017**, 6, 31.
- [188] Q. He, P. Xu, C. Zhang, G. Zeng, Z. Liu, D. Wang, W. Tang, H. Dong, X. Tan, A. Duan, *Crit. Rev. Biotechnol.* **2019**, 39, 746.
- [189] W. Wang, C. Zhou, Y. Yang, G. Zeng, C. Zhang, Y. Zhou, J. Yang, D. Huang, H. Wang, W. Xiong, X. Li, Y. Fu, Z. Wang, Q. He, M. Jia, H. Luo, *Chem. Eng. J.* **2021**, 404, 126540.
- [190] C. Tang, C. Liu, Y. Han, Q. Guo, W. Ouyang, H. Feng, M. Wang, F. Xu, *Adv. Energy Mater.* **2019**, 8, 1801534.
- [191] Y. Zou, X. Wang, A. Khan, P. Wang, Y. Liu, A. Alsaedi, T. Hayat, X. Wang, *Environ. Sci. Technol.* **2016**, 50, 7290.
- [192] M. A. Barakat, *Arabian J. Chem.* **2011**, 4, 361.
- [193] J. Li, W. Zhang, M. Ran, Y. Sun, H. Huang, F. Dong, *Appl. Catal., B* **2019**, 243, 313.
- [194] J. Liao, W. Cui, J. Li, J. Sheng, H. Wang, X. a. Dong, P. Chen, G. Jiang, Z. Wang, F. Dong, *Chem. Eng. J.* **2020**, 379, 122282.
- [195] X. Li, J. Xie, C. Jiang, J. Yu, P. Zhang, *Front. Environ. Sci. Eng.* **2018**, 12, 14.
- [196] Y. Long, L. Li, L. Zhou, S. Zhang, L. Wang, Z. Zheng, S. Wu, Y. Hei, F. Jiang, *Mater. Res. Bull.* **2020**, 126, 110787.
- [197] G. Palanisamy, N. H. Al-Shaalan, K. Bhuvaneswari, G. Bharathi, G. Bharath, T. Pazhanivel, E. V. Sathishkumar, M. K. Arumugam, S. K. K. Pasha, M. A. Habila, A. El-Marghany, *Environ. Res.* **2021**, 201, 111429.
- [198] T. Ni, H. Zhang, Z. Yang, L. Zhou, L. Pan, C. Li, Z. Yang, D. Liu, *J. Colloid Interface Sci.* **2022**, 625, 466.
- [199] Z. Xiong, Y. Jiang, Z. Wu, G. Yao, B. Lai, *Chem. Eng. J.* **2021**, 421, 127863.
- [200] X. Liu, D. Dai, Z. Cui, Q. Zhang, X. Gong, Z. Wang, Y. Liu, Z. Zheng, H. Cheng, Y. Dai, B. Huang, P. Wang, *ACS Catal.* **2022**, 12, 12386.
- [201] M. Zhang, Y. Yang, X. An, L. Hou, *Chem. Eng. J.* **2021**, 412, 128663.



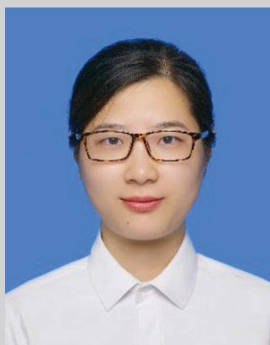
Yongxi Chen is studying for a master's degree in College of Environmental Science and Engineering, Hunan University, Changsha 410082, PR China. Her current research interest is mainly focused on the preparation of nanomaterials and their application in energy and environmental remediation.



Min Cheng received his Ph.D. degree under the supervision of Prof. Guangming Zeng from Hunan University, China, in 2018. He is currently an associate professor at the College of Environmental Science and Engineering, Hunan University. His current research interests focus on the development of MOF-based materials and porous materials for applications in catalysis and separation.



Cui Lai graduated from the College of Environmental Science and Engineering of Hunan University in 2013 and received her Ph.D. degree in Environmental Science. She joined Professor Guangming Zeng's group at Hunan University after completing her Ph.D. degree. Her main research interests are the development and environmental application of functional nanomaterial.



Zhen Wei is currently a research fellow in the College of Environmental Science and Engineering of Hunan University, where she received her Ph.D. in 2015. After graduation, Dr. Zhen Wei joined the Department of Chemistry in the University of Warwick as a Marie Skłodowska-Curie research fellow from 2016 to 2018. Her primary research interests focus on design of novel photocatalytic material-microbe hybrids for converting biorefinery wastes into fuels and value-added chemicals and for the degradation of organic pollutants in water.